# Studying orientational disorder with neutron total scattering

Guanqun Cai

*Submitted in partial fulfillment*
*of the requirements of the Degree of*
*Doctor of Philosophy*

October 2020

School of Physics and Astronomy
Queen Mary, University of London

Queen Mary
University of London

# Abstract

The orientations of chemical bonds and molecular groups are an important characteristic of the local structure of materials, and may determine the macroscopic performance of materials. Because orientational disorder happens over small length scales and fast time, it may not be accessible to many common characterisation techniques. The properties of neutron allow them to be an excellent tool for the study of orientational disorder in materials. In this thesis, I will demonstrate how orientational disorder can be studied using neutron total scattering and its Fourier transform, namely the pair distribution function. Combining neutron total scattering, the reverse Monte Carlo (RMC) and molecular dynamics (MD) simulations has shown how the phase transitions of KCN and $BaCO_3$ are associated with the orientational disorder of cyanides and carbonate molecular anions respectively, and has given quantitative information on the degree of disorder through analysis of the orientational distribution function. The study of $BaCO_3$ has been supported by molecular dynamics simulations, giving us a new picture of the phase transitions in both $BaCO_3$ and the related mineral calcite. The porous aromatic framework (PAF) has been studied by neutron total scattering and small angle scattering combined with molecular dynamics simulations. It has shown that the amorphous phase of PAF has the structure of a continuous random network similar to that of amorhous silica for example, but with orientational disorder of the biphenyl molecular groups about their long axes. Finally,the orientational disorder of ammonium and sulfate tetrahedra in $(NH_4)_2SO_4$ was studied by both neutron total scattering and RMC. It was found the orientational disorder plays an important role in the explanation of the giant entropy change during the ferroelectric phase transition.

# Acknowledgements

First, I would like to express my appreciation to the two people who took me to the real door of science, my supervisors Professor Martin Dove and Dr Anthony Phillips. It is very lucky for me to have Martin who can bomb me with endless, picky, devastating, desperate instruction messages on wechat until the last minutes of my thesis submission (even if it's over 22:00). I'm also very lucky to have Anthony who fled work to buy bread in working hours just in order to arrange more time including those after working hours to discuss Bee's book with me. They engraved me with lots of "golden codes" from never use multiple adjectives to never be vague when explaining things. Those golden codes will no doubt influence my future career and how I ~~teach~~ torture my future students if there is such an unfortunate guy on the earth.

I would like to offer my special thanks to Dr David Keen, Dr Helen Walker, Dr Alex Hannon, Dr Helen Playford, Dr Tom Headen, Dr Tristan Young, Dr Dean Keeble, Dr Ivan da Silva, Dr Issac Abrahams and Dr Franz Demmel for there help in my research. Meanwhile, I wish to thank everyone in the SPA QMUL especially those in CCMMP for their help.

I wish to acknowledge our research group members for their helpful discussions, including Dr Yuanpeng Zhang, Dr Ling Wang, Mr X – Dr Lei Wang (and his wife Ying Xiang), Dr Zhengqiang Yang, Dr Ovando Carter, Mark Wilkinson, Lei Tan, Zhongsheng Wei, Shurong Yuan, Bernet Meijer, Dr Richard Dixey, Dr Haolai Tian and Dr Lei Wang. I would like to acknowledge my friends including Dr Dabiao Liu, Dr Wenda Shi, Dr Yuan Li, Dr Manting Qiu, Dr Jingliang Miao, Dr Fei Xie, Dr Zhichao Weng, Dr Xueyan Hou, Ying Liu, Chen Lyu, Junning Li, Fei Peng, Yizheng Zhou, Changhong Wang, Bingqing Guo and Xindi Zhang for their company.

I would like to express my sincere thanks to China Scholarship Council and

Queen Mary University of London for their financial support.

Special thanks to Dr Jiaxun Liu for her technical support and free lessons on RMC and relevant analysis, plus the encouragement and enlightment she brought.

Finally, I am grateful to my parents (Jing Chen and Yongxin Cai), grandparents and other family members. Without their care and education, I would not have any chance to pursue a PhD. Particularly, I'm grateful to my grandfather Jingchen Cai who is now in Heaven. He set an example by himself to teach me to be a upright person.

# Contents

# List of Tables

# Chapter 1

# Introduction

## 1.1 Introduction of oreintational disorder: through a case study of water

Nature creates materials with order and disorder at different scales. Depending on the length scale, it can be divided into the short range order, medium range order and long range order for atomic structures. The short range order refers to the order within a unit cell, e.g. less than 5 Å. The medium range order refers to the order involving a few neighbouring unit cells, e.g. 5 Å to 15 Å and the long range order refers to the periodic order e.g. larger than 15 Å. A set of well defined atoms with short range order may orient in different directions and result in a medium or long range disorder. This phenomenon can be summarized as the orientational disorder.

Taking one of the most substantial and important materials, water, as an example, the water molecule is a simple combination of one oxygen atom and two hydrogen atoms. In a water molecule, the H–O bond length is 0.957 Å and the H–O–H angle is 104.52° [1]. This H–O–H angle results in the absence of a centre of symmetry and a permanent dipole moment. These simple water molecules

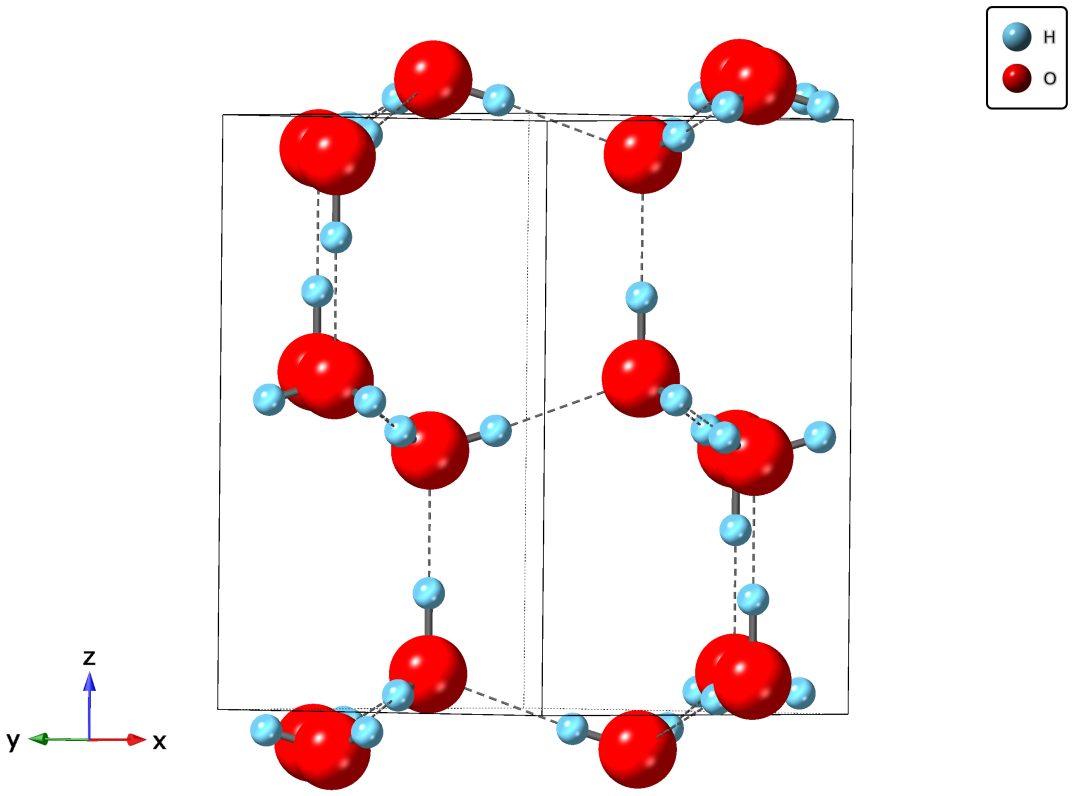


Figure 1.1: The crystal structure of Ice Ih. Ice Ih has a Wurtizite structure. Its space group is $P6_3/mmc$. The red spheres represent the oxygen atoms and the cyan spheres represent the hydrogen atoms. In this structure, the oxygen atoms sit on a hexagonal lattice. Each oxygen atom must accept two hydrogen atoms from the neighbouring oxygen atoms in the meantime offer two hydrogen atoms to the neighbouring oxygen atoms in order to form a tetrahedral hydrogen bonding network. Thus, the orientation of the $H_2O$ molecule is constrained by the neighbouring $H_2O$ molecules within the lattice. The crystal structure is drawn based on the refined model from reference [3].

are rigid. No matter in the liquid water or in different phases of ice, the basic geometry and properties of water molecules remain intact [2]. In other words, the arrangement of oxygen and hydrogen atoms within the water molecule is well defined.

In the solid form of water, ice, the water molecules are arranged according to periodic lattice. Fig. 1.1 shows the crystal structure of the most common ice phase Ice Ih. In this crystalline phase, the oxygen atoms sit on a well defined hexagonal

lattice, showing a long range periodic order. Unlike the oxygen atoms which strictly following the crystallography rules, the arrangement of hydrogen atoms for every water molecule in every unit cell is different. A more concise description is the orientation of O-H bonds or the orientation of the permanent dipole of water molecule is disordered. However, there is a constraint from neighbouring atoms to distinguish the orientational disorder of O-H bonds from complete randomness. Each oxygen has to accept two hydrogen atoms from the neighbouring oxygen atoms and offering two hydrogen atoms to the neighbouring oxygen atoms [4]. Otherwise, the crystal lattice will not be stable. The orientation of water molecules is actually correlated with the neighbouring water molecules. Considering the intrinsic dipole moment of water molecules, this orientational disorder has an important effect on the unusual dielectric and electric conductive behaviours of water and ice [2].

The ice example illustrates, between the well-defined rigid unit, e.g. rigid molecules or bonds, and the well-studied crystallographic long range order, there is orientational disorder of the rigid units, often correlated with neighbouring unit. Orientational disorder is actually not uncommon in nature. Examples range from molecular crystals [5] such as fullerenes [6] to polyatomic ions in metal-organic frameworks [7] and even hemes in proteins [8].

Moreover, it is this orientational disorder that leads to many interesting properties of materials. For instance, molecular ions such as methylammonium or formamidinium have permanent dipole moments just like water molecules. The orientational disorder of methylammonium ions in the hybrid perovskite methylammonium lead iodide ($MAPbI_3$) has been studied extensively to investigate its relationship with the optoelectronic properties of $MAPbI_3$, the solar cell material with great expectations [9–11]. Understanding the orientational disorder in materials plays an important role in understanding and tuning [12] many interesting properties of materials.

## 1.2 Method to study orientational disorder

### 1.2.1 Bragg diffraction

Bragg diffraction is perhaps the indispensable standard routine to study the material structures. One method often adopted by crystallographers to characterize the orientational disorder of rigid units is to use equivalent sites for certain atoms in a unit cell model to refine the Bragg diffraction data [13].

Sometimes, it is not enough to describe the orientational disorder with this simple discreet model. Instead, the atomic structure must be described in terms of a continuous distribution of rigid units orientations. A common approach is to expand these distribution functions in terms of an appropriate basis of "rotator functions" such as symmetry-adapted spherical harmonics[14]. This process reduces the problem of describing the structure to that of determining the appropriate coefficients for the basis functions, which can be done in analysis of Bragg diffraction data using a standard least-squares refinement of the Bragg diffraction data.

However, this method has two related problems[15, 16]. First is that it is only practical to relatively low order, and second, as a consequence the resulting distribution function is not necessarily positive for all possible orientations [17–19].

### 1.2.2 Local structure probes

Nuclear magnetic resonance spectroscopy (NMR) is a powerful tool to probe the local structure of materials. In a single crystal sample, the orientation of certain bonds associated with the designated nuclei species (usually light elements) can be deduced from the line shape of the measured spectra[20, 21]. Nowadays, with the aid of DFT calculations, NMR is becoming more powerful in determining the local structure geometry of materials [22]. However, it is mainly sensitive

to the very local coordination environment of a designated kind of nuclei, and much less sensitive to the structure at larger distances. The orientation disorder of a rigid unit may correlate with the structure on a larger scale than the very local coordination environment that NMR is mostly sensitive to [23]. Lots of past research experience show a model that fits the local structure well is not necessarily consistent with experimental data showing larger range order[24]. Besides, for some complex molecular ions, NMR is not capable of deducing the whole molecular orientation. These characteristics make NMR less powerful in orientational studies.

Extended X-Ray Absorption Fine Structure (EXAFS) is another commonly used technique to probe the local structure of materials [24]. The Fourier transform of the measured spectra gives the coordination atom distribution around a specific element [25]. Like NMR, EXAFS is very powerful to probe the very local structure but less powerful to probe structures larger than a few angstroms. The limited length scale and the fact that it only contains local structure information for a single element (usually heavy elements with plenty of electrons) restrain EXAFS alone to be sufficient for orientational disorder study[26].

## 1.3 Total scattering + big box simulation

Total scattering, in a nutshell, is all the scattering of a beam of radiation from a material, measured without discrimination of energy and hence effectively integrating over all values of energy transfer [24, 27, 28]. In particular, it includes both Bragg scattering (elastic scattering, with no change in radiation energy, from long-range order) and diffuse scattering (from local disorder, containing dynamic process information). Taking the space Fourier transform of the total scattering function yields the material's pair distribution function (PDF): a weighted sum of the histograms of instantaneous interatomic distances between each pair of atom-types. Of particular note in this context, the pair distribution function is

directly sensitive to the distribution of rigid unit orientations in a complementary way to the Bragg peak intensities and covers both local and long range structures for all atom species. Thus, there comes a promise of understanding the whole picture of orientational disorder by fully exploiting the total scattering data.

Although in physics, we prefer simple, easy models to describe the complexity of disorder more or less in a beautiful and concise way, real life applications demand us to put forward physical models more complicated and accurate than simple models such as the Ising model [4]. The construction of a reasonable model for orientational disorder must be based on the accurate characterization of a large numbers of rigid units' orientations.

Fortunately, modern computational power allows us to construct a big simulation box (usually contains more than hundreds of unit cells for crystalline materials or more than 50 Å per dimension for amorphous materials) to simulate the behaviours of tens of thousands of rigid units. The big box simulation methods in this context refer to the molecular dynamics (MD) and the reverse Monte Carlo method (RMC), the details of which will be discussed in Chapter 2.

With the aid of big box simulation, the structure information contained in the experimental total scattering data can be fully exploit to characterize the orientational behaviours of rigid units. On this basis, the orientational disorder of certain rigid units, its correlation with neighbouring units, the synergetic effect from the short, medium and long range order and the relationship between orientational disorder and specific properties of materials, can be studied with the theoretical tools of statistical mechanics and lattice dynamics [29, 30].

## 1.4 Outline of the thesis

This thesis aims at studying orientational disorder in a series of materials by the combination of neutron total scattering and big box simulation.

Chapter 2 gives a detailed introduction about the methods used in these orientational disorder studies, including the experimental aspects of neutron scattering, pair distribution function formalism, the Rietveld refinement, the molecular dynamics method, the reverse Monte Carlo method and symmetry adapted functions to quantitatively describe the orientation of rigid units.

Chapter 3 tells the story of phase transitions of a orientationally-disordered crystal potassium cyanide (KCN). The orientational behaviour of the cyanide ions during the phase transitions is quantified by the combination of total scattering and RMC.

Chapter 4 explores the role of orientational disorder in the phase transition of calcium carbonate ($CaCO_3$) and barium carbonate ($BaCO_3$).

Chapter 5 introduces the study of a porous aromatic framework material (PAF-1). This study tries to uncover the structure mystery of this open porous amorphous tetrahedral network.

Chapter 6 explores the relationship of orientational disorder and the caloric effect of ammonium sulfate ($(NH_4)_2SO_4$). Understanding the mechanism of the colossal entropy change during the phase transition of this compositionally simple material can instruct further development of new materials for cooling applications.

Chapter 7 provides a conclusion for the work presented in this thesis.

# Chapter 2

# Methods

## 2.1 Introduction to neutron scattering

### 2.1.1 Basics of neutron scattering

The atomic structures of materials (e.g. the unit cell structure of crystals) is at the length scale of a few to tens of angstroms. Therefore, they are usually studied by the scattering of particles or photons with comparable wavelength. The wavelength requirement and accessibility often limits the candidates to three kinds of particles: electrons, X-rays and neutrons. Fig. 2.1 shows their scattering process with the atoms. Electrons are charged particles. Their interactions with the atoms are actually electrostatic interactions with orbital electrons. Electron scattering is often limited to surface studies because the strong electrostatic force prevents electrons from penetrating deeply into the materials. The electromagnetic waves X-rays interact with the orbital electrons of atoms and they are able to penetrate further than the electrons (e.g. a few millimetres of aluminium) [31].

A neutron has no charge. However, it has a magnetic spin. Thus, neutrons are not only able to interact directly with the nuclei of the atoms via the strong nuclear force but also able to interact through dipole - dipole magnetic interaction

if there are unpaired electrons in some of the atoms of the material. Neutrons are able to penetrate deeply into materials (e.g. a few centimetres of aluminium) and hence suitable to study the bulk structure of the materials [27].

However, low flux of the incident neutron beam and low scattering power requires the sample for a neutron scattering experiment has to be much larger (around 2 $cm^{-3}$ cubic centimeters in volume) than those required for electrons and X-rays scattering (0.0001 $mm^{-3}$ in volume is enough). Besides, because in most cases the neutrons interact with the atomic nuclei rather than electrons (except magnetic interaction), the contribution of different elements to the overall scattering is independent of the number of electrons in atom, whereas the scattering of electrons and X-rays are dominated by heavy elements with larger number of electrons if both heavy and light elements are present in the material.

Neutrons as the experimental probe can be divided into hot, thermal and cold neutrons depending on their wavelength. The wavelength of hot neutrons are 0.4 Å–1 Å. The wavelength of thermal neutrons are 1 Å–3 Å. And the wavelength of cold neutrons are 3 Å–30 Å [32].

Neutrons are a good probe choice under the following circumstances:

- The wavelength of neutrons (0.4 Å – 30 Å) is comparable to the atomic distances and lattice spacings in materials
- The experiment aims at studying the bulk structure of the material
- The experiment is focused on the study of the magnetic behaviours of materials.
- The energy of thermal neutrons is the same order of most excitations e.g. the phonon excitations.
- Neutrons are usually non-destructive to samples.

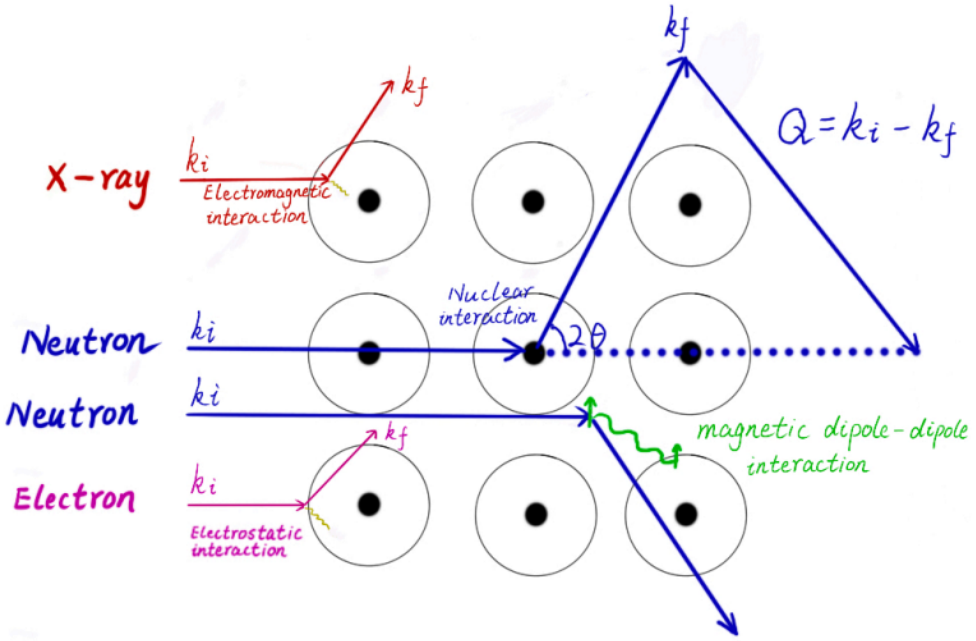


Figure 2.1: Illustration of scattering process for neutrons (blue beam), X-rays (red beam) and electrons (pink beam)

- There are both light and heavy elements in the material especially when the behaviour of the light element is important in the study.

A scattering experiment aims at measuring the change of the momentum and energy of a scattered particle. The incident particle has a wave vector of $\mathbf{k}_i$ characterizing the momentum of the particle and a angular frequency $\omega_i$ characterizing the energy of the particle. After interacting with an atom, the wave vector of the scattered particle becomes $\mathbf{k}_f$ and the angular frequency of the scattered particles becomes $\omega_f$. The momentum transfer in neutron scattering is defined as the wave vector change $\mathbf{Q}$ between the incident particle and the scattered particle.

$$\mathbf{Q} = \mathbf{k}_i - \mathbf{k}_f \tag{2.1}$$

As shown in Fig. 2.1, the angle between $\mathbf{k}_i$ and $\mathbf{k}_f$ is called scattering angle $2\theta$. The energy transfer is characterized by the frequency change $\omega$ between the incident

particle and the scattered particle through $E = \hbar\omega$.

$$\omega = \omega_i - \omega_f \tag{2.2}$$

The final result from a neutron scattering experiment is a scattering function $S(\mathbf{Q}, \omega)$ as a function of $\mathbf{Q}$ and $\omega$. The analysis of neutron scattering experiments is based on this function [32].

### 2.1.2 Introduction to neutron scattering length

The interaction strength of a particle and an atom, i.e. the form factor, is usually a function of incident wavelength and scattering angle $f(\lambda, \theta)$. Because the interaction of a neutron and an atom is like an isotropic point to point interaction at a very short distance ($10^{-4}$ Å) compared with the wavelength of neutron, it's often a good approximation that the interaction strength is independent of the interaction direction and the wavelength of the neutron. Therefore, the interaction strength of a neutron and a type of atom is a constant, called the scattering length $b$. [1]

Being a constant does not make the neutron scattering length simple. The scattering length can be positive or negative depending on whether the incident neutron is subjected to a repulsive potential (positive scattering length) or attractive potential (negative scattering length) of the nucleus. It can also be a complex number, the imaginary part of which represents the absorption of neutrons. For an atom with a non-zero spin, different spin orientations give different scattering length. This indicates different isotopes of an element have different scattering length values and even an isotope at different spin states have different scattering length values. Therefore, the scattering length for a type of nuclei is composed of an average value $\bar{b}$ (coherent scattering length) and a standard deviation $\Delta b$ (incoherent scattering length). They result in the coherent neutron scattering and

[1] For dipole – dipole magnetic interaction i.e. the magnetic form factor is a function of the scattering angle or $\mathbf{Q}$, but the discussion of magnetic scattering is out of the scope of this thesis.

the incoherent scattering respectively [31].

$$b = \bar{b} \pm \Delta b \tag{2.3}$$

### 2.1.3 Coherent and incoherent neutron scattering

Because the coherent scattering length characterizes the average behaviour for each type of atoms, coherent scattering is a result of overall interference between the neutron waves and the scatterer centres. Hence, it contains the structural information of relative positions of different atoms (elastic scattering) or collective dynamics (inelastic scattering). Incoherent scattering, on the other hand, comes from the scattering of different states for a single atom. Instead of structural information, it reflects the movement of a single atom or single atom dynamics. Because structural information comes from the coherent scattering, incoherent scattering is regarded as nuisance to minimize in most neutron experiments except in quasi-elastic neutron scattering (QENS), where incoherent scattering is particularly desired to study the single atom or single ion dynamics [33].

Fortunately, the incoherent scattering for most atom types are quite small except one common atom type $^1$H. $^1$H is famous for having the largest incoherent scattering length in the neutron world. Its incoherent scattering often becomes dominant in the overall scattering and dominate the real desired signals for scientists. Therefore, for structure and collective dynamics studies, deuterated samples are often used for materials containing hydrogen.

### 2.1.4 Elastic and inelastic neutron scattering

In terms of whether there is energy transfer, neutron scattering can be divided into elastic and inelastic scattering. If there is no energy transfer, the neutron scattering is elastic. The $S(\mathbf{Q}, \omega)$ becomes only a function of $\mathbf{Q}$. The magnitude

remain unchanged for $\mathbf{k}_i$ and $\mathbf{k}_f$, and the wave vector $\mathbf{Q}$ can be calculated as

$$\mathbf{Q} = \frac{4\pi \sin\theta}{\lambda} \tag{2.4}$$

where $\lambda$ is the wave length of the neutron [30].

If there is energy transfer, the neutron scattering is inelastic. Inelastic neutron scattering is often used to study the dynamics of materials. For an inelastic neutron scattering experiment, either the incident neutrons or the scattered neutrons have to be selected in order to measure the energy transfer. In a neutron diffraction experiment, there is no neutron selection before or after the experiments. It is often assumed that all the scattering is elastic. The wave vectors are calculated according to Eq. (2.4). However, this assumption is not exactly true. For diffraction studies, the inelastic scattering is treated as background. Total scattering is almost the same as diffraction in terms of the basic measurement idea. However, the scattering from the inelastic part becomes valuable information in total scattering studies.

### 2.1.5 Neutron sources

Currently there are two kinds of neutron sources in the world. One is called the reactor source, in which the neutrons are produced through nulear fission. The other one is the spallation source. In a spallation source, protons are accelerated in either linear or synchrotron accelerators and then hit to a heavy metal target. As shown in Fig. 2.2, the incident protons will react with the neutrons and protons within the nuclei and produce high energy protons, neutrons and muons while leaving the nuclei excited. This process is called the intranuclear cascade. Some of the high energy particles will escape the nuclei and collide with other nuclei in the target causing secondary spallation reactions. In the meantime, the excited nuclei will emit relatively low energy neutrons, protons and alpha particles etc. The produced low energy neutrons are first slowed down by moderators to the

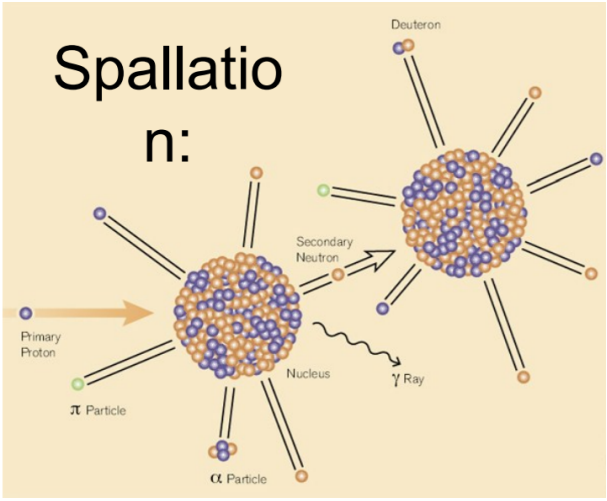


Figure 2.2: Illustration of the spallation reaction process [35].

usable energy scale and then to different instrument[34]. All the experimental data involved in this thesis is measured at the UK pulsed spallation neutron source ISIS.

### 2.1.6 Neutron scattering instruments

The neutron scattering experiments in this thesis are carried out on three instruments, the General Materials Diffractometer (GEM), the Near and Intermediate Range Order Diffractometer (NIMROD) and Polaris.

GEM is a diffractometer with high intensity and good resolution. It is able to measure not only the diffraction patterns to study the atomic and magnetic structures of crystalline materials but also pair distribution functions to study the disorder in crystalline and amorphous materials [36].

NIMROD is a special instrument aiming at bridging the gap between the wide angle scattering (high Q, short range structure) and the small angle scattering (low Q, large scale structure). This instrument has 25 detector banks covering a Q range of $0.02\,\text{Å}^{-1}$ to $50\,\text{Å}^{-1}$. This corresponds to the structure scale about 1 Å to 300 Å [37].

Polaris is also a diffractometer suitable for measuring both the Bragg patterns

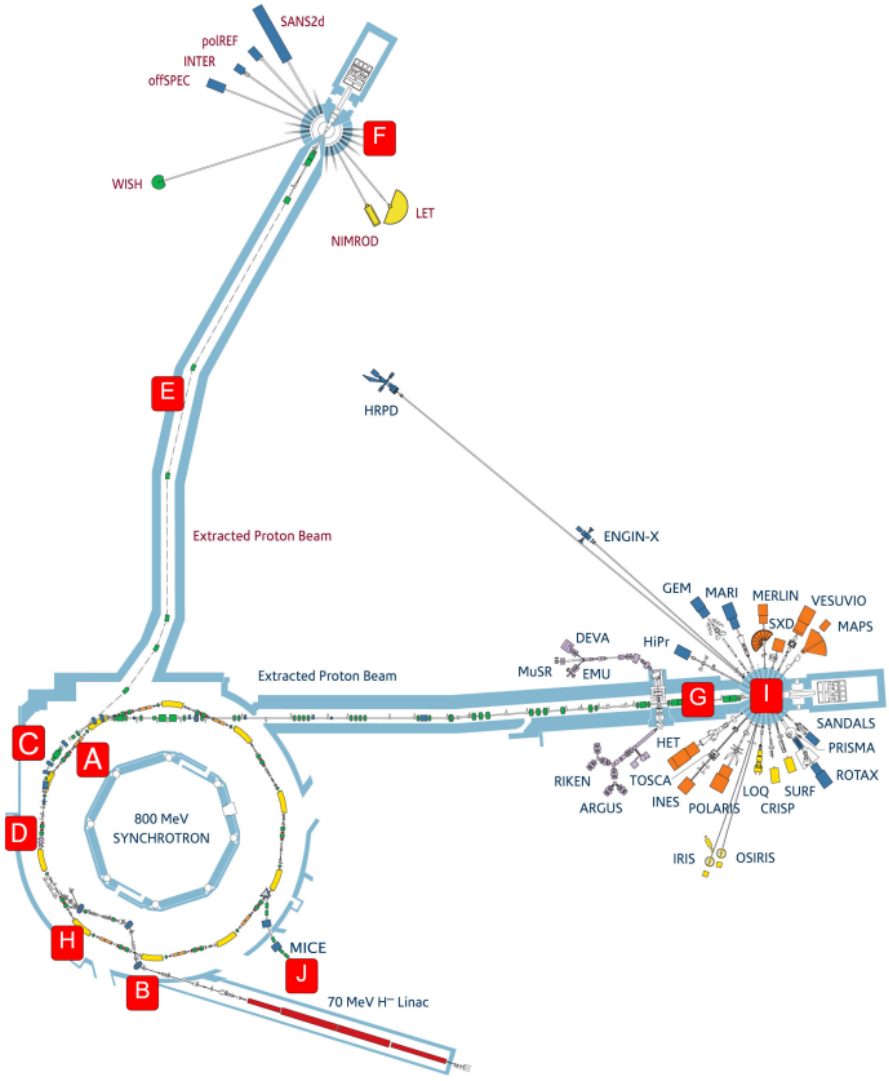


Figure 2.3: Layout of the ISIS neutron source. GEM and Polaris are in Target station 1i.e. Zone I, and NIMROD is in target station 2 i.e. Zone F. The graph is taken from the STFC ISIS website.

and the pair distribution functions. Particularly, the design of the instrument allows for small samples ( 1mm$^3$ in volume), short runs and various in-situ experimental environments [38].

## 2.2 Bragg scattering and Rietveld refinement

### 2.2.1 Bragg scattering and the Bragg's law

Studying the structure of materials with scattering experiments stems from the discovery of the first crystal diffraction by von Laue. After that, the Braggs solved the crystal structure of sodium chloride (NaCl) with X-ray diffraction and opened the door for modern crystallography. A crystal diffraction pattern is mainly coherent elastic scattering. The coherent elastic scattering contains information of the relative position of atoms i.e. the static structure of materials. The golden rule to decipher the underlying symmetry of crystals is the Braggs' law:

$$\lambda = 2d_{hkl} \sin \theta_{hkl} \tag{2.5}$$

where $\lambda$ is the wavelength of the radiation, $\theta$ is the scattering angle, $h$,$k$,$l$ are the Miller indices[2] and $d$ is the interplanar spacing. The interplanar spacing is defined as the distance between different planes of atoms in a periodic structure. Therefore, the coherent elastic scattering is also called the Bragg scattering.

### 2.2.2 powder diffraction and Rietveld refinement

Ideally, the structure for a crystalline material is best solved by the single crystal diffraction. While large, high quality single crystals are often hard to grow. Poly-crystalline powder samples are easy to obtain but composed of crystallites with random orientations. The reflection peaks that are not related may have similar

[2]Miller indices h, k, l are defined as the reciprocals of the intercepts of planes at lattice vectors a, b and c respectively.

d-spacings and create overlapping peaks, which make it hard to index every peak and solve the crytal structure.

Often the structure underlying the diffraction patterns is resemble to some known unit cell structure. The key idea of the Rietveld refinement is to refine a pre-defined unit cell model until the difference of the Bragg patterns calculated from the model and the experimental Bragg patterns reaches minimum [39]. In this way, the Rietveld refinement is able to overcome the problem of complex Bragg patterns with overlapping peaks.

Actually, the Rietveld refinement not only refines the parameters about the unit cell model (e.g. lattice parameters, atomic positions, atomic displacement parameters (ADPs)[3] etc.), it also involves parameters from the instrument (e.g. parameters to determine the peak shape etc. ) and the macroscopic properties of the samples (crystallite size, texture orientation, neutron absorption etc.) In this way it considers every aspect that may influence the peak intensity and position in the Bragg patterns. However, careful must be taken to avoid unreasonably strong correlations between two parameters (such as the neutron absorption coefficient correlates with one ADP) and produce false minimum [40].

The goodness of the fit can be measured by the weighted profile R-factor $R_{\mathrm{wp}}$:

$$R_{\mathrm{wp}} = \sqrt{\sum_i \omega_i \left(y_{io} - y_{ic}\right)^2 / \sum_i \omega_i y_{io}^2} \tag{2.6}$$

where $i$ represents the $i$th data point, $y_{io}$ is the experimentally observed intensity, $y_{ic}$ is the calculated intensity from the refined model and $\omega_i$ is the weight factor weighted by $1/y_i$. The $R_{\mathrm{wp}}$ is not an absolute standard of the goodness of the fit. It is always suggested to judge how good the refinement is from direct observation of the fit and from whether the refined model is physically plausible.

For diffraction data measured with time-of-flight (TOF) instruments, such as instruments at ISIS, the $d$-spacing is determined by the flight time of neutrons

[3]The atomic displacement parameter ADP is the mean-squared displacement of the atom from its equilibrium position. It has a effect to diminish the diffraction intensity.

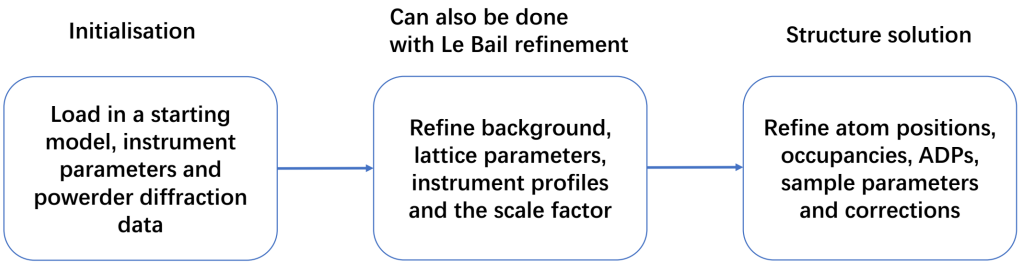


Figure 2.4: The work flow for the Rietveld refinement.

according to Eq. (2.7):

$$t = \mathrm{DIFC}d + \mathrm{DIFA}d^2 + \mathrm{ZERO} \tag{2.7}$$

where DIFC, DIFA and ZERO are instrument constants [41].

A typical procedure for Rietveld refinement is shown in Fig. 2.4. After choosing a starting unit cell model and loading in the instrument parameters and diffraction data, the background, lattice parameters, instrument profiles and the scale factor to set up a good foundation for further structure refinement. This step can also be done with the Le Bail refinement, which only refines the reflection intensity without any model bias [42]. Then the atom positions, occupancies, ADPs, crystallite orientations and neutron absorption corrections can be refined [43].

The final result of the Rietveld refinement is a unit cell model characterizing the time and space averaged behaviour of the material at the atomic scale. It is able to provide insights ranging from the basic structure and composition determination to material processing (e.g. texture analysis).

## 2.3 Total scattering

Total scattering automatically integrates over all orientations, time and energies [27]. It is composed of the Bragg scattering, which reflects the time- and space-averaged structure, and the diffuse scattering containing information about the

local structure disorder[24]. The measuring process of total scattering is almost the same as traditional neutron diffraction, but there are four extra requirements[28]:

- larger $Q_{\max}$[4] for higher Fourier transform resolution
- broader incident neutron energy spectrum to cover the energy scales of phonons
- a more accurately measured background
- longer measuring time to ensure good statistical accuracy

Performing total scattering with modern spallation neutron sources allows for good resolution in $Q$-space and for a high value of $Q_{\max}$, as well as having sufficient energy to cover the energy scales of phonons. In practical measurements, total scattering experiments are performed on polycrystalline materials, giving an average over all orientations of the crystal with respect to the instrument (incoming beam direction and position of the detector) and hence over all orientations of the scattering vector $\mathbf{Q}$. Thus practical total scattering measurements are performed as a function of $Q = |\mathbf{Q}|$.

### 2.3.1 Total scattering formalism

In neutron scattering, the density of the scattering atoms can be expressed as a sum of Dirac delta functions:

$$\rho(\mathbf{r}) = \sum_j b_j \delta(\mathbf{r}_j - \mathbf{r}) \tag{2.8}$$

where $\mathbf{r}_j$ is the position of atom j and $b_j$ is the scattering length of atom j; Its Fourier transform gives $F(\mathbf{Q})$

$$F(\mathbf{Q}) = \int \rho(\mathbf{r}) \exp(i\mathbf{Q} \cdot \mathbf{r}) \mathrm{d}\mathbf{r} = \sum_j b_j \exp(i\mathbf{Q} \cdot \mathbf{r}_j) \tag{2.9}$$

[4] $Q_{\max}$ is the maximum value of Q a scattering experiment is able to measure. It also determines the minimum d-spacing measurable in a scattering experiment through $d_{\min} = 2\pi/Q_{\max}$.

However, in total scattering, it is not $F(\mathbf{Q})$ that we measure, but a time and orientation averaged $S(\mathbf{Q})$ integrated over all energies.

$$
\begin{aligned}
S(\mathbf{Q}) &= \frac{1}{N}\left|F(\mathbf{Q})\right|^2 && (2.10)\\
&= \int S(\mathbf{Q},\omega)\mathrm{d}\omega && (2.11)\\
&= \frac{1}{N}\sum_{j,k} b_j b_k \int\int \exp(i\mathbf{Q}\cdot\mathbf{r}_{jk}(t))\exp(-i\omega t)\mathrm{d}t\mathrm{d}\omega && (2.12)\\
&= \frac{1}{N}\sum_{j,k} b_j b_k \left\langle \exp(i\mathbf{Q}\cdot\mathbf{r}_{jk})\right\rangle && (2.13)\\
&= \frac{1}{N}\sum_{j,k} b_j b_k \frac{\sin(Qr_{jk})}{Qr_{jk}} && (2.14)
\end{aligned}
$$

Subtracting the self scattering part i.e. when $i = j$, from $S(Q)$ gives the total scattering $i(Q)$:

$$
\begin{aligned}
i(Q) &= S(Q) - \sum_m c_m b_m^2 - S_0 && (2.15)\\
&= 4\pi\rho \int \sum_{m,n} c_m c_n b_m b_n r^2 \left(g_{mn}(r) - 1\right)\frac{\sin(Qr)}{Qr}\,\mathrm{d}r && (2.16)
\end{aligned}
$$

where $c_m$, $c_n$ are the fraction of all atoms for type $m$ and type $n$ respectively, $\rho$ is the density of atoms, $g_{mn}(r)$ is the partial atomic pair distribution functions and $S_0$ is the delta function at $Q = 0$:

$$
S_0 = 4\pi\rho \int \sum_{m,n} c_m c_n b_m b_n r^2 \frac{\sin(Qr)}{Qr}\,\mathrm{d}r \qquad (2.17)
$$

It represents the neutron transmission. A set of partial atomic pair distribution functions $g_{mn}(r)$ are defined as the number of atoms of type $m$ contained within a thin spherical shell of radius $r$ and thickness $\mathrm{d}r$. In the limit as $r \to \infty$, $g_{mn}(r) \to 1$, representing the uniformly distributed disorder. Moreover, because atoms cannot be closer than some minimum distance, we have $g_{mn}(r) = 0$ for small values of $r$.

In practice $i(Q)$ is extracted from the measurements by removing scattering from the sample container, the sample environment, and background scattering from within the instrument and beam attenuation by the sample container and

sample environment. These corrections are obtained by a serious of background measurements (empty instrument, empty sample environment, and sample environment with empty sample container), together with a standard sample measurement for normalization, usually a measurement from a vanadium rod [44].

### 2.3.2 Pair distribution function

The measured reciprocal space total scattering data is often Fourier transformed to and analysed as real space pair distribution function [28]. Mathematically, it's defined as [45] :

$$D(r) = 4\pi\rho r \sum_{m,n} c_m c_n b_m b_n \left(g_{mn}(r) - 1\right) \tag{2.18}$$

The functions $i(Q)$ and $D(r)$ are linked through Fourier sine transforms,

$$D(r) = \frac{2}{\pi} \int_0^\infty Q i(Q) \sin(Qr)\, \mathrm{d}r \tag{2.19}$$

There are other definition of PDF in the literature, including $G(r)$ and $T(r)$:

$$G(r) = \frac{D(r)}{4\pi\rho r} \tag{2.20}$$

$$T(r) = 4\pi r\rho \left[ G(r) + \left( \sum_{i=1}^{n} c_i \bar{b}_i \right)^2 \right] \tag{2.21}$$

A direct analysis of the PDF without any atomic model refinement provides 3 pieces of information[23]:

- The positions of the peaks tell the average interatomic distances.
- The area under each peak gives information about the corresponding coordination number.
- The width of the peak reflects the extent of bonds variation, thus indirectly reflects how disorder the bonds are.

Further information can be extracted from the PDF by refining a known structure against the PDF data. The "real-space Rietveld" method [46] in which the structural parameters of one or a few unit cells are refined by fitting to the PDF data is one of the most popular method, albeit not taking explicit account of Bragg scattering data. Because of the restricted number of the refined unit cells, multiple structure models are sometimes needed for different length scales in order to fully characterize the structure evolution over the whole PDF length scale (usually over $10\,\text{Å}^{-1}$ for amorphous materials and over $30\,\text{Å}^{-1}$ for crystalline materials)[47].

## 2.4 The Reverse Monte Carlo method

The Reverse Monte Carlo simulation (RMC) is the only method in common use that gives configurations of large numbers of atoms consistent with experimental data, most importantly both the Bragg scattering and pair distribution functions are included. [48] The primary goal of RMC is to obtain a sufficiently large structure model to consistently reflect the structure characteristics across the local short range to the periodic long range. [49]

Unlike the traditional Monte Carlo method, which refines a structure model purely relying on the minimization of a theoretical energy without any consideration of experimental data, RMC successively modifies an atomic configuration until the modified configuration gives a set of calculated patterns in best agreement with the experimental data. [50]

In the RMC method, an initial atomic configuration, a box of atoms with 50 Åper side, is generated from any source, including, for example, the results of a Rietveld refinement of the crystal structure from the corresponding Bragg scattering data, or the results of a molecular dynamics simulation. The RMC process proceeds by selecting an atom at random and moving it a random distance

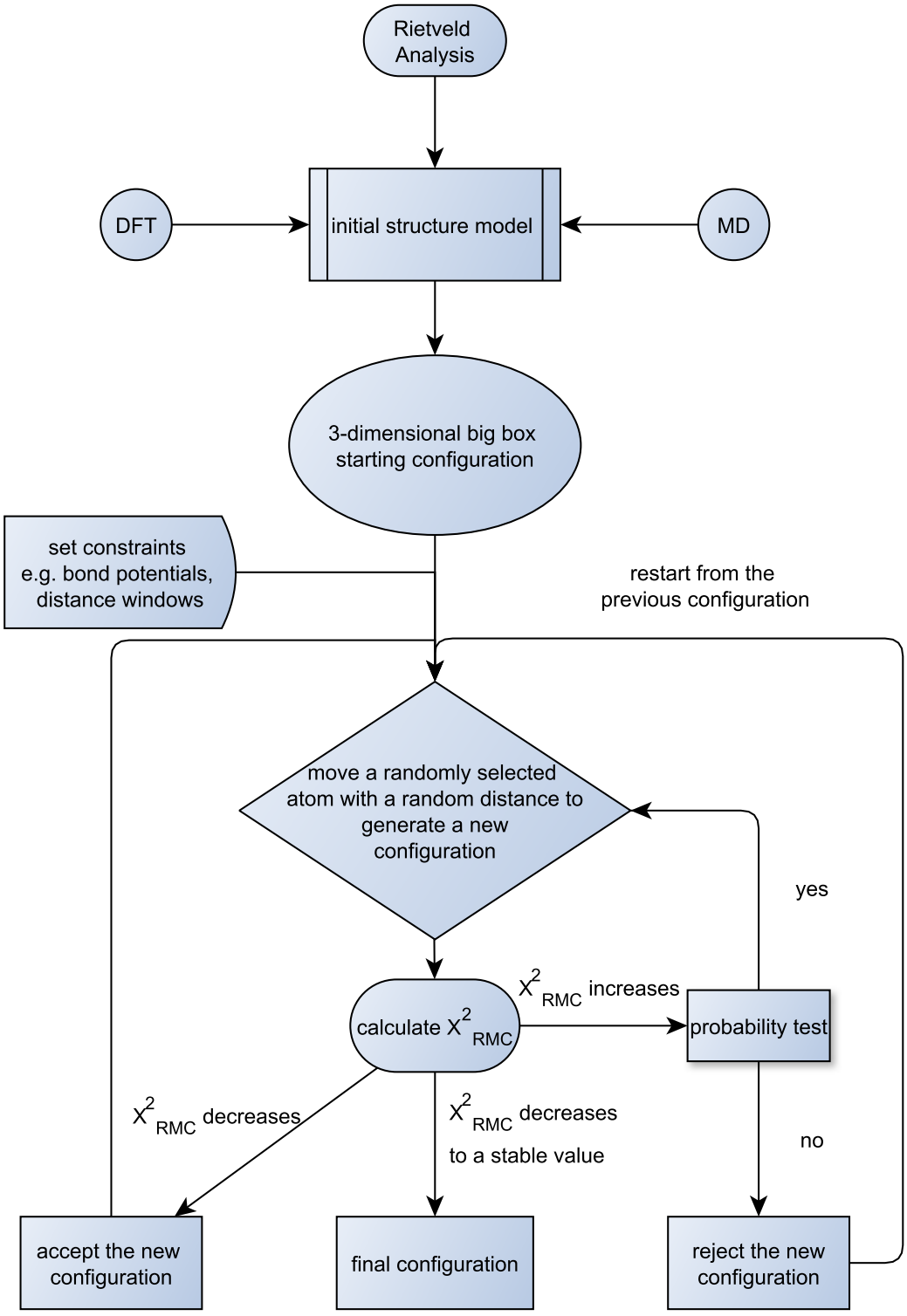


Figure 2.5: RMCProfile work flow

(up to some pre-defined maximum value). Every step change of the configuration will cause a change in $\chi^2_{\mathrm{RMC}}$, the energy function representing the difference of calculated data patterns and the experiment data patterns. The energy function $\chi^2_{\mathrm{RMC}}$ contains four parts, corresponding to the difference between calculated and experimental PDF, scattering data, Bragg (if the samples are crystals) and the potential energy term (if the potential constraints are set) respectively:

$$\chi^2_{\mathrm{RMC}} = \chi^2_{D(r)} + \chi^2_{i(Q)} + \chi^2_{\mathrm{Bragg}} + \chi^2_{\mathrm{energy}} \tag{2.22}$$

where the three data functions are defined as

$$\chi^2_{D(r)} = \sum_j \left[D_{\mathrm{calc}}\left(r_j\right) - D_{\mathrm{exp}}\left(r_j\right)\right]^2 / \sigma^2_{D(r)} \tag{2.23}$$

$$\chi^2_{i(Q)} = \sum_j \left[i_{\mathrm{calc}}\left(Q_j\right) - i_{\mathrm{exp}}\left(Q_j\right)\right]^2 / \sigma^2_{i(Q)} \tag{2.24}$$

$$\chi^2_{\mathrm{Bragg}} = \sum_l \left[y_{\mathrm{calc}}(d_l) - y_{\mathrm{exp}}(d_l)\right]^2 / \sigma^2_{y(d)} \tag{2.25}$$

where the functions $D(r)$ and $i(Q)$ have been defined above, the function $y(d)$ is the Bragg scattering as a function of $d$-spacing (or as a function of neutron flight time for TOF diffractometers), and the $\sigma^2$ parameters in principle should reflect the experimental error. In practice the $\sigma^2$ parameters are set to a constant value for all data points in a given experimental function. By tuning the parameter $\sigma$, a particular experimental data set can be emphasised or de-emphasised in the total $\chi^2_{\mathrm{RMC}}$ energy function. For example, if the $\sigma$ value for the Bragg data is set as 0.01 and for all other experimental data are set as 0.1. The goodness of fit of the Bragg data will wight 10 times bigger than any other experimental data in the overall refinement. The function $\chi^2_{\mathrm{energy}}$ reflects the constraint terms to assist the RMC process. There are various constraints available in the RMC program RMCProfile. [51] The most commonly used constraints include bond stretch and

bond angle potential. The potential part in the function $\chi^2_{\text{energy}}$ is defined as:

$$\chi^2_{\text{energy}} = \sum_i E_i / k_{\text{B}} T \tag{2.26}$$

where $T$ is the nominal temperature (which ideally will be the temperature of the experiment if the potential energy functions are realistic), and $E_i$ is the potential energy function.

During the RMC process, as shown in Fig. 2.5, if an atomic move lowers the value of $\chi^2_{\text{RMC}}$ it is automatically accepted. If it raises the value of $\chi^2_{\text{RMC}}$, it is accepted with probability $\exp(-\chi^2_{\text{RMC}}/2)$. In this sense, $\chi^2_{\text{RMC}}$ plays the role of energy divided by temperature as used in conventional Monte Carlo simulations of condensed matter, where the values of $\sigma^2$ in the defintions play the role of temperature (that is, larger values of $\sigma^2$ permit large fluctuations).

When the $\chi^2_{\text{RMC}}$ is decreased to a stable value and the calculated data patterns are in good agreement with the experimental counterparts, the resulting configuration can be accepted as the final refined RMC configuration. Usually at this stage, the RMC process has been repeated millions of times, so that in the end there are tens or hundred of accepted moves per atom.

Each RMC configuration can be treated as an instantaneous snapshot of the atomic structure of the material across many unit cells. This snapshot directly shows how the atoms are displaced from their crystallographic sites, in other words, reflecting local fluctuations and disorder at a molecular level. Moreover, the multi-unit cell nature of the RMC configuration makes it possible to quantitatively analyse the statistical distribution of atomic positions and molecular orientations. Many previous studies have demonstrated how this method can be applied to study effects including bond anharmonicity [52], distortions of coordination polyhedra [48] and host-guest interactions in framework materials [7], as well as orientational disorder [53].

## 2.5 Molecular dynamics

The molecular dynamics method (MD) is a virtual atom experiment in which the atoms under a specific condition (the ensemble) move according to a series of pre-defined equations of motions (empirical potentials) [54]. The very heart of molecular dynamics is Newtonian mechanics. All the MD simulations in this thesis are performed with the software DL_POLY4 [55].

### 2.5.1 Empirical potentials

#### Coulomb interaction

For atoms with charges, the main force to hold them together is the electrostatic Coulomb interaction. This interaction in molecular dynamics is described as:

$$U\left(r_{ij}\right) = \frac{Q_i Q_j}{4\pi\epsilon_0 r_{ij}} \tag{2.27}$$

where $U\left(r_{ij}\right)$ is the potential energy, $r_{ij}$ is the distance between atom $i$ and atom $j$, $Q_i$ and $Q_j$ are the charge for atom $i$ and atom $j$ respectively and $\epsilon_0$ is the vacuum permittivity [56].

#### Buckingham potential

The Buckingham potential is composed by a repulsive term and an attractive term. I used the Buckingham potential as the intermolecular potential for the work presented in this thesis. The Buckingham potential is :

$$U\left(r_{ij}\right) = -\frac{C_{ij}}{r_{ij}^6} + B_{ij}\exp\left(-r_{ij}/\rho_{ij}\right) \tag{2.28}$$

where $C_{ij}$ is the coefficient for the long range attractive term and $B_{ij}$ is the coefficient for the short range repulsive term [29].

**Covalent interaction**

The covalent interaction is a strong bonding from overlapping electrons. It plays an important role in defining a molecule or a rigid unit as well as characterizing the interactions between neighbouring molecules or rigit units. For example, a C atom in a methyl and a N atom in an ammonium connected by a covalent bond forms a methylammonium ion. The covalent bond strength determines how rigid a methylammonium ion is. The basic potential to represent the covalent bond between two atoms is often described with a Morse potential [54]:

$$U_{\text{stretch}}(r) = \epsilon \left[\exp\left(2\alpha\left(r - r_0\right)\right) - 2\exp\left(\alpha\left(r - r_0\right)\right)\right] \tag{2.29}$$

where $r_0$ is the equilibrium distance and $\epsilon$ is the energy at $r_0$ and $\alpha$ is related to the curvature around the minimum of the potential well.

The angle potential between two bonds, characterizing how easy it can be bent, is usually described with a harmonic 3-body potential [54]:

$$U_{\text{angle}}(\theta) = \frac{k}{2}\left(\theta - \theta_0\right)^2 \tag{2.30}$$

where $\theta_0$ is the equilibrium angle and $k$ is the bending energy.

Sometimes it is important to add a potential to describe the torsion of a dihedral angle illustated in Fig. 2.6. Specifically, the torsion potential is important to characterize the behaviour of the 4,4′-biphenyl molecule in the work presented in chapter 5 of this thesis. This torsion potential can be expressed as [54]:

$$U\left(\phi_{ijkn}\right) = A\left[1 + \cos\left(m\phi_{ijkn} - \delta\right)\right] \tag{2.31}$$

where $A$ is the torsion energy, $m$ is the multiplicity i.e. how many minima during a 360° cycle and $\delta$ is the phase factor determining the positions of the minima.

### 2.5.2 Ensembles

The virtual atom experiment MD needs to be carried out under a pre-defined condition known as the ensemble. The first developed ensemble is the NVE

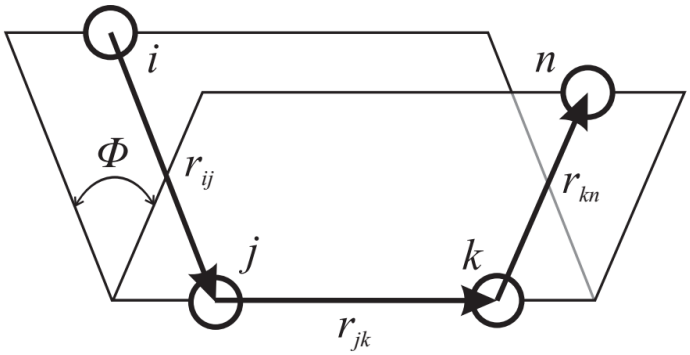


Figure 2.6: An illustration of the dihedral angle. Four atoms form 3 bonds and the adjacent 2 bonds form two planes. The angle between the two planes i-j-k and j-k-n is the dihedral angle $\Phi$

ensemble i.e. constant number of atoms, constant volume and constant energy. This is only suitable to study a closed system. More often, the materials exist in nature under a condition of constant temperature and constant pressure. This leads to the development the ensemble of NPT. Sometimes in phase transition studies, the size and the shape of the atomic configuration is required to change in order to accommodate the set temperature. In this situation, the best candidate ensemble is NST i.e. constant number of atoms, constant stress and constant temperature [56]. In the works presented in this thesis, I used NPT ensemble to preserve the cubic shape and used NST ensemble to study how the geometry of structure changes across phase transitions. NVE ensemble is also used in the PAF-1 case to study the dynamics.

## 2.6 Analysis of big-box atomic configurations

### 2.6.1 Spherical harmonics and symmetry adapted functions

The orientation of a molecule or a rigid unit can be represented by the spherical harmonics. Spherical harmonics are a set of orthogonal basis functions as a

function of polar angles $\theta$ and $\phi$[5] defined on a spherical surface [57]. The basis function are parameterised by two integers $\ell$ and $m$, where $\ell = 0, 1, 2, \ldots$ and $m = 0, \pm 1, \pm 2, \ldots, \pm \ell$. Any function $f(\theta, \phi)$ defined on a spherical surface can be expanded as a linear combination of the spherical harmonics just like the Taylor expansion in Cartesian coordinates.

$$f(\theta,\phi) = c_{0,0}Y_0^0(\theta,\phi) + c_{1,-1}Y_1^{-1}(\theta,\phi) + c_{1,0}Y_1^0(\theta,\phi) + c_{1,1}Y_1^1(\theta,\phi) + \ldots \quad (2.32)$$

Where $c_{l,m}$ is the linear combination coefficient for $Y_{l,m}$.

Sometimes, the orientational distribution for molecules or rigid units can be described quantitatively by a dipole vector (can simply be a bond vector or a vector elaborately defined in some way) orientation distribution function $P(\Omega)$[58, 59]. Here $\Omega$ represents the polar angles $(\theta, \phi)$. The orientation distribution function $P(\Omega)$ can be expanded with a set of orthogonal "rotator functions" $S_i(\Omega)$,

$$P(\Omega) = \sum_i c_i S_i(\Omega) \quad (2.33)$$

and the "rotator functions" $S_i(\Omega)$ themselves are linear combinations of spherical harmonics $Y_\ell^m(\Omega)$. These can be symmetry adapted functions or simply the real combinations of spherical harmonics such as:

$$Y_\ell^{m,c}(\theta,\phi) = \tfrac{1}{\sqrt{2}}\left(Y_\ell^m + Y_\ell^{-m}\right) \quad (2.34)$$

$$Y_\ell^{m,s}(\theta,\phi) = -\tfrac{\mathrm{i}}{\sqrt{2}}\left(Y_\ell^m - Y_\ell^{-m}\right) \quad (2.35)$$

where $Y_\ell^{m,c} \propto \cos(m\phi)$ and $Y_\ell^{m,s} \propto \sin(m\phi)$ [60].

From MD or RMC configurations, it is feasible to obtain a series of orientation values $(\theta_i, \phi_i)$ for molecules or rigid units. These orientation values can be treated as a sum of delta functions $\sum_i \delta(\theta - \theta_i, \phi - \phi_i)$ and the linear combination

[5]Physics and mathematics use opposite conventions for the angles $\theta$ and $\phi$. In my research I use the "physics" convention that $\theta$ is the zenith angle, measured from the $z$ axis and running from 0 to $\pi$, while $\phi$ is the azimuthal angle, measured from the $x$ axis and running from 0 to $2\pi$. The "mathematics" convention is exactly the opposite.

coefficients can be calculated according to:

$$c_{\ell,m,x} = \sum_i Y_\ell^{m,x}(\theta_i, \phi_i) \tag{2.36}$$

where $x = c, s$.

The existence of symmetry makes some coefficients of the spherical harmonics zero. In other words, only certain $Y_\ell^m(\Omega)$ terms are allowed by the symmetry and the symmetry adapted functions are the combinations of the allowed spherical harmonic. These combinations are usually mathematically simple except the cubic symmetry where the threefold axes at an angle to the polar axis make its symmetry adapted functions (usually called the cubic harmonics) rather complicated. The first five cubic harmonics functions in both Cartesian and polar form are given below. The Cartesian form [61] differs by a factor of $\sqrt{4\pi}$ from the polar form[60].

$$K_0 = 1 \qquad = \sqrt{4\pi}(Y_0^0) \tag{2.37a}$$

$$K_4 = \frac{\sqrt{21}}{4}(5Q - 3) \qquad = \sqrt{4\pi}\left(\sqrt{\frac{7}{12}}Y_4^0 + \sqrt{\frac{5}{12}}Y_4^{4,c}\right) \tag{2.37b}$$

$$K_6 = \frac{\sqrt{13}}{8\sqrt{2}}(462S + 21Q - 17) \qquad = \sqrt{4\pi}\left(\sqrt{\frac{1}{8}}Y_6^0 - \sqrt{\frac{7}{8}}Y_6^{4,c}\right) \tag{2.37c}$$

$$K_8 = \frac{\sqrt{561}}{32}(65Q^2 - 208S - 94Q + 33) \qquad = \sqrt{4\pi}\left(\sqrt{\frac{99}{192}}Y_8^0 + \sqrt{\frac{28}{192}}Y_8^{4,c} + \sqrt{\frac{65}{192}}Y_8^{8,c}\right) \tag{2.37d}$$

$$K_{10} = \frac{\sqrt{455}}{64\sqrt{2}}(7106QS + 187Q^2 - 3190S - 264Q + 85) \qquad = \sqrt{4\pi}\left(\sqrt{\frac{65}{384}}Y_{10}^0 - \sqrt{\frac{132}{384}}Y_{10}^{4,c} - \sqrt{\frac{187}{384}}Y_{10}^{8,c}\right) \tag{2.37e}$$

In the Cartesian equations, $Q = x^4 + y^4 + z^4$ and $S = x^2y^2z^2$, where $x = \sin\theta\cos\phi$, $y = \sin\theta\sin\phi$ and $z = \cos\theta$.

Once the coefficient of the basis functions are determined, the orientation probability can be calculated at any designated polar angle. This makes the spherical harmonics and symmetry adapted functions powerful tools to study the

orientational disorder quantitatively. There are lots of examples to demonstrate this in chapter 3 and chapter 4 of this thesis.

### 2.6.2 Polyhedra geometric analysis

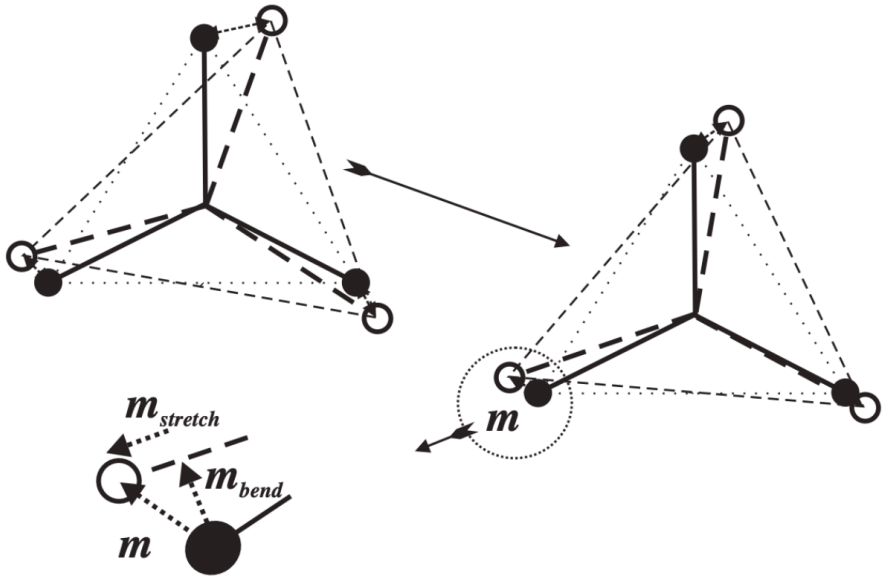


Figure 2.7: The mismatch factors are calculated from 3 terms. The first term, $m_{rotation}$, comes from finding the best-fit of the polyhedra whole body rotations. The residue mismatch are then separated into the bond bending term $m_{bend}$, and the bond stretching terms $m_{stretch}$ [62].

In structure analysis, the atoms in rigid unit ions such as $NH_4^+$ are usually considered as a whole in the form of polyhedra. On one hand, the polyhedra may displace or rotate as rigid units. On the other hand, the polyhedra may have distortion within themselves due to bond bending or stretching.

The software Geometric Analysis of Structural Polyhedra (GASP) can be used to quantitatively analyse such disorder behaviours of rigid units polyhedra. The essential idea of GASP is to compare each polyhedron with its ideal regular counterpart and measure their geometric mismatch. As shown in Fig. 2.7, the overall mismatch factor can be divided into 3 terms, whole body rotation, bond bend, and bond stretch. Hence, this analysis is able to provide not only information

about how the polyhedra deviate from the ideal regular polyhedra, but also information about the contributions of different kinds of geometry changes to the overall mismatch.

### 2.6.3 Pseudo-dipole analysis

A rigid unit polyhedron in real structures is not necessarily to be in an ideal regular shape. It may have distortion within the polyhedra. One way to characterize such distortion is to define a pseudo-dipole moment as a sum of bond vectors. Taking the ammonium ion $NH_4^+$ as an example, the centre atom N are surrounded by 4 H atoms. The bond vectors are defined as the position coordinates of the surrounding atom subtracting the coordinates of the centre atom. In this case, the bond vectors are

$$\mathrm{ND_i} = \mathrm{D}_i(x, y, z) - \mathrm{N}(x, y, z) \tag{2.38}$$

where i = 1,2,3,4. The sum of the bond vectors gives the pseudo-dipole moment of the ammonium ion $NH_4^+$:

$$\delta = \sum_i \mathrm{ND_i} \tag{2.39}$$

The modulus of the pseudo-dipole moment i.e. the distance deviation between the real shape centre and the ideal shape centre, can be used as an indicator to characterize the extent of distortion in a polyhedron.

# Chapter 3

# Orientational disorder in potassium cyanide KCN

## 3.1 Introduction

Orientational disorder is a common phenomenon in molecular crystals or inorganic crystals.[1] Often, at least in the first phases found on cooling below the melting point, the disorder is dynamic, with the molecules or molecular ions undergoing rotational motion across a continuous distribution of molecular orientations, or jump rotations between a well-defined set of distinct orientations.

One simple and intensively studied case is that of the cyanide ion, $CN^-$, in metal cyanides [63]. $CN^-$ exhibits two types of orientational disorder in metal cyanides. In the cristobalite-like group-12 metal cyanides $Zn(CN)_2$ [64] and $Cd(CN)_2$ [65], the cyanide ions can be treated as electric dipoles with static head-to-tail orientational disorder. Apparently this disorder persists to low temperature in $Zn(CN)_2$, but recently reorientational motion and short-range order have been identified in

[1] In the past orientationally-disordered materials were called 'plastic crystals' as a result of their mechanical properties, but the scientific community later preferred the term use here. However, as orientationally disordered crystals have come back into fashion, sometimes people are rediscovering the older name! For the good reasons why the name 'plastic crystals' was replaced by the name 'orientionally disordered crystals' choose to work with the latter name.

$Cd(CN)_2$ [65]. On the other hand, in the alkali metal cyanides NaCN, KCN and RbCN with the rocksalt structure, the cyanide molecular ions have a much broader distribution of orientations and show rotational freedom [66] rather than jump motions [67]. In fact, the first phase transition on cooling after freezing involves ordering of the elastic quadrupole moments rather than of the molecular electrical dipole moments.

The metal cyanide metals has been well studied since 1980s. Nevertheless it's regathering momentums because of the orientational disorder of the cyanide ions is analogous to the organic ions in hybrid perovskite. One example is the hybrid perovskite solar cell material methylammonium lead iodide ($MAPbI_3$), which has been investigated in a huge number of studies, yet still facing the problem of characterising the orientational disorder from experimental data. $MAPbI_3$ undergoes two phase transitions at ambient pressure involving changes in the degree of orientational order, and it has been shown that these correlate with its temperature-dependent dielectric properties [10]. The methylammonium includes a C–N bond, a direct analogue of the cyanide ion in KCN, for example, and indeed a recent study by molecular dynamics simulation of $MAPbI_3$ compared the ordering to that of KCN from single-crystal diffraction, suggesting that the methylammonium ions are somewhat more isotropic, although again the spherical harmonic expansion was terminated at very low order [11]. For these reasons it is timely to revisit the once landmark metal cyanide, potassium cyanide KCN.

### 3.1.1 The phase transitions in KCN

Below its melting point (907 K), potassium cyanide exists in three distinct crystalline phases. From 168 K up to its melting point, KCN has the well-known rock salt structure with space group $Fm\bar{3}m$ [68]. The cyanide anions occupy sites of the full cubic point symmetry ($m\bar{3}m$) and therefore there is three-dimensional

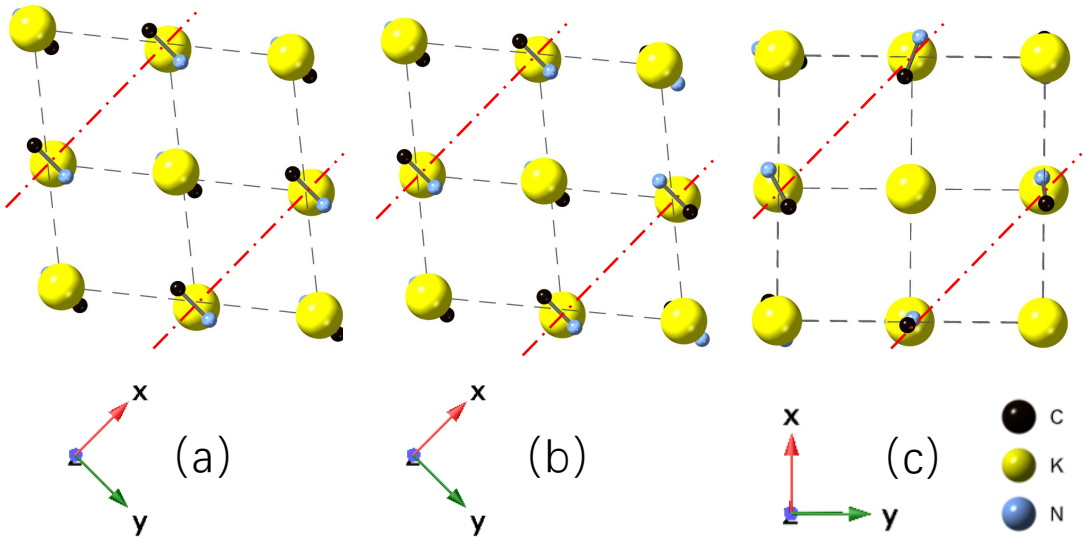


Figure 3.1: The structure of KCN view from the c axis in (a) the low temperature phase (below 83 K), (b) the intermediate temperature phase (83 K to 168 K) and (c) the high temperature phase (above 168 K) with black, cyan and yellow balls representing carbon, nitrogen and potassium atoms respectively. The gray lines represent a pseudo rhombohedral or a cubic cell containing the same set of atoms. In the low temperature phase, the cyanide ions align along the y axis with the same direction within one layer(shown as red dashed lines) and adjacent layers point at opposite directions. This is known as head to tail order. In the intermediate phase, the cyanide ions lose head-to-tail order while still aligning along the $b$ axis. In the high temperature phase, the cyanides are no longer restrained to align along $b$ and orient randomly over the full unit sphere.

orientational disorder. At 168 K there is a phase transition involving considerable but not complete ordering of the cyanide orientations. The crystal structure of this phase is orthorhombic, space group $Immm$. The cyanide anions have their long axes parallel to the orthorhombic [010] axis (equivalent to the $\langle 110 \rangle$ axes in the cubic phase) but with head-to-tail disorder of the electric dipoles [69, 70]. The ordering can be described as involving the molecular quadrupole moments. It is well established that the ordering couples linearly to the softening of the $C_{44}$ shear elastic constant as a result of coupling between the translations and rotations [14, 71–75], meaning that the phase transition is a proper ferroelastic phase transition. At 83 K there is a second phase transition to a fully-ordered

structure of orthorhombic space group *Pmnm*. This has ordering of the electric dipole moments in a proper antiferroelectric arrangement [13, 76].

The atomic structures of the three crystalline phases of KCN are illustrated in Fig. 3.1. This figure shows the relationship between the phases, and illustrates the change in orientational ordering.

## 3.2 Experimental and analysis methods

### 3.2.1 Neutron scattering measurements

Two sets of neutron scattering experiments were performed in this study measured by Prof. Martin Dove. A set of neutron powder diffraction measurements were performed using a 10-detector array on the E13 spectrometer on the NRU nuclear reactor at the Chalk River Laboratories. The second set were a combination of neutron diffraction and total scattering measurements performed on the GEM diffractometer at the ISIS pulsed spallation neutron source in the UK. The data from ISIS are publicly available [2]. The data reduction for the NRU data was performed using in-house software, and for the ISIS data using the MANTID software. More details of the data collection can be found from Prof. Martin Dove.

In both cases the sample was contained within a thin-walled vanadium can, with temperature controlled by a standard cryostat. The samples were obtained commercially.

### 3.2.2 Analysis of diffraction data

The crystal structures of KCN were refined using the the `GSAS`/`EXPGUI` programs. Starting coordinates for the intermediate temperature phase were taken from literature values with disordered occupancy of the C/N sites. For the low-temperature

[2]The data can be accessed with DOI 10.5286/ISIS.E.RB13786.

phase the structure was taken as an antiferroelectic ordering of the electric dipole moments of the intermediate-temperature phase. The disordered high-temperature phase has no well-defined positions for the C/N atoms, but nevertheless such positions are required for standard Rietveld analysis and so were selected to lie parallel to the cubic unit cell axes.

### 3.2.3 Total scattering data and the Reverse Monte Carlo analysis

The total scattering data were transformed to the appropriate scattering functions $i(Q)$ and pair distribution functions $D(r)$ using standard procedures introduced in Section 2.3. The data correction, normalization and Fourier transform are all done using the `GUDRUN` package.

The Reverse Monte Carlo simulation was performed using the `RMCprofile` code [51]. Configurations of the low-temperature phase used a $12 \times 10 \times 8$ supercell based on the refined crystal structure, set up using the `data2config`/`RMCcreate` code [77]. The configuration for the intermediate-temperature phase was set up in a similar manner, but using an option to randomly rotate the cyanide molecular ions by 180° about the normal to the molecular axis. The configuration for the cubic phase was a $8 \times 8 \times 8$ supercell of the cubic phase, using an option to give each cyanide molecular ion a random orientation. The RMC simulations were carried out for 2315263 steps in total until convergence (see Fig. 3.2d, giving 70.1 accepted moves per atom and an average move acceptance rate of 18.6%. For each temperature I generated 100 independent configurations for analysis.

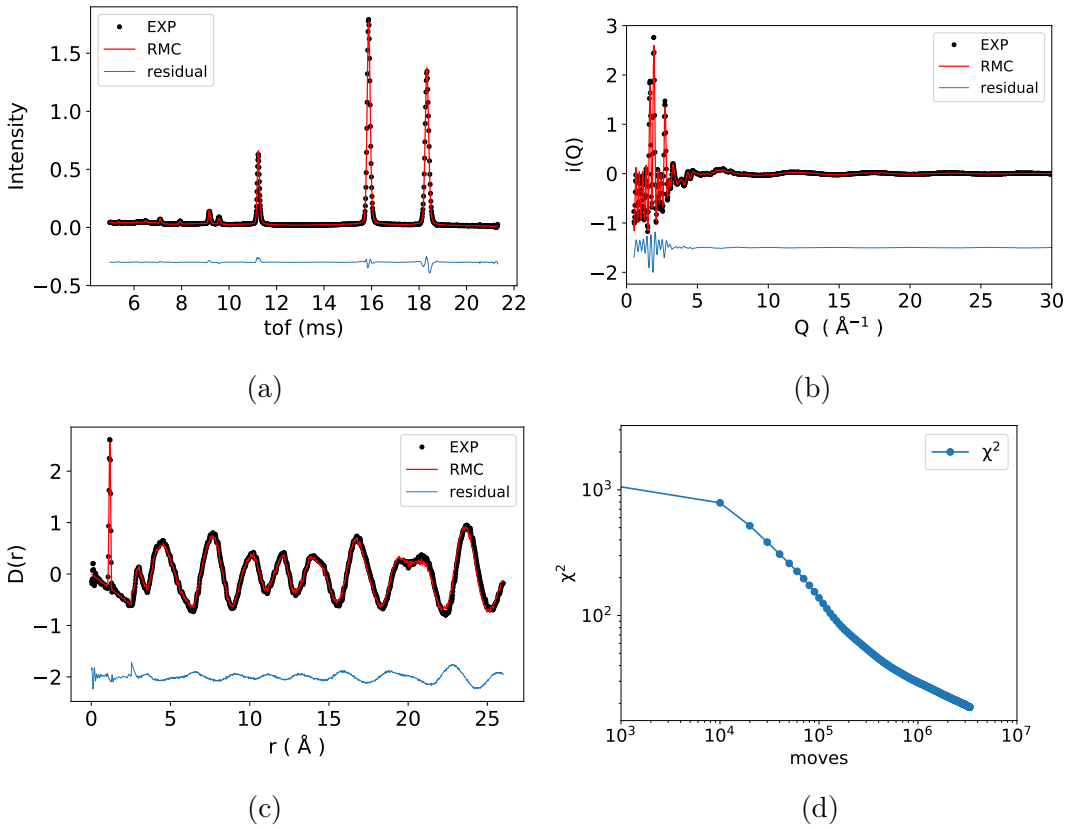


Figure 3.2: Representative fits from RMC simulation at 250 K of (a) Bragg pattern, (b) total scattering function and (c) pair distribution function. (d) shows the variation of total $\chi^2$ in RMC with number of RMC moves proposed in a log-log scale.

## 3.3 Rietveld analysis of KCN: lattice parameters and spontaneous strain

The atomic structure of the ordered $Pmnm$ phase has atomic coordinates K $(\frac{1}{4}, \frac{1}{4} - u_{\mathrm{K}}, \frac{1}{4})$, C $(\frac{3}{4}, y_{\mathrm{C}}, \frac{1}{4})$ and N $(\frac{3}{4}, y_{\mathrm{N}}, \frac{1}{4})$. The atomic structure of the partially-ordered $Immm$ phase has atomic coordinates K $(0, 0, 0)$ and C/N $(0, u, \frac{1}{2})$, with fractional occupancy of 0.5 for both atom types. The atomic structure of the disordered $Fm\bar{3}m$ phase has K $(0, 0, 0)$, and in the refinement the coordinates for C/N are set of the form $(\frac{1}{2}, u, 0)$ with fractional occupancy of 1/12 for both atom types, as an over-simplified model in order to be able extract lattice parameters. Results for the crystal structure of all three phases refined from the GEM data

are given in Table 3.1–Table 3.3.

Table 3.1: Crystal structure data for the low-temperature ordered phase of KCN, space group symmetry $Pmnm$ (number 59). Atomic coordinates are of the form $(\frac{1}{4}, y, \frac{1}{4})$ for atom type K, and of the form $(\frac{3}{4}, y, \frac{1}{4})$ for atom types C and N. These results were obtained by Rietveld refinement of the diffraction data from the GEM diffractometer at ISIS.

| $T$ (K) | $a$ (Å) | $b$ (Å) | $c$ (Å) | atom | $y$ | $U_{11}$ (Å$^2$) | $U_{22}$ (Å$^2$) | $U_{33}$ (Å$^2$) | $R_{wp}$ (%) |
|---|---|---|---|---|---|---|---|---|---|
| 20 | 4.18631(3) | 5.24579(5) | 6.07488(5) | K | 0.2283(4) | 0.87(4) | 1.46(7) | 0.91(4) | 5.09 |
| | | | | C | 0.6418(2) | 1.81(6) | 1.07(6) | 1.21(6) | — |
| | | | | N | 0.8610(2) | 1.87(4) | 1.39(5) | 1.80(5) | — |
| 25 | 4.18670(3) | 5.24515(5) | 6.07527(5) | K | 0.2289(5) | 0.99(5) | 1.58(8) | 0.89(4) | 5.12 |
| | | | | C | 0.6417(2) | 1.90(7) | 1.14(7) | 1.13(7) | — |
| | | | | N | 0.8610(2) | 1.89(5) | 1.38(5) | 1.94(6) | — |
| 30 | 4.18718(3) | 5.24411(6) | 6.07605(5) | K | 0.2284(4) | 1.05(5) | 1.68(8) | 1.00(5) | 5.17 |
| | | | | C | 0.6418(2) | 1.94(7) | 1.00(7) | 1.36(7) | — |
| | | | | N | 0.8609(1) | 1.96(5) | 1.55(5) | 1.90(6) | — |
| 35 | 4.19026(3) | 5.23884(5) | 6.08012(5) | K | 0.2288(5) | 1.20(5) | 1.86(9) | 1.13(5) | 4.96 |
| | | | | C | 0.6427(3) | 2.14(7) | 1.57(9) | 1.37(7) | — |
| | | | | N | 0.8614(2) | 2.16(5) | 1.33(7) | 2.10(6) | — |
| 40 | 4.19018(3) | 5.23923(5) | 6.07983(5) | K | 0.2287(4) | 1.10(5) | 1.68(8) | 1.00(5) | 5.04 |
| | | | | C | 0.6418(2) | 2.17(7) | 1.28(7) | 1.38(7) | — |
| | | | | N | 0.8610(2) | 2.20(5) | 1.60(5) | 2.12(6) | — |
| 45 | 4.19027(3) | 5.23908(5) | 6.07989(5) | K | 0.2282(4) | 0.97(6) | 1.60(8) | 0.98(5) | 5.01 |
| | | | | C | 0.6424(2) | 2.21(7) | 1.14(7) | 1.49(7) | — |
| | | | | N | 0.8612(2) | 2.16(5) | 1.71(5) | 2.03(6) | — |
| 50 | 4.19249(3) | 5.23546(5) | 6.08365(5) | K | 0.2298(4) | 1.14(4) | 1.83(6) | 1.10(4) | 4.89 |
| | | | | C | 0.6420(2) | 2.19(6) | 1.19(6) | 1.34(6) | — |
| | | | | N | 0.8612(1) | 2.31(5) | 1.82(5) | 2.24(5) | — |

Table 3.2: Crystal structure data for the intermediate-temperature partially-ordered phase of KCN, space group symmetry $Immm$ (number 71). K has atomic coordinates $(0, 0, 0)$. C and N have atomic coordinates of the form $(0, y, \frac{1}{2})$, both with occupancy 0.5. These results were obtained by Rietveld refinement of the diffraction data from the GEM diffractometer at ISIS.

| $T$ (K) | $a$ (Å) | $b$ (Å) | $c$ (Å) | atom | $y$ | $U_{11}$ (Å$^2$) | $U_{22}$ (Å$^2$) | $U_{33}$ (Å$^2$) | $R_{wp}$ (%) |
|---|---|---|---|---|---|---|---|---|---|
| 100 | 4.22003(3) | 5.19426(5) | 6.13157(5) | K | — | 2.19(2) | — | — | 4.24 |
| | | | | C/N | 0.11061(6) | 3.76(2) | 3.15(2) | 2.98(2) | — |
| 110 | 4.22139(4) | 5.19228(6) | 6.13314(5) | K | — | 2.24(2) | — | — | 4.70 |
| | | | | C/N | 0.11036(7) | 3.85(2) | 3.21(2) | 3.09(2) | — |
| 120 | 4.22576(4) | 5.18662(7) | 6.13820(5) | K | — | 2.34(2) | — | — | 4.70 |
| | | | | C/N | 0.11034(7) | 4.08(2) | 3.33(2) | 3.25(2) | — |
| 130 | 4.23341(4) | 5.17663(6) | 6.14660(5) | K | — | 2.55(2) | — | — | 4.53 |
| | | | | C/N | 0.10997(7) | 4.51(2) | 3.50(2) | 3.54(2) | — |
| 140 | 4.25204(6) | 5.15108(10) | 6.16599(8) | K | — | 2.69(4) | — | — | 7.05 |
| | | | | C/N | 0.10929(10) | 4.65(4) | 3.36(3) | 3.75(3) | — |
| 150 | 4.25404(4) | 5.14872(7) | 6.16798(5) | K | — | 2.94(3) | — | — | 4.28 |
| | | | | C/N | 0.10893(8) | 5.30(3) | 4.10(3) | 4.14(3) | — |
| 160 | 4.26060(4) | 5.13946(8) | 6.17461(6) | K | — | 3.17(3) | — | — | 4.31 |
| | | | | C/N | 0.10857(8) | 5.70(3) | 4.33(3) | 4.47(3) | — |
| 170 | 4.26992(4) | 5.12587(8) | 6.18355(6) | K | — | 3.33(3) | — | — | 4.22 |
| | | | | C/N | 0.10795(9) | 6.14(3) | 4.65(3) | 4.66(3) | — |
| 180 | 4.28194(5) | 5.10774(10) | 6.19551(7) | K | — | 3.61(4) | — | — | 5.02 |
| | | | | C/N | 0.10723(12) | 6.61(4) | 4.93(4) | 5.03(4) | — |

Table 3.3: Crystal structure data for the intermediate-temperature partially-ordered phase of KCN, space group symmetry $Fm\bar{3}m$ (number 225). K has atomic coordinates $(0, 0, 0)$. C and N have atomic coordinates of the form $(\frac{1}{2}, y, \frac{1}{2})$, both with occupancy 0.5. These results were obtained by Rietveld refinement of the diffraction data from the GEM diffractometer at ISIS.

| $T$ (K) | $a$ (Å) | $b$ (Å) | $c$ (Å) | atom | $y$ | $U_{11}$ (Å$^2$) | $U_{22}$ (Å$^2$) | $U_{33}$ (Å$^2$) | $R_{wp}$ (%) |
|---|---|---|---|---|---|---|---|---|---|
| 200 | 6.48790(3) | — | — | K | — | 7.23(4) | — | — | 2.76 |
| | | | | C/N | 0.4187(2) | 10.95(9) | 6.80(9) | 10.95(9) | — |
| 210 | 6.48880(3) | — | — | K | — | 7.38(5) | — | — | 3.49 |
| | | | | C/N | 0.4183(3) | 10.95(11) | 6.90(11) | 10.95(11) | — |
| 220 | 6.49152(3) | — | — | K | — | 7.31(5) | — | — | 3.31 |
| | | | | C/N | 0.4197(3) | 11.46(11) | 7.15(11) | 11.46(11) | — |
| 230 | 6.49451(3) | — | — | K | — | 7.37(4) | — | — | 3.25 |
| | | | | C/N | 0.4187(3) | 11.14(10) | 6.90(10) | 11.14(10) | — |
| 240 | 6.49763(3) | — | — | K | — | 7.27(5) | — | — | 3.19 |
| | | | | C/N | 0.4198(3) | 11.50(10) | 6.76(10) | 11.50(10) | — |
| 250 | 6.50285(2) | — | — | K | — | 7.16(3) | — | — | 5.36 |
| | | | | C/N | 0.4205(2) | 11.63(10) | 6.61(10) | 11.63(10) | — |

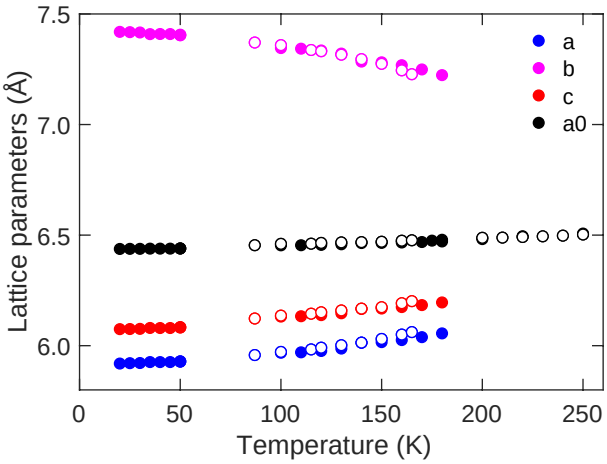


(a)

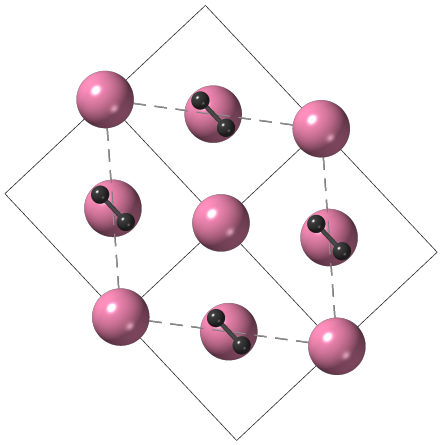

(b)

Figure 3.3: (a) Lattice parameters of KCN. In this diagram the values of $a$ (blue points) and $b$ (magenta points) have been multiplied by $\sqrt{2}$ in order to compare better with the data for the $c$ axis (red points) and the values of the cubic lattice parameter (black points). The cubic values extrapolated below the temperature of the cubic phase are obtained from $(abc)^{1/3}$, using the scaled values. Filled circles represent data from ISIS, and open circles represent data from Chalk River Laboratories. (b) Crystal structure of the intermediate-temperature KCN of space group $Immm$, viewed down the orthorhombic $c$ axis. The large pink atoms are potassium, and the small grey dumbbells represent the cyanide anions with head-to-tail disorder. The orthorhombic $b$ axis is parallel to the orientations of the cyanide anions. The thin lines give the outline of the orthorhombic unit cell with orthogonal axes. The dashed line represents the unit cell that corresponds to the cubic face-centred lattice, with axes rotated by 45° about the orthorhombic $c$ axis.

The variations of the lattice parameters of the cubic and orthorhombic phases with temperature are shown in Fig. 3.3a, using the scaled parameters $a' = \sqrt{2}a$ and $b' = \sqrt{2}b$ for the orthorhombic phase in order to give values that will tend towards the value of the lattice parameter of the cubic phase. It is striking that the volume of the unit cell appears to show no change in passing through the cubic–orthorhombic phase transition. Therefore a parameter $a_0 = (a'b'c)^{1/3}$ is defined , such that $a_0$ acts as the extrapolation of the cubic $a$ lattice parameter to low temperature. To interpret the lattice parameters, it is instructive to look at the crystal structure viewed down the orthorhombic $c$ axis, Fig. 3.3b. The cyanide anions orient along one of the cubic $\langle 110 \rangle$ axes, which corresponds to the

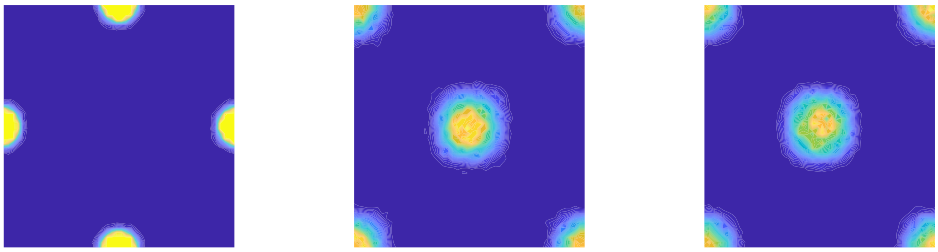

(a) K atoms (b) C atoms (c) N atoms

Figure 3.4: Representation of the atomic density within a slice of one unit cell viewed down the [001] direction for fractional coordinates $0.4 < z < 0.6$. The vertical direction of the figure corresponds to the [100] direction of the unit cell for fractional coordinates $0 < x < 1$. The horizontal direction of the figure corresponds to the [010] direction of the unit cell for fractional coordinates $0 < y < 1$. (a)–(c) shows the atomic density for each atom type at 200K. Yellow indicates the maximum values of the atomic density, and deep blue indicates the minimum values of the atomic density.

orthorhombic $b$ axis. This leads to an expansion of the $b$ lattice parameter on cooling compared with its value in the cubic phase, with a corresponding reduction in the size of the $a$ and $c$ axes.

## 3.4 Orientational order and local atomic structure from neutron total scattering and RMC simulation

### 3.4.1 Atomic distributions

The spatial distribution of individual atoms in the unit cell was constructed by collapsing each configuration onto one unit cell, and merging the results from many independent RMC simulations. Fig. 3.4a–c shows the density profile for each atom type at the cubic phase. Fig. 3.4a reflects the large amount of thermal motion of the K atom as seen in the size of the atomic displacement parameter

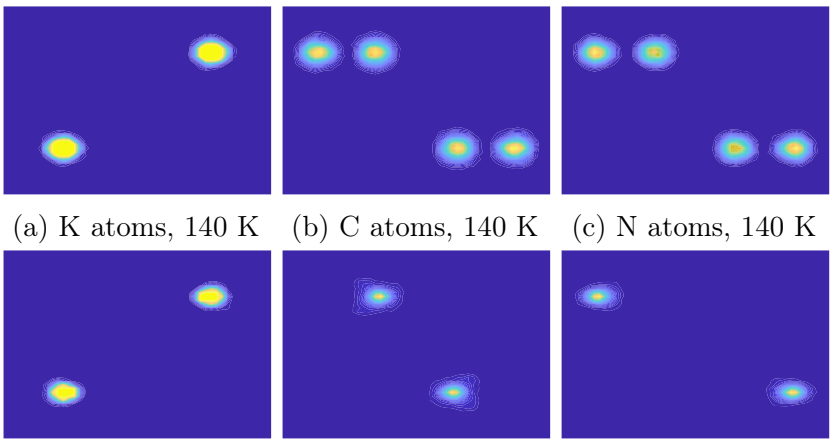

(a) K atoms, 140 K (b) C atoms, 140 K (c) N atoms, 140 K

(d) K atoms, 20 K (e) C atoms, 20 K (f) N atoms, 20 K

Figure 3.5: Representation of the atomic density within a slice of one unit cell viewed down the [001] direction for fractional coordinates $0.4 < z < 0.6$. The vertical direction of the figure corresponds to the [100] direction of the unit cell for fractional coordinates $0 < x < 1$. The horizontal direction of the figure corresponds to the [010] direction of the unit cell for fractional coordinates $0 < y < 1$. (a)–(c) shows the atomic density for each atom type at 140K. Yellow indicates the maximum values of the atomic density, and deep blue indicates the minimum values of the atomic density. (d)–(f) shows the atomic density for each atom type at 20 K.

from the Rietveld analysis, Table 3.2. The distribution of C and N atoms is wider in extent. What is interesting from Fig. 3.4b and Fig. 3.4c are that the distribution of C and N atoms are centred in the middle of the unit cell, rather than the distribution of C and N atoms forming a spherical shell. Thus the orientational disorder is accompanied by a high degree of translational disorder.

The corresponding atomic distributions for the intermediate-temperature (100 K) partially-ordered $Immm$ phase are shown in Fig. 3.5a–c, and for the low-temperature (20 K) ordered $Pmnm$ phase in Fig. 3.5d–f. The reduction in translation disorder is clear, and the sites for C and N atoms are distinct. In the intermediate phase there is head-to-tail disorder of the cyanide molecular ions, which is clearly seen in the distribution of C and N atoms.

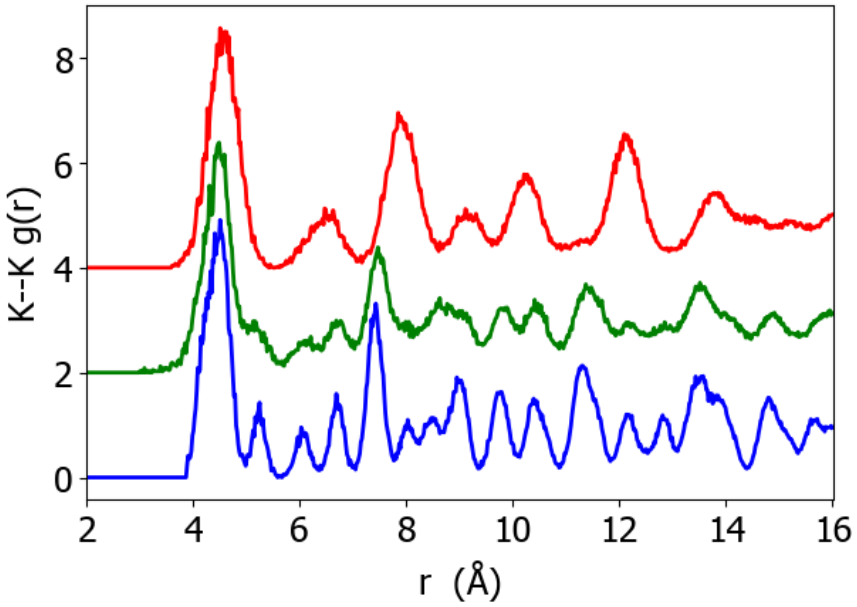


Figure 3.6: K–K partial PDF $g(r)$ for temperatures 20 K (blue), 100 K (green), 200 K (red), with vertical displacement to separate the results for the different phases.

### 3.4.2 Information from pair distribution functions

The partial PDFs $g(r)$ for K–K, K–(C/N) and (C/N)–(C/N) are shown in Fig. 3.6–Fig. 3.8 respectively. For the K–K PDF Fig. 3.6, the high-temperature data show broad peaks at positions consistent with the face-centred cubic arrangement of ions, and in the lower-temperature phases the transition to the orthorhombic phases results in the splitting of these peaks, with the positions being very similar in the two orthorhombic phases but with the expected sharpening of the peaks on cooling through the phase transition from 100 K to 20 K. The peaks up to a distance of around 7 Å in the PDF for the lower-two temperature phase correspond to peaks in the PDF of the high-temperature phase, with the expected broadening, but after 7 Å the peaks positions of the cubic phase are clearly out of register with those in the orthorhombic phases, reflecting the change in symmetry. The first peak in the PDF of the orthorhombic phase is actually comprised of three peaks, at mid-point distances of around 4.2, 4.4 and 4.6 Å. The first peak in the

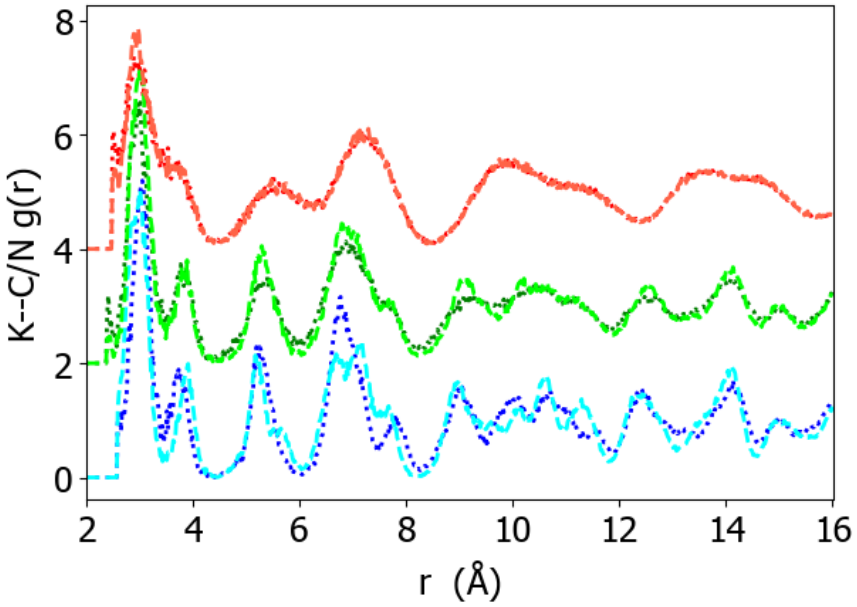


Figure 3.7: K–C (dotted lines) and K–N (dashed lines) partial PDF $g(r)$ for temperatures 20 K (blue), 100 K (green), 200 K (red), with vertical displacement to separate the results for the different phases.

PDF of the cubic phase is centred on position $a/\sqrt{2}$, and it is broad to the extent that it encompasses the distribution of peaks in the low-temperature phases. The second distinct peak in the PDF for the data at 10 K becomes a shoulder in the data for 100 K, and is subsumed within the tail of the first peak in the cubic phase. The fact that the first peak in the PDF of the cubic phase encompasses the distribution of peaks within the low-temperature orthorhombic peaks suggests that there are local distortions of the unit cell that reflect the local orientations of the CN molecular anions. The same can be said of the second peak too,

The K–C and K–N $g(r)$ results ( Fig. 3.7) for 10 K show two peaks at around 3.1 and 3.8 Å, which correspond to two cases in which the K atom lies equidistant from both atoms in the CN molecular anion and where the K..CN and K...NC connections are almost straight lines. It is interesting that the same basic form of this $g(r)$ for the cubic phase too for both the same first pair of peaks and beyond, albeit with expected broadening. Clearly the first peak should be the

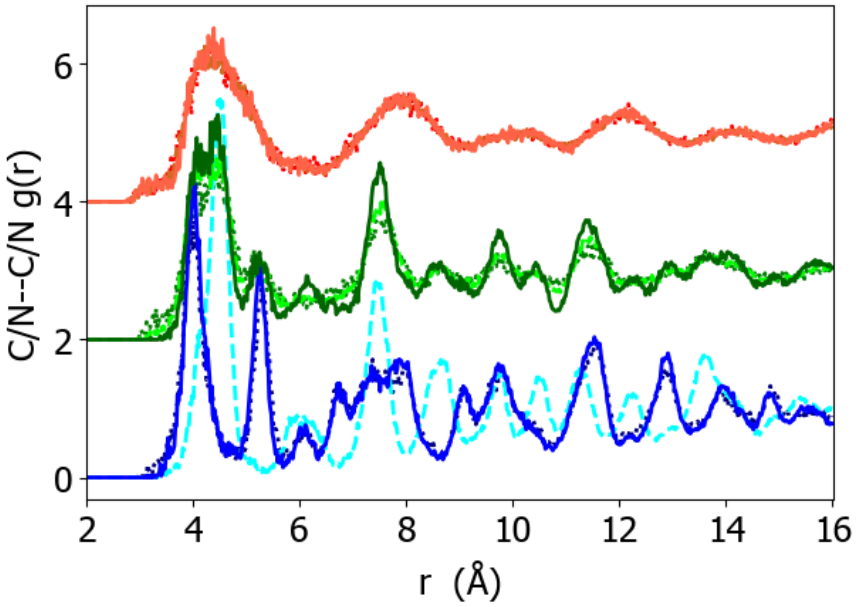


Figure 3.8: C–C (dotted lines), N–N (dashed lines) and C–N (solid lines) partial PDF $g(r)$ for temperatures 20 K (blue), 100 K (green), 200 K (red), with vertical displacement to separate the results for the different phases. For clarity we have excluded the bonded C–N neighbours within the cyanide anion.

same because it is the nearest-neighbour contact between a K atom and either a C or N atom, but it is interesting that the second peak remains into the high-temperature disordered phase, but broadened and with a midpoint shifted to lower distance. The remaining peaks for the cubic phase are consistent with the positions expected for the cation–anion distance in the rocksalt structure with broadening due to the orientational disorder of the cyanide anions. The C–C, C–N and N–N $g(r)$ results are shown in Fig. 3.8. For the cubic phase, there is no difference between C and N, reflecting the orientational disorder, and the $g(r)$ function for both is similar to that for the K–K $g(r)$ ( Fig. 3.6) with broadening of peaks reflecting the orientational disorder. In the low-temperature phase, the C–C and N–N distributions are almost identical, and due to the ordering these are not the same as the C–N distribution.

### 3.4.3 Molecular orientational distribution function

As the simplest type of molecule possible, the rigid unit cyanide molecular anions consist of only two atoms and therefore containing only one chemical bond. The orientation distribution of the cyanide anions is quantitatively described using the bond orientational distribution function $P(\Omega)$, the mathematical details of which were introduced in Section 2.6.1

Table 3.4: Calculated values of the coefficients $c_\ell$ of the cubic harmonic expansion of the bond orientation distribution function $P(\Omega)$ defined in Eq. (2.37). RMC results are compared with values calculated in a molecular dynamics simulation [70].

| Method and $T$ (K) | $c_4$ | $c_6$ | $c_8$ | $c_{10}$ |
|---|---|---|---|---|
| RMC 200 | 0.019(2) | 0.013(2) | 0.024(2) | −0.004(3) |
| RMC 250 | 0.079(2) | −0.003(2) | 0.016(2) | 0.000(2) |
| MD 184 | 0.04 | 0.12 | — | — |
| MD 287 | 0.03 | 0.06 | — | — |

Table 3.5: The values of the coefficients for the $m = 0$ spherical harmonics terms in the bond orientational distribution function for the RMC configurations of the low-temperature $Pmnm$ phase of KCN

| l | 20K | 50K |
|---|---|---|
| 0 | 1.0000(—) | 1.0000(—) |
| 1 | −1.6525(2) | −1.6543(1) |
| 2 | 1.9507(7) | −1.881(2) |
| 3 | −2.039(1) | 1.720(3) |
| 4 | 1.993(2) | −1.545(3) |
| 5 | −1.871(3) | 1.369(4) |
| 6 | 1.716(3) | −1.198(4) |
| 7 | −1.554(3) | 1.038(4) |
| 8 | 1.396(4) | −0.892(3) |
| 9 | −1.248(3) | 0.759(3) |
| 10 | 1.110(3) | 1.9561(5) |
| 11 | −0.981(3) | −2.048(1) |
| 12 | 0.860(2) | 0.2004(2) |

In the low-temperature $Pmnm$ phase of KCN, the cyanide ions occupy sites of $mm2$ point symmetry. The rotator functions $S_i(\Omega)$ are $Y_\ell^{m,\mathrm{c}}(\Omega)$ with even values

Table 3.6: The values of the coefficients for the $m = 0$ spherical harmonics terms in the bond orientational distribution function for the RMC configurations of the intermediate-temperature $Immm$ phase of KCN

| **l** | 100K | 140K |
|---|---|---|
| 0 | 1.0000(—) | 1.0000(—) |
| 2 | 1.7757(3) | 1.8337(4) |
| 4 | 1.4138(6) | 1.553(1) |
| 6 | 0.756(1) | 0.918(2) |
| 8 | 0.236(2) | 0.419(3) |
| 10 | −0.051(2) | 0.165(2) |
| 12 | −0.143(3) | 0.0662(1) |

of $m$. In the intermediate-temperature $Immm$ phase, the point symmetry is $mmm$, and again the rotator function again is a basis of $Y_\ell^{m,c}(\Omega)$ but now requires both $m$ and $\ell$ to be even. Finally, in the high-temperature $Fm\bar{3}m$ phase, the cyanide molecular anions are on sites of $m\bar{3}m$ point symmetry. The rotator functions for this case are the cubic harmonics.

The coefficients in the bond orientational distribution function can be obtained directly by forming the average value of the relevant harmonic from the RMC configurations, in contrast to fitting to data as in diffraction experiments [16]. In this way, it is feasible to compare the calculated distribution function directly with that formed from histograms of bond orientations in the configurations. The form of $P(\Omega)$ for the disordered cubic phase for two arcs of $\Omega$ are shown in Fig. 3.9a and Fig. 3.9b for temperatures 200 K and 250 K respectively. These show the function calculated from the histogram and from the form of $P(\Omega)$ of Eq. (2.37). Values of the coefficients $c_\ell$ were evaluated from averaging over around 100 independent configurations, and are given in Table 3.4, and compared to values obtained from molecular dynamics simulations [70]. All values are small compared with $c_0 = 1$, indicative of a high degree of disorder as seen in Fig. 3.9a and Fig. 3.9b, where the fluctuations from the uniform value $P(\Omega) = 1/4\pi$ do not exceed 10%. There is a very slight preference for ordering along the cubic $\langle 100 \rangle$ directions, and a very

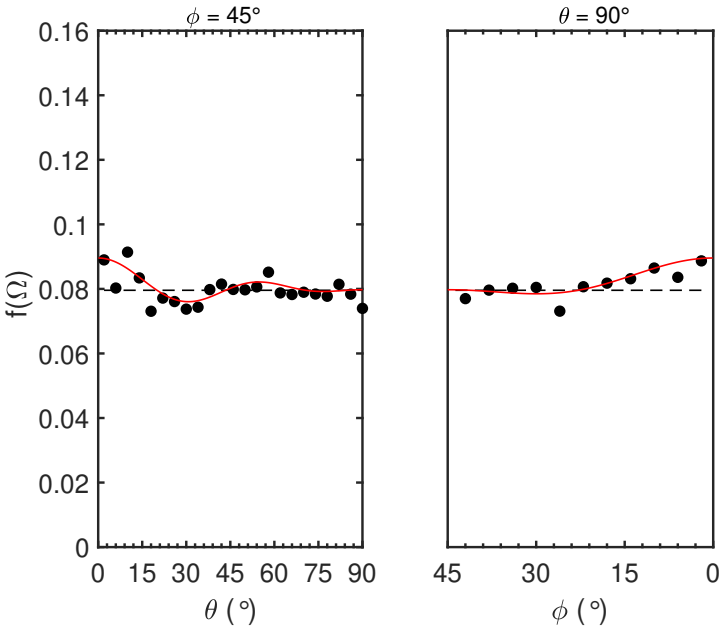


(a) Bond orientation distribution for KCN at 200 K.

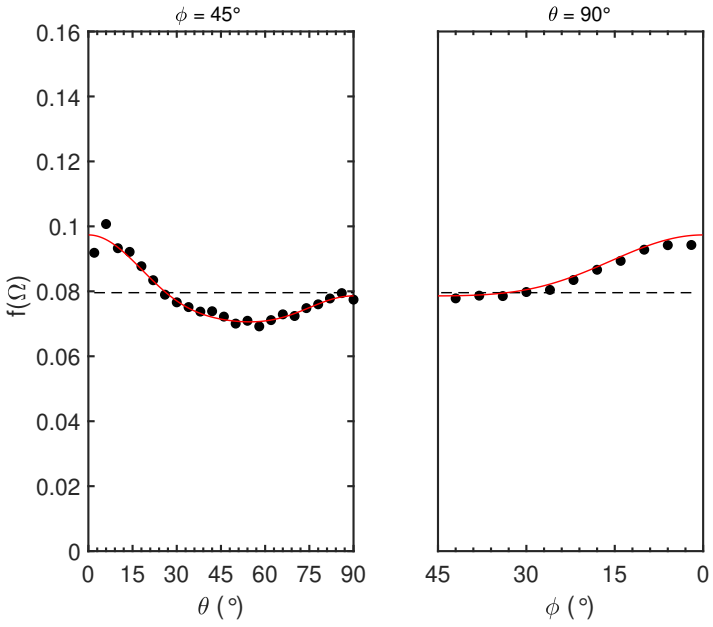


(b) Bond orientation distribution for KCN at 250 K.

Figure 3.9: Bond orientation distribution function for the CN molecular anion in KCN at two temperatures in the disordered cubic phase at two temperatures, a) 200 K and b) 250 K. In both cases the points represent averages from many RMC configurations, and the red lines are calculated from the cubic harmonic expansion with coefficients calculated from the configurations. The left panels show orientations in the directions from $\langle 001 \rangle$ to $\langle 110 \rangle$, and the right panels show the directions from $\langle 110 \rangle$ to $\langle 100 \rangle$. The broken black line at $f(\Omega) = 1/4\pi$ shows the value for a uniform distribution.

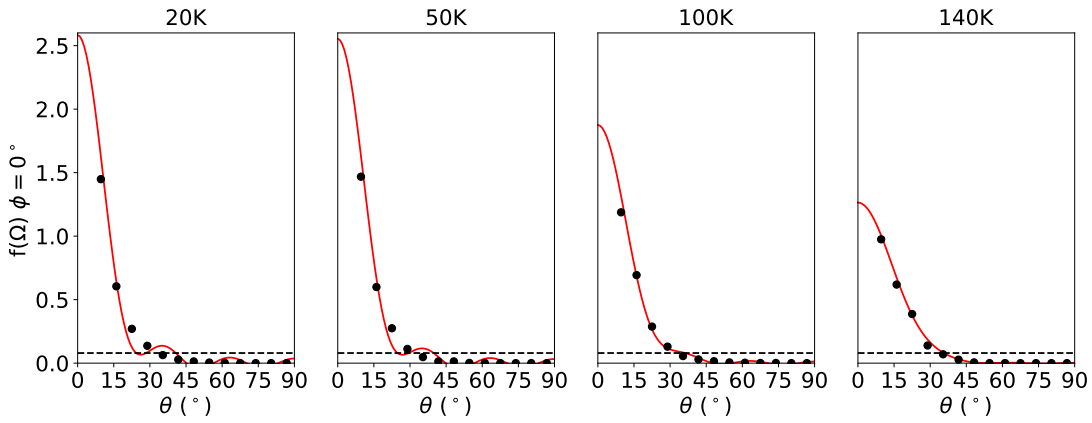


Figure 3.10: A slice view of spherical harmonic expansion and cyanides orientation distribution for KCN at 20 K, 50 K, 100 K and 140 K. Each subplot demonstrates the direction from $\langle 010 \rangle$ to $\langle 001 \rangle$. The black dots represent the orientation distribution directly counted from the RMC output configuration and the red curve represents the orientation distribution function calculated from cubic harmonics. There is a broken black line at $f(\Omega) = 1/4\pi$ indicating the uniformly distributed states.

slight preference away from the $\langle 111 \rangle$ directions, with no obvious preference for the $\langle 110 \rangle$ directions, the directions in which the cyanide molecular anions order in the two lower-temperature orthorhombic phases. The results appear to show a slightly less uniform distribution at 250 K than at 200 K, but the difference is very small and may not be significant. The RMC results for the coefficients $c_\ell$ are similar to those from the simulations [70], particularly in so far as the coefficients for $\ell > 0$ are remarkably small.

The coefficients for the low-temperature $Immm$ phase at 20 K and 50 K, and for the intermediate-temperature $Pmnm$ phase at 100 K and 140 K, are given in Tables 3.5 and 3.6 respectively. The bond orientation functions are shown in Fig. 3.10, showing a much higher degree of orientational order as expected. The degree of orientational order/disorder described by the orientation distribution function of each phases is highlighted by calculating the three-dimensional representations as shown in Fig. 3.11, together with views of representative RMC configurations.

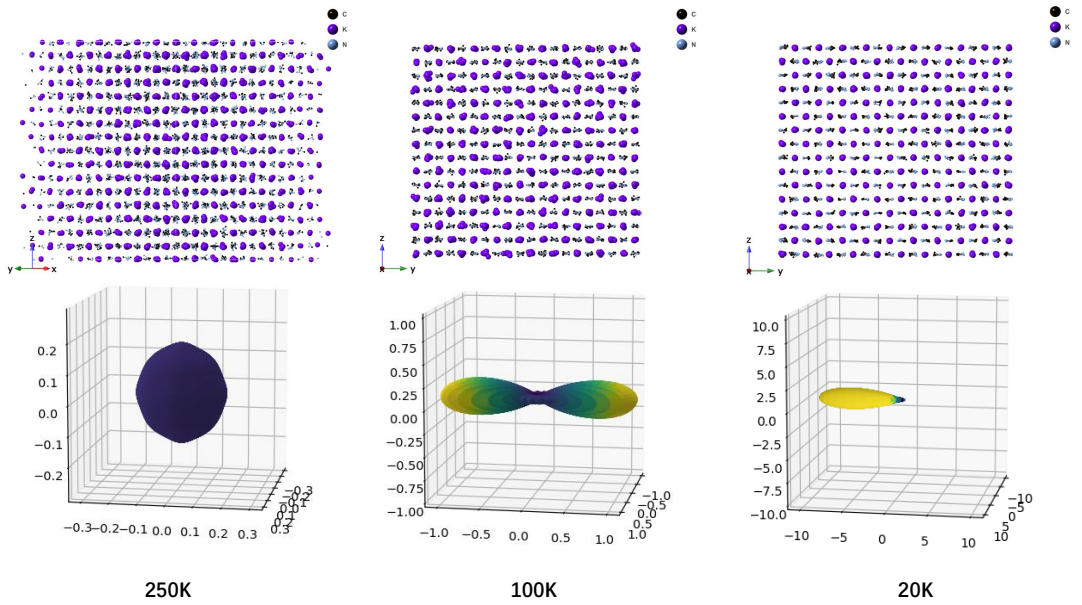


Figure 3.11: RMC configurations showing instantaneous orientations of the cyanide anions (top) for one temperature in each of the three phases (250 K for the high-temperature disordered cubic $Fm\overline{3}m$ phase, 100 K for the intermediate-temperature $Immm$ phase, and 20 K for the low-temperature $Pmnm$ phase). The three-dimensional representations of the bond orientation distribution function in each case calculated from the cubic and spherical harmonics are given in the lower part.The viridis colour map is used for the colour scale scheme. In order to highlight the fact that each crystallographic equivalent cyanide anion is only able to point to one direction, the bond orientation distribution function for the 20 K LT phase is characterized as half of the dumbbell shape.

The picture that emerges from this analysis is that there is almost uniform distribution of orientations of the cyanide anions in the high-temperature cubic phase. The small preference for or against particular orientations is only of order of 10% of the uniform distribution. On the other hand, a much greater degree of quadrupolar ordering (i.e. orientational ordering of the bond ignoring the direction of the dipole moment) in the lower-symmetry phases, and complete ordering on the low-temperature phase. Furthermore, in the low-temperature phase the widths of the distribution function reflect and increase in librational motion on heating from 20 K to 100 K.

## 3.5 Summary

In this chapter, I have used both Bragg scattering analysed by the Rietveld method, and total scattering analysed by the Reverse Monte Carlo method – to study the orientational ordering phase transition in KCN in more detail than was previously possible. The Bragg scattering in this study has primarily given information about the lattice parameters changes with temperatures whereas the total scattering provides the local orientational disorder underlying the lattice parameter change.

The orientational order in each phase of KCN has been evaluated from the atomic configurations generated by the RMC method. At the low temperature, the cyanide anions show quite ordered, with a very narrow C–N bond orientation around the y axis. At the IT phase, the cyanide anions show head-to-tail disorder and larger librational amplitudes. This is confirmed by the RMC configuration and the associated bond orientation calculations. At the HT phase, the calculated C–N bond orientation is almost uniformly distributed, suggesting the large orientational disorder of the cyanide anions in the cubic phase.

Moreover, it has been achieved that good agreement between histograms of the bond orientation distribution function formed from the atomic configurations with an expansion of the bond orientation distribution function in terms of symmetry-adapted orientational functions. With the advantage of large atomic configuration boxes (i.e. large number of cyanide molecular ions), it is able to take the expansion of the distribution function to high order and therefore maintain positive-definiteness, a problem that is encountered when fitting to diffraction data.

# Chapter 4

# Orientational disorder and phase transitions in barium carbonate $BaCO_3$

## 4.1 Introduction

Calcium carbonate, $CaCO_3$, is the most significant of the non-silicate minerals found in the Earth's crust, forming as chalk, limestone and marble, and playing an important role in both the water and carbon dioxide budgets of the planet. Calcite is well-known in the form of Iceland Spar, where the beautiful single crystals with well-defined habit show the dramatic effect of double refraction. The characteristic shape of crystals of Iceland Spar comes from the set of $(10\bar{1}4)$ planes[1] that form the crystal faces, as shown in Fig. 4.1, because these are the electrically neutral planes in the crystal That is, there is no surface dipole moment. Calcite actually has a rather unusual thermal expansion, with a relatively large (for a mineral) positive linear expansivity along the trigonal [001] direction and small but negative

[1]This is the four-index notation for the rhombohedral phases described in the hexagonal/trigonal system.

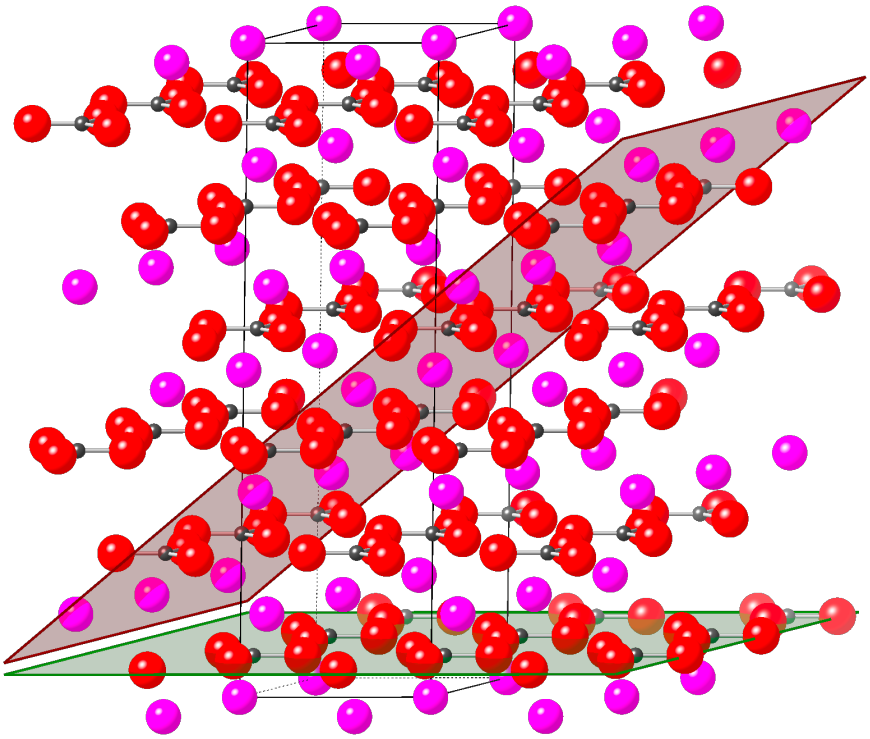

Figure 4.1: Crystal structure of the $R\bar{3}c$ phase of calcite, $CaCO_3$. The $CO_3$ groups (carbon atoms as gray spheres, oxygen atoms as red spheres) lie in planes parallel to the trigonal (0001) plane, separated by layers of calcium atoms (pink spheres). One (0001) plane (translucent green) is shown to highlight the flat layers of carbonate molecular anions. The figure also shows the electrically neutral $(10\bar{1}4)$ planes which form the predominant crystal habit (translucent red).

linear expansivity along the perpendicular directions [78, 79].

The large positive expansivity along the trigonal [001] direction has been associated with a probable orientational order–disorder phase transition at high temperature [80, 81]. The Bragg reflections of the room-temperature phase where the Miller indices $(hki\ell)$ have odd values of $\ell$ fall to zero on heating towards a temperature of around 1260 K [80, 81]. This is consistent with a phase transition from the room temperature structure of space group $R\bar{3}c$ to that of space group $R\bar{3}m$ with a halving of the trigonal $c$ lattice parameter. Such a transition could be achieved if the carbonate groups become orientationally disordered about axes parallel to the trigonal [001] direction. This aspect was studied by neutron powder diffraction [81], showing two interesting unexpected effects. The first was that

on heating the carbonate molecular anions show a large increase in librational amplitude and no growth in the number of anions with a 60° rotation, and secondly a large increase in the amplitude of libration about axes perpendicular to the molecular 3-fold axis. This increase in the perpendicular libration was suggested to explain the rather large thermal expansion of the $c$ axis that appeared to be associated with the phase transition.

Experimentally this was as far as was possible to get to, because the carbonate molecular anions become chemically unstable at the point of the $R\bar{3}c$–$R\bar{3}m$ phase transition, with the rapid decomposition reaction $CaCO_3 \rightarrow CaO + CO_2$. Attempts to prevent this reaction, or at least raise it to a higher temperature, through the use of a pressurised $CO_2$ environment were unsuccessful [81]. This means that the true nature of the $R\bar{3}m$ phase and hence of the phase transition cannot be confirmed, and neither establish a baseline thermal expansion for the $R\bar{3}m$ phase with which to confirm that the origin of the thermal expansion of the $R\bar{3}c$ phase is associated solely with this phase transition.

Subsequent molecular dynamics simulations, suggest that the $R\bar{3}c$–$R\bar{3}m$ phase transition is part of a larger sequence of phase transitions that ultimately reach an orientationally disordered phase with the simple cubic rocksalt structure.

Although it seems impossible to access this state in calcite, it appears that a similar orientationally-disordered rocksalt phase exists in $BaCO_3$ [86]. Actually at ambient conditions $BaCO_3$ is found as the mineral witherite [82–85], which has the aragonite structure adopted by $CaCO_3$, as shown in Fig. 4.2 (orthorhombic symmetry, space group $Pmcn$; details of the crystal structure will be reported below) at a slight high pressure. At a temperature of 1084 K [83] it transforms to a rhombohedral phase of symmetry either $R3m$ or $R\bar{3}m$; the former is ordered with all carbonate anions the same orientation, and the latter is necessarily disordered with respect to the orientations of the carbonate anions. Subsequently at a temperature of 1255 K [83] it transforms to the disordered rocksalt cubic phase [86], until

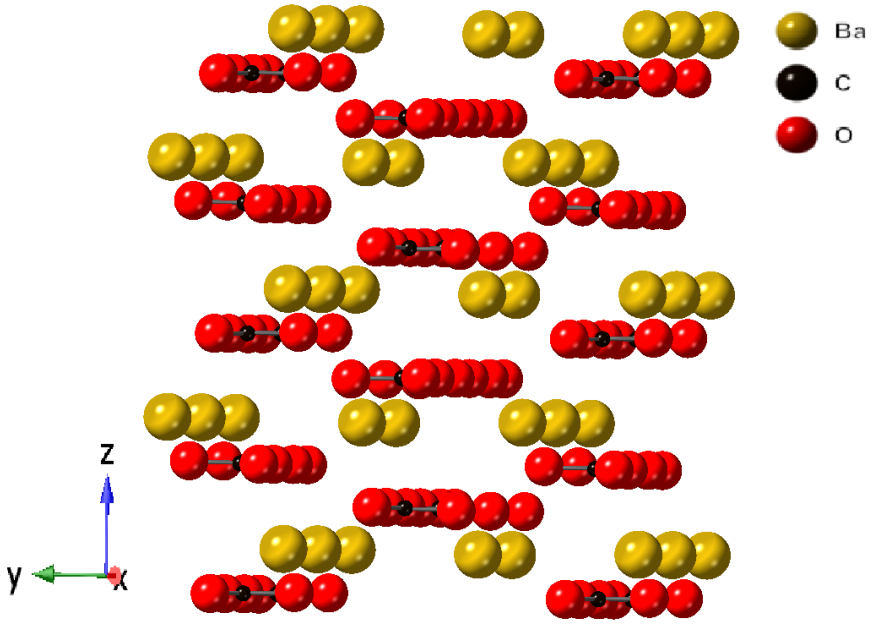


Figure 4.2: Crystal structure of the orthorhombic *Pmcn* phase of witherite, $BaCO_3$ [82–85]. The $CO_3$ groups (carbon atoms as gray spheres, oxygen atoms as red spheres) lie in planes parallel to the orthorhombic (001) plane, separated by layers of barium atoms (gold spheres).

eventually undergoing the decomposition reaction $BaCO_3 \rightarrow BaO + CO_2$.

## 4.2 Experimental and analysis methods

### 4.2.1 Molecular dynamics simulations

Molecular dynamics (MD) simulations were performed using the `DL_POLY` code [55]. The potential energy function of Archer et al [87] was used with rigid $CO_3$ molecules and rigid ions. This was chosen in preference to other alternatives in the literature [88] because it was been specifically tuned to account for the vibrational dynamics of calcite, and in particular to reproduce the soft phonon branch associated with the high-pressure phase transition, whilst retaining full stability, and it was designed to allow for a wide range of divalent cations.

Simulation boxes with orthogonal axes of approximate length 50 Å were prepared using the `data2config`/`rmcreate` program [77]. One axis is along the

trigonal [001] axis, one along the trigonal [100] axis, and the third along the orthogonal [210] axis. MD simulations were also performed using configurations from the witherite crystal structure.

In all cases I used time steps of 0.005 ps. Simulations were equilibrated for 10,000 steps (50 ps) and run for 50,000 steps (250 ps) to generate configurations for analysis. I used constant-stress [89, 90] and constant temperature [91, 92] thermodynamic ensembles.

### 4.2.2 Neutron powder diffraction and total scattering measurements

For the experimental work reported here $BaCO_3$ was obtained commercially. Neutron scattering measurements were performed on the GEM instrument at the ISIS spallation neutron facility [93]. The short runs for the Rietveld refinement were measured for 8 minutes and long runs for the PDF were measured for 6 hours with a proton current of 160 $\mu$A. The first sample dropped after meansuring at 1000 °C, leaving the IT total scattering data unmeasured. In the newly replaced sample, BaO was found at 1000 °C and 930 °C long run, suggesting some $BaCO_3$ had decomposed.

Empty instrument, empty can and empty furnace data are also collected for further data correction. The data were prepared in a form for Rietveld refinement using the MANTID software [94]. The total scattering data were corrected using the GUDRUN code [95].

### 4.2.3 Rietveld analysis

The Rietveld refinements of the different structures of $BaCO_3$ were performed using the GSAS/EXPGUI [96, 97] and GSAS II [98] programs. A representative fit for the ordered witherite phase is shown in Fig. 4.3. Results for lattice parameters

are given in Table 4.1, for atomic fractional coordinates in Table 4.2, and for atomic displacement parameters in Table 4.3 and Table 4.4. The table reports refinements in two different space groups for the intermediate temperature phase. It is found that both space groups model gave equivalent quality fits for data from all neutron banks except the highest-resolution bank of angle 154.40°. As shown in Fig. 4.4, the $R\bar{3}m$ model gives a better fit and correct relative peak heights.Table 4.4 shows the model refined with $R3m$ space group has a large Ba atomic displacement parameter, which is comparable with the C atomic displacement parameter. However, in the witherite phase and the cubic phase, the heavy atom Ba always has a much smaller atomic displacement parameter than the light atom C. Meanwhile, the $R\bar{3}m$ models have atomic displacement parameters more consistent with other phases. Therefore, $R\bar{3}m$ is more likely to be the space group of the intermediate-temperature phase, in spite of the discussion given by Antao and Hassan [83].

Table 4.1: Lattice parameter data for the three phases of $BaCO_3$. These results were obtained by Rietveld refinement of the diffraction data from the GEM diffractometer at ISIS. Horizontal lines demarcate different phases; the top group is for the phase with space group symmetry $Pmcn$, the middle group is for rhombohedral symmetry of either $R\bar{3}m$ or $R3m$, and the bottom line is for cubic space group $Fm\bar{3}m$. Tables 4.2 to 4.4 give the temperatures in the units for the measurement, namely °C, but in the main text I will refer to temperatures in units of K for direct comarison with the molecular dynamics simulations.

| $T$ (°C) | $a$ (Å) | $b$ (Å) | $c$ (Å) | $R_{wp}$ (%) |
|---|---|---|---|---|
| 25 (I) | 5.3305(25) | 8.9288(4) | 6.45167(19) | 4.58 |
| 25 (II) | 5.3282(26) | 8.9250(5) | 6.44887(20) | 5.22 |
| 100 | 5.31743(6) | 8.90467(11) | 6.45480(7) | 5.53 |
| 150 | 5.31915(6) | 8.90636(11) | 6.46966(7) | 5.46 |
| 200 | 5.32087(5) | 8.90804(9) | 6.48472(6) | 4.44 |
| 250 | 5.32259(7) | 8.90963(12 | 6.49905(7) | 5.47 |
| 300 | 5.32424(7) | 8.91161(12) | 6.51668(8) | 5.57 |
| 350 | 5.32694(9) | 8.91577(16) | 6.53620(8) | 5.74 |
| 400 | 5.32873(10) | 8.91751(17) | 6.55370(8) | 6.16 |
| 450 | 5.33042(10) | 8.92006(18) | 6.57253(9) | 6.58 |
| 500 | 5.33176(11) | 8.92226(20) | 6.59073(10) | 7.11 |
| 550 | 5.33360(13) | 8.92580(23) | 6.61110(11) | 8.05 |
| 650 | 5.33955(14) | 8.93600(26) | 6.65945(12) | 7.09 |
| 700 | 5.34124(15) | 8.94086(28) | 6.68444(13) | 7.56 |
| 750 | 5.34276(17) | 8.94649(32) | 6.71179(16) | 8.56 |
| 800 | 5.34375(18) | 8.9535(4) | 6.74229(18) | 9.37 |
| 850 | 5.22387(12) | — | 10.5688(10) | 5.39 |
| 900 | 5.20132(11) | — | 10.65650(26) | 4.99 |
| 950 | 5.16208(11) | — | 10.87436(30) | 4.76 |
| 850 | 5.22399(9) | — | 10.51903(22) | 4.92 |
| 900 | 5.20137(9) | — | 10.65672(21) | 4.90 |
| 950 | 5.16216(10) | — | 10.87424(27) | 4.21 |
| 1000 | 6.9712(2) | — | — | 4.73 |

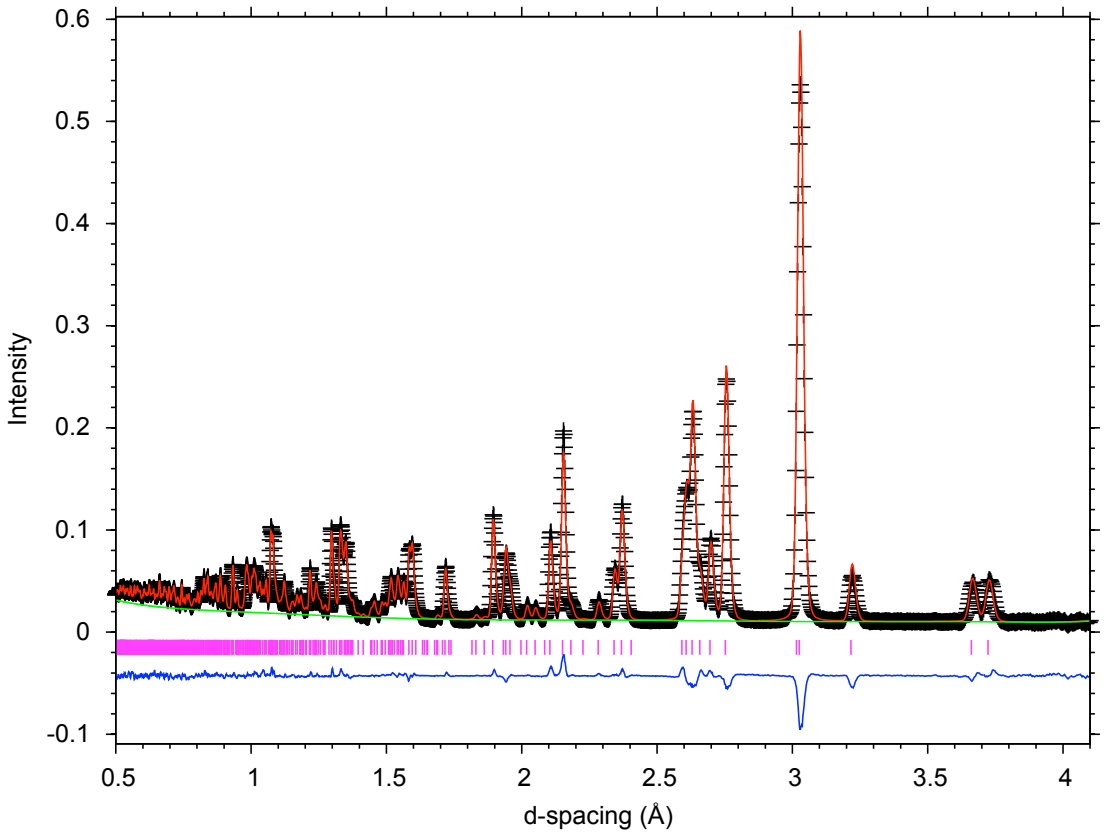


Figure 4.3: A representative fit of diffraction data using Rietveld refinement, shown for the witherite phase at a temperature of 25 °C, with data from the detector bank of nominal scattering angle 63.42°. The black crosses are the data and the red curve is the fitted diffraction profile. The green line indicates the fitted background, and the blue curve represents the difference between data and fitted profile. The magenta vertical lines represent the positions of the Bragg peaks.

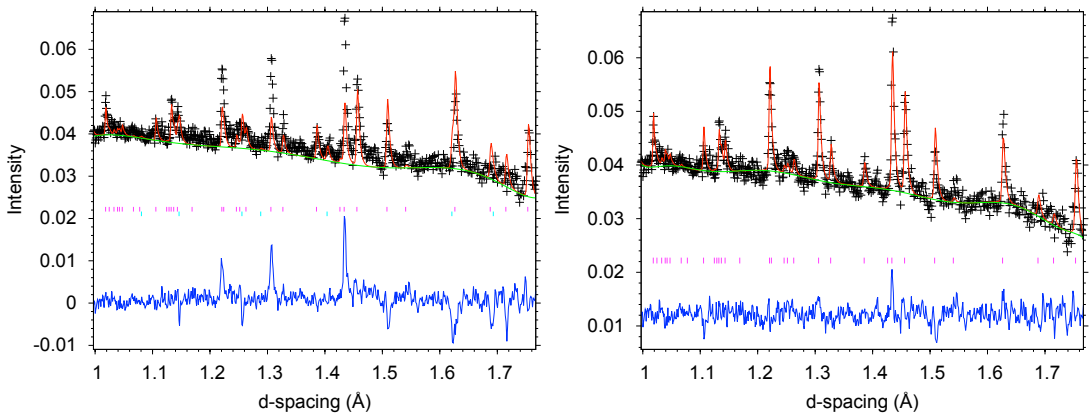


(a) $R3m$ (b) $R\bar{3}m$

Figure 4.4: Comparison of the fits to the highest-resolution diffraction data (detector bank of nominal scattering angle 154.40°) obtained for a temperature of 850 °C from Rietveld refinement, using the crystal structures of the two candidate rhombohedral phases of symmetry $R3m$ and $R\bar{3}m$. The black crosses are the data, the red curves are the fitted diffraction profiles, the green lines indicate the fitted backgrounds, and the blue curves represent the difference between data and fitted profile. The magenta vertical lines represent the positions of the Bragg peaks. A better agreement was obtained with the disordered $R\bar{3}m$ structure.

Table 4.2: Atomic fractional coordinates for the various phases of $BaCO_3$ as indicated in the table. In the space group $Pmcm$ by symmetry $x = 1/4$ for Ba, C and O1. In the $R3m$ phase $x = y = 0$ for Ba and C, and $y = -x$ for O. In the $R\bar{3}m$ phase Ba has $x = y = 0$ and $z = \frac{1}{4}$, C has $x = y = z = 0$ and O has $y = z = 0$. In the cubic $Fm\bar{3}m$ phase Ba has coordinates $(0, 0, \frac{1}{2})$, C has coordinates $(0, 0, 0)$, and O has $x = 0$ and $y = -z$. These results were obtained by Rietveld refinement of the diffraction data from the GEM diffractometer at ISIS.

| *Pmcn* | $T$ (°C) | Ba $y$ | Ba $z$ | C $y$ | C $z$ | O1 $y$ | O1 $z$ | O2 $x$ | O2 $y$ | O2 $z$ |
|---|---|---|---|---|---|---|---|---|---|---|
| | 25 (I) | 0.4164(3) | 0.7538(5) | 0.7567(3) | −0.0810(4) | 0.9015(3) | −0.0894(5) | 0.4598(3) | 0.6831(2) | −0.0806(4) |
| | 25 (II) | 0.4165(4) | 0.7537(5) | 0.7568(3) | −0.0808(4) | 0.9017(3) | −0.0897(6) | 0.4598(3) | 0.6832(2) | −0.0808(4) |
| | 100 | 0.4168(1) | 0.7542(2) | 0.7570(1) | −0.0810(2) | 0.9011(1) | −0.0878(2) | 0.4595(1) | 0.6839(1) | −0.0790(2) |
| | 150 | 0.4166(1) | 0.7543(2) | 0.7570(1) | −0.0810(2) | 0.9011(1) | −0.0878(2) | 0.4594(1) | 0.6839(1) | −0.0790(2) |
| | 200 | 0.4166(1) | 0.7541(2) | 0.7570(1) | −0.0810(1) | 0.9011(1) | −0.0878(2) | 0.4594(1) | 0.6839(1) | −0.0790(1) |
| | 250 | 0.4165(2) | 0.7539(2) | 0.7570(1) | −0.0810(2) | 0.9010(1) | −0.0877(3) | 0.4593(1) | 0.6840(1) | −0.0790(2) |
| | 300 | 0.4167(2) | 0.7540(2) | 0.7570(1) | −0.0810(2) | 0.9010(1) | −0.0877(3) | 0.4593(1) | 0.6840(1) | −0.0790(2) |
| | 350 | 0.4164(2) | 0.7549(2) | 0.7571(1) | −0.0770(2) | 0.9000(2) | −0.0860(3) | 0.4583(2) | 0.6840(1) | −0.0772(2) |
| | 400 | 0.4167(2) | 0.7548(3) | 0.7573(2) | −0.0765(2) | 0.8998(2) | −0.0850(3) | 0.4589(2) | 0.6844(1) | −0.0767(2) |
| | 450 | 0.4160(2) | 0.7560(3) | 0.7571(2) | −0.0748(3) | 0.8999(2) | −0.0839(3) | 0.4590(2) | 0.6853(1) | −0.0759(2) |
| | 500 | 0.4161(2) | 0.7560(3) | 0.7568(2) | −0.0740(3) | 0.9004(2) | −0.0841(4) | 0.4589(2) | 0.6858(1) | −0.0751(2) |
| | 550 | 0.4163(3) | 0.7561(3) | 0.7575(3) | −0.0722(3) | 0.9003(3) | −0.0843(4) | 0.4587(2) | 0.6867(2) | −0.0738(3) |
| | 650 | 0.4166(3) | 0.7569(4) | 0.7579(3) | −0.0710(4) | 0.8994(3) | −0.0837(4) | 0.4555(3) | 0.6858(2) | −0.0732(3) |
| | 700 | 0.4164(3) | 0.7581(4) | 0.7575(3) | −0.0694(4) | 0.8998(4) | −0.0810(5) | 0.4554(3) | 0.6868(2) | −0.0731(3) |
| | 750 | 0.4157(4) | 0.7572(4) | 0.7583(3) | −0.0682(5) | 0.9010(4) | −0.0795(5) | 0.4548(4) | 0.6881(2) | −0.0717(4) |
| | 800 | 0.4173(4) | 0.7637(4) | 0.7573(4) | −0.0601(6) | 0.8970(4) | −0.0816(6) | 0.4555(4) | 0.6881(3) | −0.0718(4) |
| *R3m* | $T$ (°C) | Ba $z$ | C $z$ | O $x$ | O $z$ | | | | | |
| | 850 | 0.1257(6) | 0.6012(6) | 0.136(4) | 0.6012(6) | | | | | |
| | 900 | 0.0840(9) | 0.5664(7) | 0.140(5) | 0.5664(7) | | | | | |
| | 950 | 0.0795(8) | 0.5681(9) | 0.1124(3) | 0.5637(9) | | | | | |
| $R\bar{3}m$ | $T$ (°C) | O $x$ | | | | | | | | |
| | 850 | 0.2106(7) | | | | | | | | |
| | 900 | 0.2109(8) | | | | | | | | |
| | 950 | 0.2055(10) | | | | | | | | |
| $Fm\bar{3}m$ | $T$ (°C) | O $z$ | | | | | | | | |
| | 1000 | 0.1132(4) | | | | | | | | |

Table 4.3: Atomic displacement parameters for the witherite phase of $BaCO_3$. These results were obtained by Rietveld refinement of the diffraction data from the GEM diffractometer at ISIS.

| $T$ (°C) | Ba $U_{iso}$ | C $U_{iso}$ | O $U_{11}$ | O $U_{12}$ | O $U_{13}$ | O $U_{22}$ | O $U_{23}$ | O $U_{33}$ |
|---|---|---|---|---|---|---|---|---|
| 25 (I) | 0.00425(17) | 0.00720(16) | 0.0035(4) | — | — | 0.0021(4) | -0.0036(5) | 0.0296(6) |
| | | | 0.00163(25) | 0.00210(24 ) | -0.00314(34) | 0.00414(26) | 0.0040(4) | 0.0329(4) |
| 25 (II) | 0.00404(19) | 0.00729(17) | 0.0031(5) | — | — | 0.0023(4) | -0.0032(5) | 0.0290(7) |
| | | | 0.00146(27) | 0.00178(26) | -0.0034(4) | 0.00387(29) | 0.0044(4) | 0.0334(5) |
| 100 | 0.00547(22) | 0.00906(20) | 0.0069(6) | — | — | 0.0030(5) | -0.0035(6) | 0.0349(8) |
| | | | 0.00238(33) | 0.00282(31) | -0.0039(4) | 0.00642(35) | 0.0048(5) | 0.0423(6) |
| 150 | 0.00654(24) | 0.01060(22) | 0.0078(7) | — | — | 0.0039(5) | -0.0019(7) | 0.0386(9) |
| | | | 0.00303(35) | 0.00248(33) | -0.0030(5) | 0.0080(4) | 0.0063(6) | 0.0473(6) |
| 200 | 0.0076(7) | 0.0115(6) | 0.0098(6) | — | — | 0.0050(5) | -0.0025(6) | 0.0432(8) |
| | | | 0.00389(31) | 0.00348(29) | -0.0037(4) | 0.00946(33) | 0.0053(5) | 0.0514(6) |
| 250 | 0.00855(27) | 0.01281(24) | 0.0120(8) | — | — | 0.0061(6) | -0.0016(8) | 0.0474(10) |
| | | | 0.0046(4) | 0.0040(4) | -0.0045(5) | 0.0112(4) | 0.0046(6) | 0.0573(7) |
| 300 | 0.01007(29) | 0.01430(26) | 0.0157(9) | — | — | 0.0073(7) | -0.0039(8) | 0.0512(11) |
| | | | 0.0051(5) | 0.0039(4) | -0.0043(6) | 0.0140(5) | 0.0057(7) | 0.0634(8) |
| 350 | 0.00965(31) | 0.01802(31) | 0.0126(13) | — | — | 0.0104(9) | 0.0006(11) | 0.0660(14) |
| | | | 0.0071(7) | 0.0016(5) | -0.0035(8) | 0.0134(6) | 0.0048(8) | 0.0665(10) |
| 400 | 0.00923(34) | 0.01704(32) | 0.0172(14) | — | — | 0.0117(10) | -0.0001(12) | 0.0657(15) |
| | | | 0.0057(7) | 0.0022(6) | -0.0041(8) | 0.0136(6) | 0.0031(9) | 0.0702(10) |
| 450 | 0.00822(34) | 0.01747(35) | 0.0200(15) | — | — | 0.0132(10) | 0.0036(13) | 0.0699(16) |
| | | | 0.0070(8) | 0.0037(6) | -0.0017(9) | 0.0134(7) | -0.0003(10) | 0.0743(11) |
| 500 | 0.00646(34) | 0.0167(4) | 0.0209(15) | — | — | 0.0155(12) | 0.0060(14) | 0.0733(17) |
| | | | 0.0060(8) | 0.0045(6) | -0.0014(10) | 0.0157(7) | -0.0044(11) | 0.0795(12) |
| 550 | 0.0061(4) | 0.0172(4) | 0.0225(17) | — | — | 0.0136(13) | 0.0127(16) | 0.0763(20) |
| | | | 0.0069(9) | 0.0059(7) | 0.0015(11) | 0.0158(8) | -0.0078(12) | 0.0838(14) |
| 650 | 0.0125(6) | 0.0310(6) | 0.0121(20) | — | — | 0.0271(17) | 0.0062(22) | 0.0985(25) |
| | | | 0.0208(13) | -0.0035(10) | 0.0021(14) | 0.0213(12) | -0.0013(15) | 0.0910(17) |
| 700 | 0.0100(6) | 0.0331(7) | 0.0115(20) | — | — | 0.0311(19) | 0.0074(25) | 0.1105(28) |
| | | | 0.0190(13) | -0.0021(11) | 0.0071(14) | 0.0251(13) | -0.0030(16) | 0.0953(19) |
| 750 | 0.0073(7) | 0.0318(8) | 0.0130(23) | — | — | 0.0341(21) | 0.0123(29) | 0.1136(33) |
| | | | 0.0195(14) | 0.0006(12) | 0.0118(16) | 0.0249(14) | -0.0053(18) | 0.1060(22) |
| 800 | 0.0026(7) | 0.0467(11) | -0.0026(22) | — | — | 0.0473(28) | 0.0722(31) | 0.135(4) |
| | | | 0.0243(16) | 0.0036(14) | 0.0147(18) | 0.0197(16) | -0.0127(19) | 0.0936(24) |

Table 4.4: Atomic displacement parameters for the IT and HT phases of $BaCO_3$. These results were obtained by Rietveld refinement of the diffraction data from the GEM diffractometer at ISIS. Horizontal lines demarcate different phases; the top group is for the phase with space group symmetry $R3m$, the middle group is for $R\bar{3}m$ and the bottom line is for cubic space group $Fm\bar{3}m$.

| $T$ (°C) | Ba $U_{\mathrm{iso}}$ | C $U_{\mathrm{iso}}$ | O $U_{11}$ | O $U_{12}$ | O $U_{13}$ | O $U_{22}$ | O $U_{23}$ | O $U_{33}$ |
|---|---|---|---|---|---|---|---|---|
| $R3m$ | | | | | | | | |
| 850 | 0.0652(24) | 0.0610(18) | 0.1484(23) | 0.0976(27) | -0.0380(13) | 0.1484(23) | 0.0380(13) | 0.237(4) |
| 900 | 0.0764(22) | 0.0815(23) | 0.1481(20) | 0.0930(26) | -0.0390(12) | 0.1481(20) | 0.0390(12) | 0.253(4) |
| 950 | 0.0963(24) | 0.1032(27) | 0.1581(23) | 0.0920(31) | -0.0436(14) | 0.1581(23) | 0.0436(14) | 0.322(6) |
| $R\bar{3}m$ | | | | | | | | |
| 850 | 0.0564(13) | 0.0976(18) | 0.1190(26) | 0.163(6) | 0.1021(27) | 0.331(11) | 0.238(5) | 0.3476(34) |
| 900 | 0.0579(13) | 0.1238(23) | 0.1232(30) | 0.145(7) | 0.0934(32) | 0.295(13) | 0.221(6) | 0.3507(34) |
| 950 | 0.0693(16) | 0.155(4) | 0.152(4) | 0.166(6) | 0.1014(32) | 0.336(13) | 0.237(6) | 0.401(4) |
| $Fm\bar{3}m$ | | | | | | | | |
| 1000 | 0.089(5) | 0.210(12) | 0.411(31) | — | — | 0.206(14) | -0.020(10) | 0.206(14) |

### 4.2.4 Reverse Monte Carlo method

The Reverse Monte Carlo method was performed using the `RMCprofile` code [51]. For most of the work I used v6.7, but for the intermediate temperature phase I used a completely new version in prototype form, provisionally assigned version number 7, which is being designed for simulation of more than a single phase [2]. Because of decomposition at high temperature, our first experimental measurements were performed at high temperature, but the first sample is lost due to a malfunction within the furnace. In fact this sample had survived intact on heating into the high-temperature cubic phase with no decomposition is detected. The data for the intermediate-temperature phase were obtained on a second sample. Unfortunately, in this case the onset of decomposition, with clear Bragg peaks associated with the presence of BaO. The strategy for the RMC analysis of the intermediate-temperature phase was to use two configurations, alternatively moving one atom at random in each configuration. The relative weights of each phase to the total scattering, PDF [99] and Bragg scattering were determined by the phase fraction determined by the prior Rietveld analysis.

As for the MD simulations, starting configurations of the $BaCO_3$ phases, with orthogonal axes of approximate length 50 Å, were prepared using the `data2config`/`rmcreate` program [77], using the structures generated by the Rietveld refinement analysis at each temperature and lattice parameters constrained to these values. Minimum distances and interatomic potentials for the C–O bond and O–C–O angles were applied as constraints in the RMC simulations. Taking the RMC simulation of the cubic phase as the example, the minimum allowed distances for the C–C, C–O, C–Ba, O–O, O–Ba and Ba–Ba contacts were 3.8, 1.0, 2.6, 1.93, 2.25 and 3.8 Å respectively. The C–O bond potential was a Morse

[2]This version has not previously been described in the scientific literature, and a paper will be published in due course. Key developers have been Christopher Kerr (University of Cambridge), Wojciech Sławiński (STFC), and the three authors AEP, MGT and MTD.

function with 1.29 Å as the equilibrium distance and 3.5 eV as the difference in energy between the lowest energy and the energy at infinite distance. The O–C–O angle potential was set with 120° as the equilibrium angle and 5.0 eV as the corresponding force constant. Each RMC simulation was run until the average number of successful moves for every atom in the $BaCO_3$ phase was nearly 200, with a maximum single move distance of 0.05 Å.

The BaO configurations used with the multiphase analysis of the intermediate-temperature phase were prepared in the same way and were of similar sizes. BaO has the standard rocksalt structure, space group $Fm\bar{3}m$.

The quality of the RMC fits to data are shown for the example of the witherite phase at room temperature (at this temperature the sample is single phase) in Fig. 4.5. Similar quality was obtained for all temperatures, including the two-phase RMC.

## 4.3 Phase transitions seen in the molecular dynamics simulations

### 4.3.1 Simulations starting in the calcite structure

The temperature-dependence of the lattice parameters of both $CaCO_3$ and $BaCO_3$, obtained by MD simulation and starting in the ordered calcite form, are shown in Fig. 4.6. The simulation box gives two orthogonal evaluations of the trigonal $a$ lattice parameter. To highlight the transition to the cubic phase, the lattice parameters are scaled as $a' = \sqrt{2}a$ and $c' = c/2\sqrt{3}$ to give the values corresponding to those of the cubic phase $a$ lattice parameter. In both cases the transitions to the cubic form is very clear – at temperatures of $1665 \pm 10$ K and $2535 \pm 10$ K for $BaCO_3$ and $CaCO_3$ respectively – as also are the transitions between the low-temperature ordered phases to the disordered $R\bar{3}m$ phases at temperatures

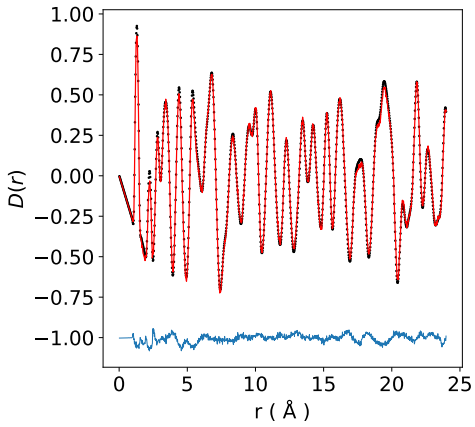


(a) $D(r)$

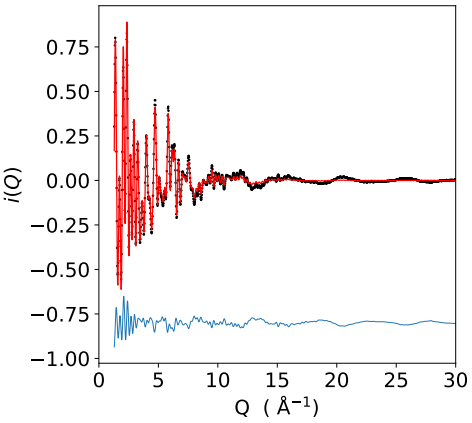


(b) $i(Q)$

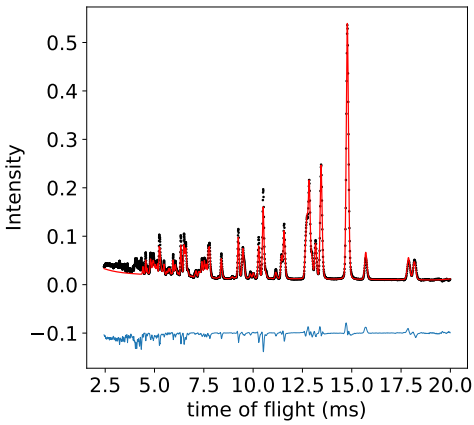


(c) Bragg scattering

Figure 4.5: Representative RMC fits of (a) pair distribution function, (b) total scattering function, and (c) Bragg pattern, for witherite at room temperature. In each case the black points represent the experimental data, and the red lines represent the RMC fitted functions. The blue lines represent the difference between the experimental and RMC fitted functions.

of $905 \pm 10$ K and $1985 \pm 10$ K for $BaCO_3$ and $CaCO_3$ respectively. It is noted that the simulations over-estimate the $R\bar{3}c$–$R\bar{3}m$ transition temperature in calcite by about 60%, and the transition to the cubic phase of $BaCO_3$ is over-estimated by around 30%. However, transition temperatures are very hard to predict from models derived from equilibrium properties only. What is encouraging is that the transition temperatures in $BaCO_3$ are lower than in $CaCO_3$, as expected. What is interesting, however, is that the background thermal expansion around

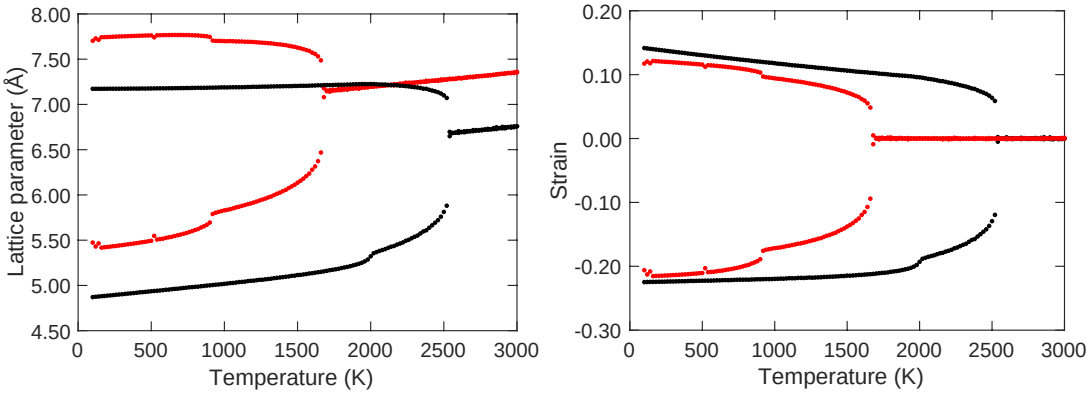


Figure 4.6: Left: Temperature-dependence of the lattice parameters of $CaCO_3$ (black) and $BaCO_3$ (red) in the calcite form as determined by molecular dynamics simulations. In each case the top curve represents $\sqrt{2}a$ and the lower curve is $c/\sqrt{12}$, the quantities that become the cubic $a$ lattice parameter at high temperature. Right, the corresponding strains obtained by subtracting the extrapolation of the cubic lattice parameter to low tempertures.

the $R\bar{3}c$–$R\bar{3}m$ transition in both cases is mostly associated with the approach to the transition to the cubic form, and not, as previously assumed [80, 81], due to the ordering associated with the $R\bar{3}c$–$R\bar{3}m$ transition. Fig. 4.6 also shows the strains calculated by comparing the lattice parameters with the extrapolation from the cubic phase, It can be seen that these are extraordinarily large for a phase transition, reaching over 20%.

Configurations from the MD simulation of each phase are shown in Fig. 4.7. The barium and calcium atoms are not shown in these figures in order to make the orientational behaviour of carbonate groups prominent. At low temperature, the carbonate anions in both $BaCO_3$ and $CaCO_3$ are orientationally ordered, although it is clear that the carbonate groups in $BaCO_3$ have spontaneously reoriented to give an ordered structure that is different from both calcite and witherite. As the temperature increases on heating towards the intermediate-temperature phase, the carbonate anions in both cases show growing librational motions about the molecular 3-fold rotational axis and about the orthogonal axes, whilst maintaining the same average orientations. The MD configuration shown in Fig. 4.7b suggests the space group for the intermediate-temperature phase of $BaCO_3$ is $R\bar{3}m$. In

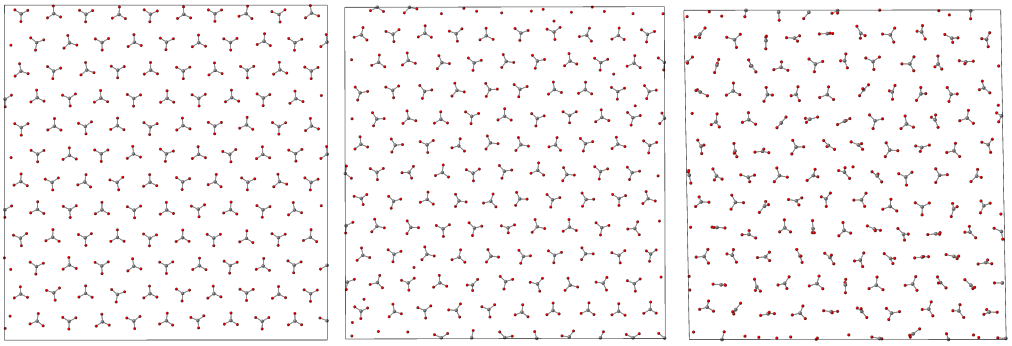

(a) $BaCO_3$, 300 K (b) $BaCO_3$, 1000 K (c) $BaCO_3$, 1700 K

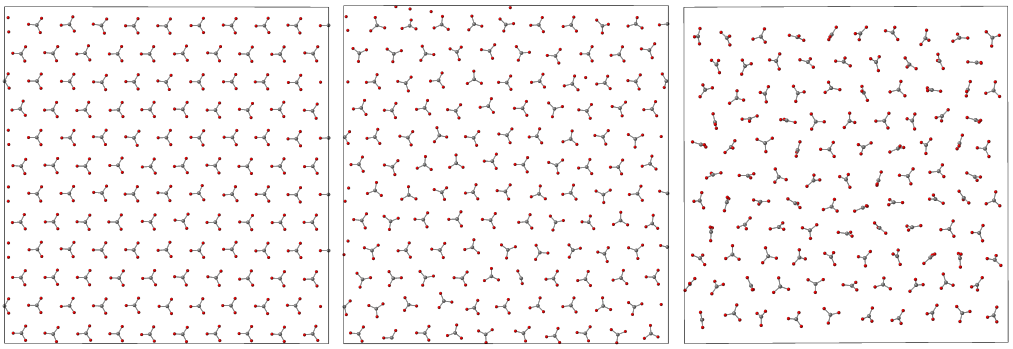

(d) $CaCO_3$, 300 K (e) $CaCO_3$, 2000 K (f) $CaCO_3$, 2600 K

Figure 4.7: Representative configurations from the MD simulations of $BaCO_3$ (top row) and $CaCO_3$ (bottom row) viewing from the trigonal [001] direction. the alkali metal atoms are excluded from these figures for clarity.

Figs. 4.7c and 4.7f, there are no orientation pattern for carbonate ions, indicating they lose preferred orientations in the cubic phases.

The orientational disorder of the carbonate groups can be seen in the distribution of C–O bond orientations. Fig. 4.8 shows how the distribution of C–O bonds in the MD simulations of $CaCO_3$ evolves with increasing temperature. The distribution broadens on heating and it vanishes in the intermediate temperature phase as shown in Fig. 4.8f. This indicates the C–O bonds in $CaCO_3$ have a preferred orientation along [100] in the low temperature phase. The C–O bonds become more widely spread around [100] with increasing temperature. At intermediate temperatures, the orientational distribution becomes nearly uniform around the equator line with large spread of librations out of this plane.

A similar trend exists in $BaCO_3$, albeit with different orientations of the

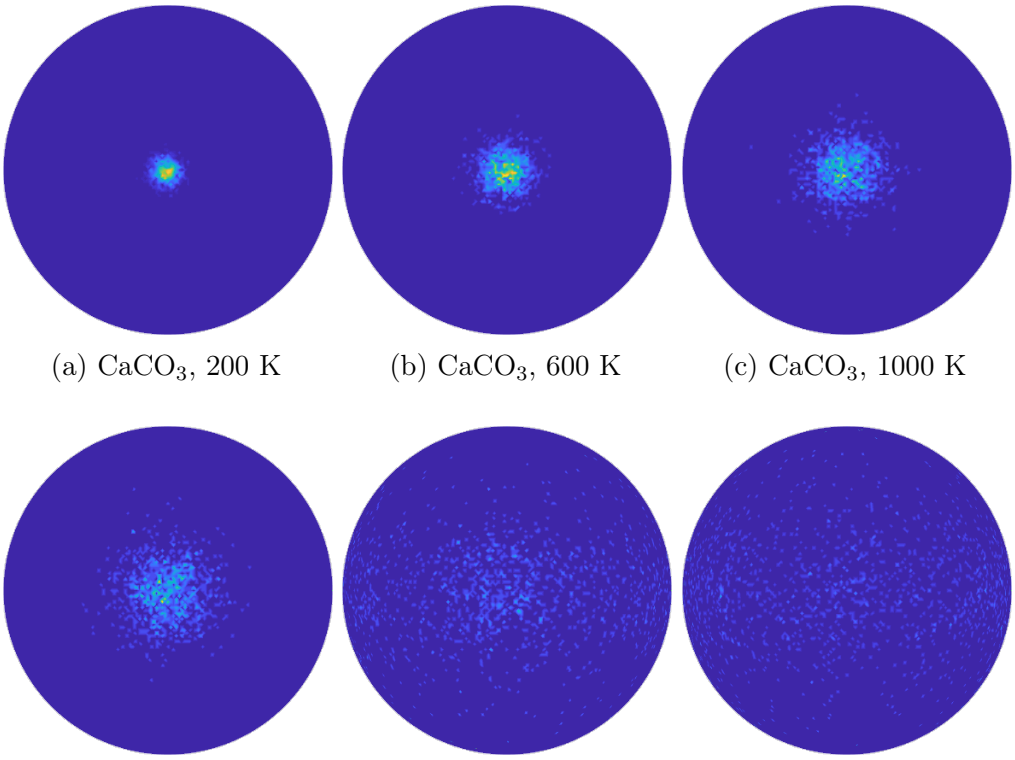

(a) $CaCO_3$, 200 K (b) $CaCO_3$, 600 K (c) $CaCO_3$, 1000 K

(d) $CaCO_3$, 1400 K (e) $CaCO_3$, 2000 K (f) $CaCO_3$, 2200 K

Figure 4.8: Orthographic projections of the C–O bond orientation distributions for $CaCO_3$ at different temperatures from MD simulations, viewed along the [100] direction. Yellow represents orientations of high probability, whereas while dark blue represents orientations with low probability.

carbonate molecular ion as noted above, and for which the C–O bond orientation distribution is shown in Fig. 4.9. At 200 K, there are 2 preferred orientations i.e. two concentrated bright dots at the equator lie viewing from the [100] direction. As the temperature increases to 1000 K, shown in Fig. 4.9a to Fig. 4.9d, the C–O orientation becomes more widely spread while the two preferred orientations are still distinguishable (brighter than other solid angles). At the intermediate-temperature phase, as shown in Figs. 4.9e and 4.9f, the C–O orientation become more evenly spread around the equator and more progressively spread towards the poles.

The C–O bond orientation distribution plots from molecular dynamics simulations suggest that in both $CaCO_3$ and $BaCO_3$ the carbonate ions are orientationally

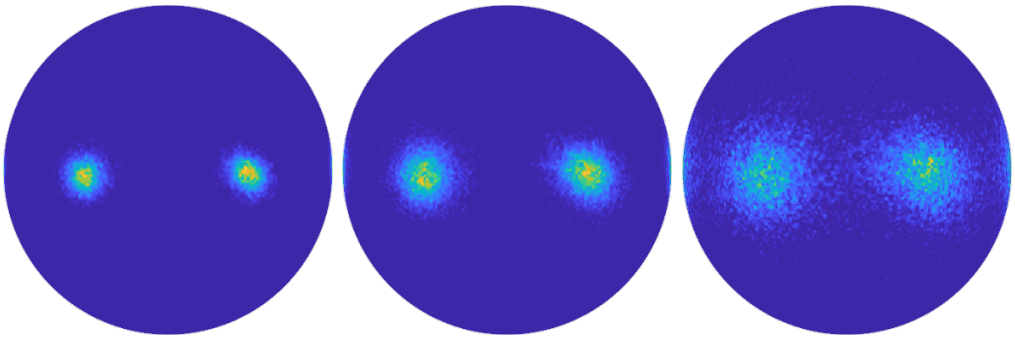

(a) $BaCO_3$, 200 K (b) $BaCO_3$, 400 K (c) $BaCO_3$, 800 K

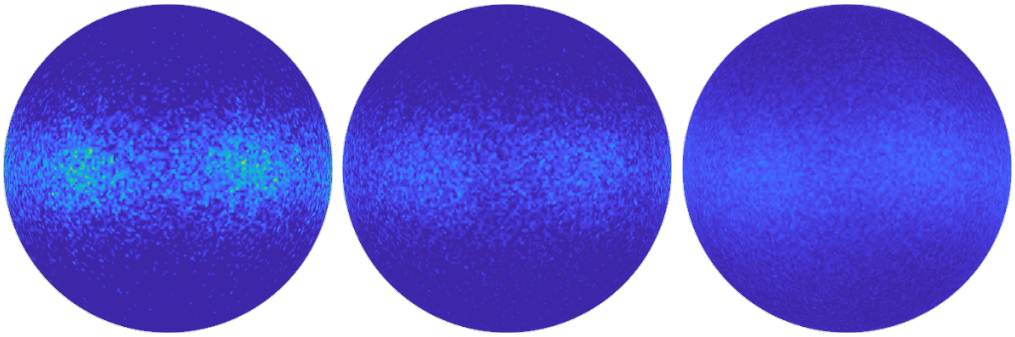

(d) $BaCO_3$, 1000 K (e) $BaCO_3$, 1200 K (f) $BaCO_3$, 1600 K

Figure 4.9: Orthographic projections of the C–O bond orientation distributions for $BaCO_3$ at different temperatures from MD simulations, viewed along the [100] direction. The colour scheme is described in the caption to Fig. 4.8.

ordered at the low temperature phases. Their rotational and librational vibration amplitudes increase with increasing temperatures resulting in a larger spread of C–O bond orientation distribution. In the intermediate-temperature phase, full disorder with respect to rotation about the threefold axis is achieved and libration out of the molecular plane increases, before the orientations of the carbonate ions become fully disordered at the cubic phase.

### 4.3.2 Simulations starting in the witherite structure

MD simulations of $BaCO_3$ are also performed with the witherite phase as the starting configuration . Over the time scale of the simulations the structure will retain the basic layout of the sites for the Ba and C atoms, but will allow

reorientations of the $CO_3$ groups as seen in the simulations of $BaCO_3$ starting in the calcite structure.

The simulated lattice parameters are shown in Fig. 4.10 and compared with the experimental values derived from Table 4.1. Fig. 4.10 makes use of the fact that the atomic structure of the witherite (aragonite) phase has the Ba atoms in an approximate hexagonal close-packed arrangement, with the C atoms in the corresponding octahedral sites to give a structure that is derived from the ideal type structure of NiAs (Strukturbericht type $B8_1$). On this basis, the $a$ lattice parameter of the orthorhombic phase will correspond to that of the hexagonal phase, and the $b$ lattice parameter, representing an orthogonal direction will correspond to a distance equal to $\sqrt{3}$ times the hexagonal $a$ lattice parameter. The $c$ lattice parameter reflects the spacing between the close-packed layers in the hexagonal close-packed arrangement, and will have ideal value when $c = \sqrt{8/3}a$. Thus Fig. 4.10 plots $a$, $b/\sqrt{3}$ and $c/\sqrt{8/3}$. The hexagonal symmetry is broken by the ordering of the orientations of the carbonate groups, but on heating in the simulation we see a clear phase transition to a hexagonal structure as the carbonate groups develop disorder first with orientations about the molecular 3-fold axis and then as full three-dimensional disorder.

The experimental lattice parameters for the witherite phase, shown in Fig. 4.10, follow the simulated values up to the point of the transition to the rhombohedral phase. What is interesting from Fig. 4.10 is the close correspondence between the simulated and experimental lattice parameters. The experimental coefficients of the thermal expansion at higher temperatures in the witherite phase are $\alpha_a = 5 \times 10^{-6}$ K$^{-1}$, $\alpha_b = 13 \times 10^{-6}$ K$^{-1}$, and $\alpha_c = 82 \times 10^{-6}$ K$^{-1}$. The relatively large experimental value of $\alpha_c$ can therefore be understood in terms of the onset of three-dimensional disorder, and the smaller temperature variation of the $a$ and $b$ lattice parameters can be understood in terms of the convergence of these quantities in the simulated transition to a hexagonal phase.

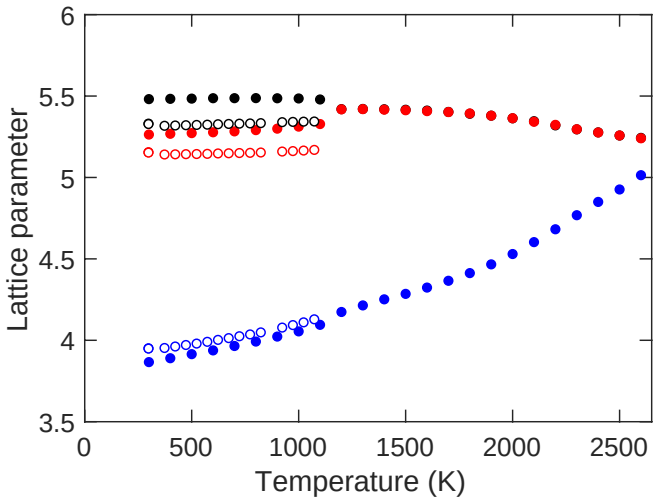


Figure 4.10: Temperature-dependence of the lattice parameters of $BaCO_3$ in the orthorhombic witherite form obtained by MD simulation (filled circles) and from Rietveld refinement of the neutron powder diffraction data (open circles). The black points are $a$, red points are $b/\sqrt{3}$, and blue points are $c/\sqrt{8/3}$. The scaling is explained in the text, and is chosen so that the scaled $a$ and $b$ lattice parameters will come together in value with a phase transition from the orthorhombic to disordered hexagonal structure, and the scaled $c$ lattice parameter will become closer in value as the disordered hexagonal phase approaches the ideal close-packed structure.

## 4.4 Results from the Reverse Monte Carlo analysis of $BaCO_3$

### 4.4.1 Atomic structures

Fig. 4.11 show representative layers of the configurations from the RMC analysis, which in the cases of the witherite phase and the intermediate rhombohedral phase are viewed down the directions perpendicular to the alignment of the molecular 3-fold axes in the crystal structures. In comparison with Fig. 4.7 it is noted there are bond-bending distortions of the carbonate molecular ions here that are not seen in the MD configurations. This is because the carbonate ions are held rigidly fixed in shape in the MD simulations but are clearly allowed to distort in reality and as seen in the RMC simulations.

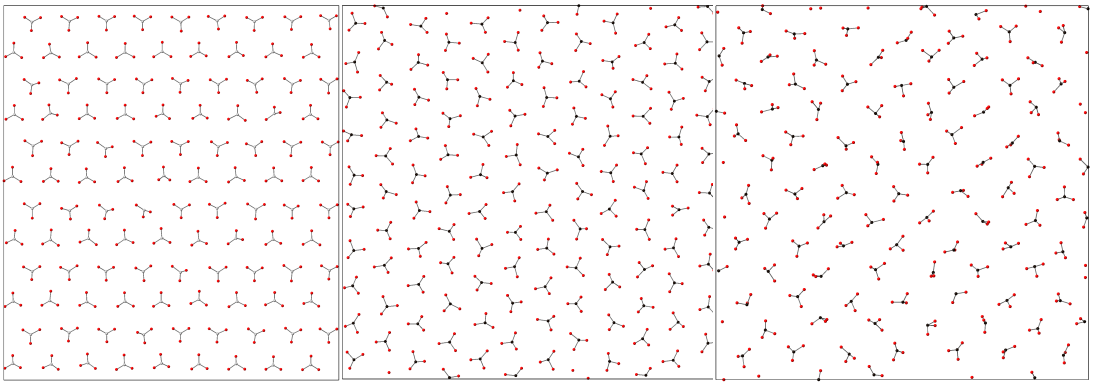

(a) $BaCO_3$, 300 K (b) $BaCO_3$, 1203 K (c) $BaCO_3$, 1273 K

Figure 4.11: Representative carbonate atomic layers from the RMC configurations of $BaCO_3$ viewing from the crystallographic [001] directions in each case. Ba atoms are excluded from these figures for clarity.

### 4.4.2 Witherite phase

Fig. 4.12a shows the distribution of C–O bond orientations within the RMC configurations for the witherite phase, and the corresponding distribution from the MD simulations is shown in Fig. 4.12b. The distributions for the RMC models for the two rhombohedral-phase starting points are shown in Figs. 4.12c and 4.12d. As compared with the MD (Fig. 4.9), the distribution shows more motion of the bonds corresponding to rotations about axes perpendicular to the carbonate three-fold rotation axis. This is consistent with the extraordinary large values of the atomic displacement parameter $U_{33}$ values given in Table 4.3, and is fully consistent with the phase behaviour discussed earlier as revealed by the MD simulations.

### 4.4.3 Rhombohedral phase

Although in the previous discussion on the Rietveld analysis it is remarked that we the rhombohedral phase is more likely to have the disordered $R\bar{3}m$ structure than that with space group $R3m$, we explored using both the $R\bar{3}m$ and $R3m$ structures as the starting configurations for the RMC analysis of this phase. In fact we found that both give similar quality fits to the three sets of data, and the

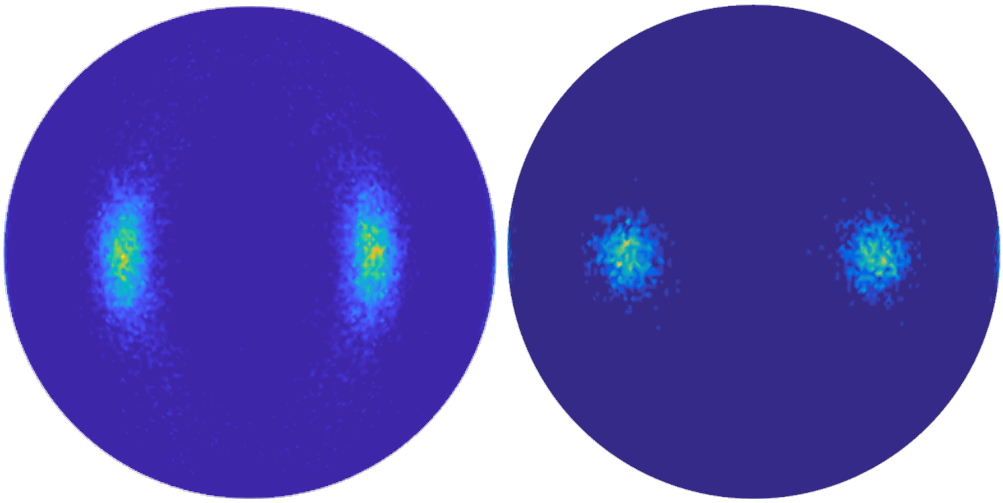

(a) Witherite RMC at 300 K



(b) Witherite MD at 300 K

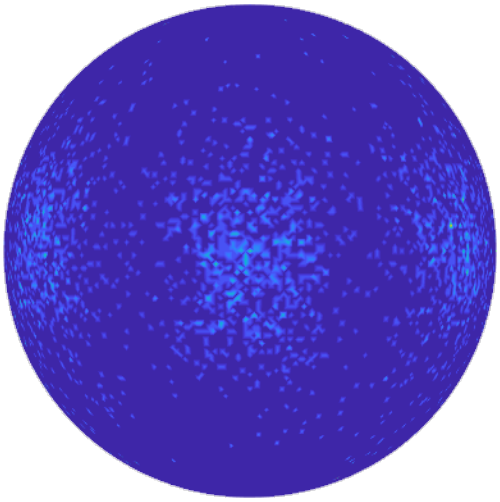

(c) $R\bar{3}m$ RMC at 1203 K

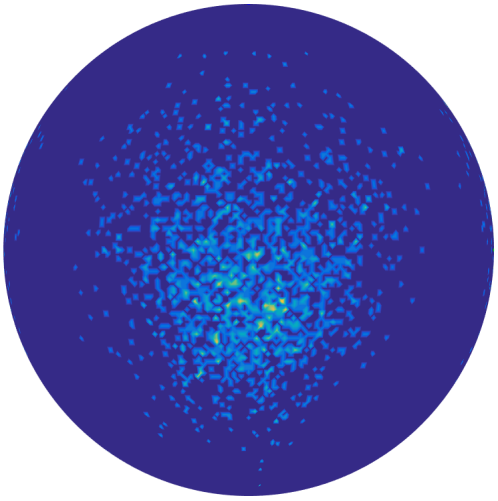

(d) $R3m$ RMC at 1203 K

Figure 4.12: Orthographic projections of the C–O bond orientation distributions for $BaCO_3$ in the witherite phase at 300 °C from the RMC and MD simulations, and for the rhombohedral phases with space groups $R\bar{3}m$ and $R3m$ at 930 °C, each viewed along the [100] direction. The colour scheme is described in the caption to Fig. 4.8.

structures remained the same throughout the RMC simulation. Thus RMC is not giving us a preference for one structure over the other.

Fig. 4.12c shows the C–O bond orientation distribution for the $R\bar{3}m$ phase, and that for the $R3m$ phase is shown in Fig. 4.12d. Similar to the RMC and MD results shown in Figs. 4.12a and 4.12b for the room-temperature witherite phase, the

vertical libration is more prominent than the horizontal rotation movement. This is consistent with the atomic displacements parameters obtained from Rietveld refinement as show in Tables 4.3 and 4.4; although the values of $U_{11}$ and $U_{22}$ increase dramatically in the rhombohedral phase, they remain smaller than the value of $U_{33}$.

### 4.4.4 Cubic phase

The various partial pair distribution functions $g(r)$ from both RMC and MD configurations for cubic $BaCO_3$ are shown in Fig. 4.13. The overall match is good, albeit with a very slight difference in length scale. The $g(r)$ functions for the Ba–Ba, Ba–C and C–C pairs reflect the simple rocksalt structure. The more interesting functions are those involving the oxygen atoms, because these will reflect the degree of disorder, and here the agreement between MD and RMC is considered to be good. Small differences will be a reflection of some small differences in bond orientational distribution function described next.

In the cubic phase of $BaCO_3$, and theoretically of $CaCO_3$ also, the carbonate groups (molecular point group symmetry $3/m$) occupy sites of the full octahedral symmetry (point group $m\bar{3}m$). The lower symmetry of the molecular anion implies that there must be orientational disorder. Such cases of orientationally disordered crystals are common; examples are KCN described in the previous chapter, and $CBr_4$ and $SF_6$ [16]. Again, the orientations distribution of the rigid unit C - O bonds $P(\Omega)$s for cubic $BaCO_3$ and $CaCO_3$ are calculated by a symmetry adapted functions. The $P(\Omega)$s are calculated from both the MD configurations and the RMC configurations. Values of $c_\ell$ for the distribution of C–O bonds are given in Table 4.5.

Fig. 4.14 shows the C–O bond orientational distribution function for cubic $BaCO_3$ calculated from the RMC configurations. It displays both the bond distri-

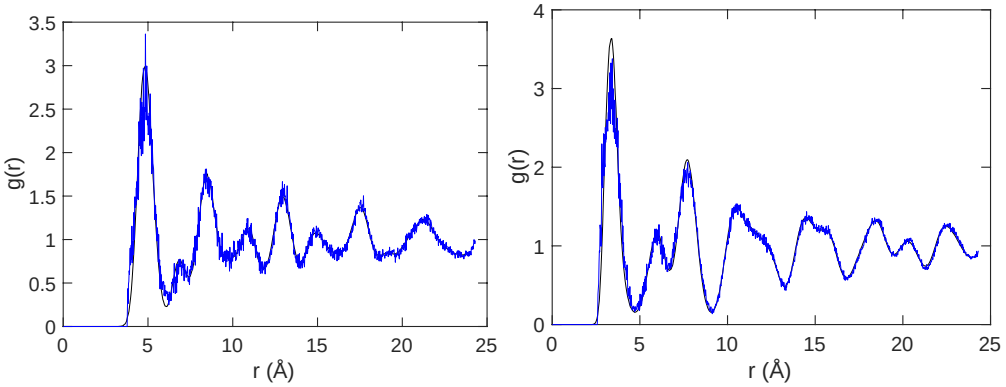


(a) Ba–Ba




(b) Ba–C

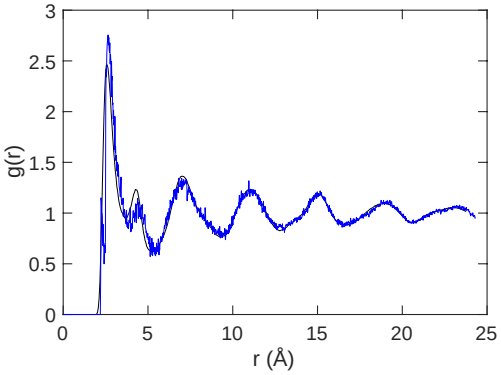


(c) Ba–O

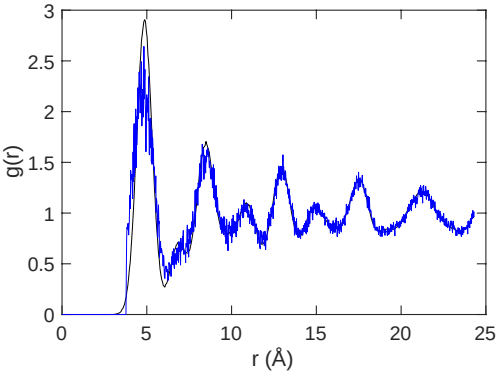


(d) C–C

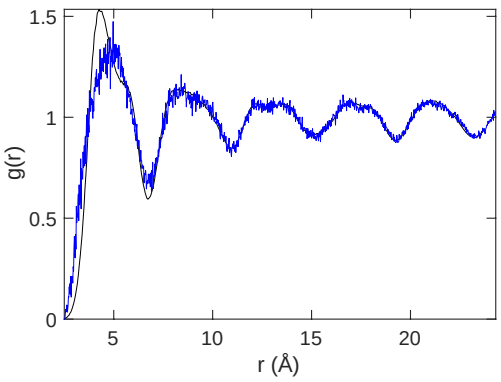


(e) C–O

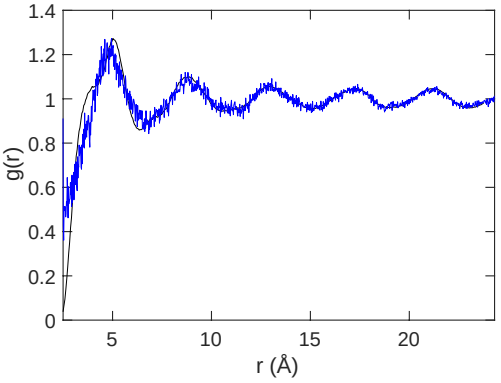


(f) O–O

Figure 4.13: Partial pair distribution functions $g_{mn}(r)$ for cubic $BaCO_3$ from RMC (blue lines) and MD (black curves) for each of the atomic pairs. Note that we do not include the low-$r$ part for the C–O and O–O functions because the peaks in the MD simulations are $\delta$-functions since we used rigid carbonate molecular anions. Due to the simulation transition temperature being higher than experiment, the PDFs for experiment are at 1273 K and for the simulation at 2600 K. A small rescaling of the values of $r$ for the MD data was applied to bring the peaks into best registry, accounting for imperfections in the interatomic potentials and the effects of thermal expansion.

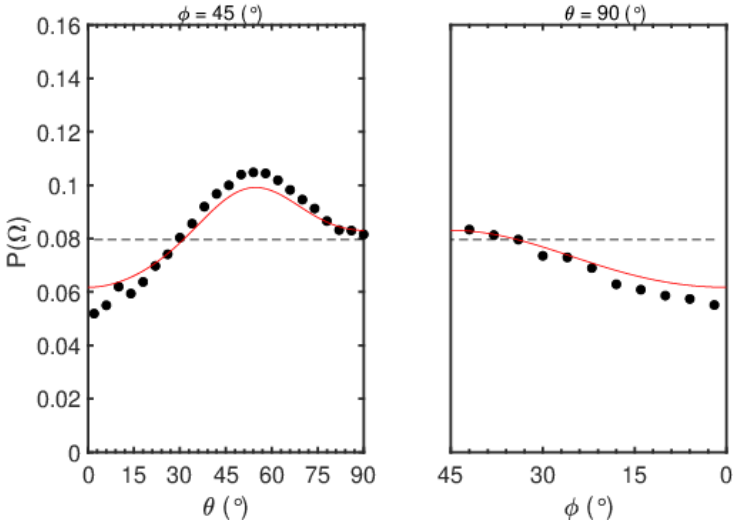


Figure 4.14: C–O bond orientational distribution function for cubic $BaCO_3$ from RMC. The points are histograms of the actual distribution in the RMC configurations, and the red line is calculated from the cubic harmonic functions, Eq. (2.37). The horizontal dashed line at $P = 1/4\pi$ is the value for a uniform distribution.

Table 4.5: Values of the coefficients $c_\ell$ in the expansion of the C–O bond orientational distribution function $P(\Omega)$ as defined by Eq. (2.37). These values were obtained by averaging over several atomic configurations as described in the text. Note that $c_0 = 1$.

| | $T$ (K) | $c_4$ | $c_6$ | $c_8$ | $c_{10}$ |
|---|---|---|---|---|---|
| $BaCO_3$ RMC | 1203 | −0.117 | 0.019 | 0.010 | −0.005 |
| $BaCO_3$ MD | 1660 | 0.1745 | −0.042 | 0.057 | −0.006 |
| $BaCO_3$ MD | 3000 | 0.028 | −0.009 | −0.004 | 0.007 |
| $CaCO_3$ MD | 2520 | 0.171 | −0.013 | 0.031 | 0.004 |
| $CaCO_3$ MD | 3000 | 0.0497 | −0.028 | −0.016 | −0.005 |

bution function calculated point-by-point from the histogram of bond angles, and as calculated from Eq. (2.37). The value $P(\Omega) = 1/4\pi$ corresponds to a uniform distribution function. It is seen that there is some preference for alignment away from the ⟨100⟩ directions, but only of the order of just over 10% variation away from the uniform distribution.

Fig. 4.15 shows the C–O bond orientational distribution functions for cubic $BaCO_3$ and $CaCO_3$ calculated from the MD configurations. These distributions are more uniform than in the RMC configurations, but the phase transitions are

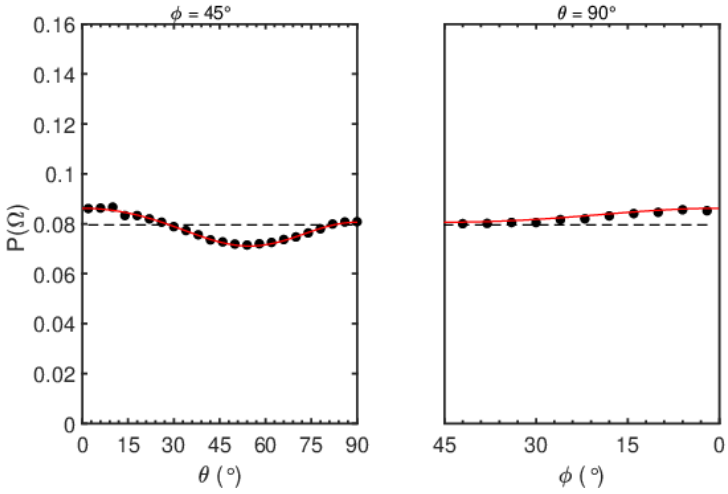


(a) $CaCO_3$

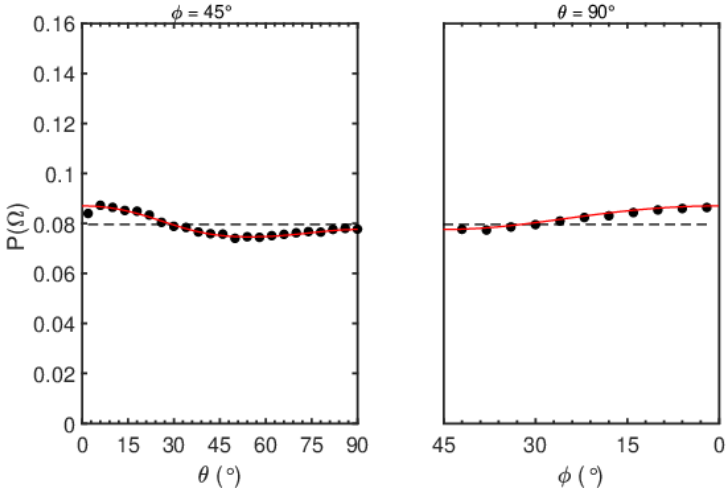


(b) $BaCO_3$

Figure 4.15: C–O bond orientational distribution function for cubic $BaCO_3$ and $CaCO_3$ from MD simulations. The points are histograms of the actual distribution in the RMC configurations, and the red line is calculated from the cubic harmonic functions, Eq. (2.37). The horizontal dashed line at $P = 1/4\pi$ is the value for a uniform distribution.

at higher temperatures and so these distributions represent correspondingly higher temperatures. In fact the distributions become more uniform on heating, since over the temperature range 1500–3000 K the value of the coefficient $c_4$ for cubic $BaCO_3$ falls by about one half. The distributions in the MD simulations of both $BaCO_3$ and $CaCO_3$ differ from the RMC in that they show slight preferences for orientations along the $\langle 100 \rangle$ directions rather than away from these directions, but the effects are actually very slight.

## 4.5 Summary

The key objective of this study was to identify the orientational disorder in the cubic phase of $BaCO_3$, which has been shown by both RMC and MD to be almost completely uniform. Given the shape of the $CO_3$ molecular anion, it is not surprising that this might be so. The lower-temperature MD data and earlier crystallographic data on $CaCO_3$ show that although the C–O bond has a preference to point along symmetry directions in the hexagonal basal plane, it has a large growth in out-of-plane orientations on heating.

The existence of the cubic phase of $BaCO_3$ that is reflected also in the MD simulations of both systems leads to a new interpretation of the observed phase transition in $CaCO_3$. Previously it was assumed that the main phase transition was from space groups $R\bar{3}c$ to $R\bar{3}m$ on heating, with the onset of orientational disorder about the 3-fold axis leading to halving of the crystallographic repeat distance parallel to the 3-fold axis. The onset of decomposition at the phase transition meant that it was impossible to confirm the existence of the higher-symmetry phase, but loss of certain Bragg peaks on heating to the transition are only consistent with this explanation. What was previously unexplained was the fact that on heating towards the phase transition the largest orientational fluctuations were associated with tilting of the 3-fold axis away from the plane

normal rather than about this axis. This is seen also in the MD simulations of the $R\bar{3}c$ in calcite, Fig. 4.8. Furthermore, without data on the lattice parameters for temperatures above the phase transition it was hard to analyse the strains associated with ordering. What emerges from the MD results presented here is that the variation of the lattice parameters with temperature is affected primarily by the spontaneous strains associated with the transition to the cubic phase and not between the two rhombohedral phases. This is a completely new viewpoint on the phase behaviour of the important mineral calcite.

# Chapter 5

# Atomic structure of the continuous random network of amorphous PAF-1

## 5.1 Introduction

Topology-guided design is playing an increasingly important role in structural chemistry and condensed matter physics. The diamond topology, an infinite connected tetrahedral network, is one of the most favoured three-dimensional topologies in nature [100]. Crystalline materials with the diamond network include, in addition to the diamond form of carbon and the foundational semiconductor material silicon, the $\beta$-cristobalite form of silica [101, 102], and the negative thermal expansion materials zinc cyanide [103], $Cu_2O$ [104, 105] and silicon dicarbodiimide [106].

As demonstrated most clearly by silica and many aluminosilicates, and the zeolitic imidazolate frameworks (ZIFs) [107], there are many networks consisting of connected tetrahedral sites. Not only is there a very large number of crystalline tetrahedral networks, but it is known that they can also form as amorphous

phases with what are described as 'continuous random networks' (CRN) [108–111]. Amorphous silicon [111–113] and silica [114, 115] are two obvious examples, but other examples include a wide range of other amorphous aluminosilicates [116] and amorphous ZIF [117]. Sometimes the amorphous phase not only provides isotropy and increased processability, but also provides some surprising properties such as lower volume change when metal ions are inserted, which leads to improved cycle performance as anodes in batteries [118]. In this chapter I focus on a recently-discovered new amorphous material, carbon di-4,4′-biphenyl, which has been designated as a 'porous amorphous framework' with the name PAF-1 [119, 120].

The thriving field of reticular chemistry provides many options for framework materials with high porosity. Various MOFs (metal-organic frameworks) [121, 122], COFs (covalent-organic frameworks) [123, 124] or POFs (porous organic frameworks) [125, 126] have been synthesised with a range of pore sizes and structures. These structures show great potential for use in gas adsorption [120, 127], separation [128] and catalyst carriers [129]. Yet between the exciting aspiration of the research laboratories and the realisation of industrial applications lie the issues of physical and chemical stability, giving what are often the major challenges for their commercial applications [130].

Attempts to synthesize a structure with diamond topology consisting of $4,4'$-biphenyl molecular linkages inserted between tetrahedral carbon nodes were inspired by the high stability of diamond itself. The result was the amorphous material PAF-1 [119], with chemical formula $C([C_6H_4]_2)_2$. It was found that PAF-1 has an ultra-high surface area (BET surface area 5600 $m^2g^{-1}$) with uniform pore width, and excellent physicochemical stability [131]. X-ray powder diffraction measurements from PAF-1 indicated the framework is not crystalline but amorphous [119], and it has been suggested that the amorphous structure could be an example of a tetrahedral CRN [132, 133].

Trewin et al. [133–135] investigated a large number of atomic models – mostly

crystalline – as potential candidates for the atomic structure for PAF-1. Their approach was to calculated the internal surface area and pore volume for each, and found that the best match was a structure based on amorphous silica. Thus, to date, this is the best candidate atomic structure of PAF-1, albeit based not on diffraction data but only on measurements and calculations of porosity.

This paper aims at answering the question of the atomic structure of PAF-1 through a combination of neutron total scattering with hydrogen-deuterium substitutions to give different views of the carbon and hydrogen atoms, and molecular dynamics simulations. The evidence from these two approaches is fully consistent with the atomic structure of PAF-1 being that of a CRN with tetrahedral C sites connected by the biphenyl molecules. That is, the structure is directly analogous to those of amorphous silicon, silica and zinc imidazolate. This is consistent with the previous suggestion [132] as supported from porosity measurements [134], but is now confirmed directly by diffraction measurements and characterised through the MD simulations.

## 5.2 Experimental details

### 5.2.1 Sample synthesis

The samples of PAF used in this study were synthesised by collaborators in China, through a nickel(0)-catalysed Yamamoto-type Ullmann coupling reaction with terkis(4-bromophenyl)methane (TBM) as the monomer. Three samples were prepared: one fully deuterated (D-PAF-1) prepared with deuterated monomer (D-TBM), one fully hydrogenated (H-PAF-1) prepared with hydrogenous monomer (H-TBM), and one with a mixture of hydrogen and deuterium with relative proportions such that the sum of the scattering lengths from the two isotopes is as close to zero as synthesis accuracy allows (H/D-PAF-1). Specifically, H/D-PAF-1

was prepared with mixture of H-TBM and D-TBM (molar ratio of 1.7834:1) as monomer. In this case, only the carbon atoms will be visible as coherent scattering in the total scattering experiments. The use of three samples gives a contrast in the total scattering experiments that models of the atomic structure must reproduce.

### 5.2.2 Basic material characterisation

The efficiency of the polymerisation can be determined by the C–Br bond vibration peak in FT-IR spectrum. (Figs. .1 to .4 in appendix) The C–Br bond vibration in the monomer is characterised by the peak at 532cm$^{-1}$ for H-TBM and 455cm$^{-1}$ for D-TBM respectively. This peak almost disappears completely in the FT-IR spectrum of H-PAF-1 and becomes very weak in the FT-IR spectrum of both D-PAF-1 and H/D-PAF-1. confirming the high efficiency of polymerisation. The relatively low polymerisation efficiency is contributed to the low activity of reaction substrate. The powder X-ray diffraction confirms the lack of long range order for all PAF-1s. Low pressure $N_2$ sorption measurement proves all PAF-1s show high $N_2$ uptake and typically microporous characterisation. Calculated BET surface area for H-PAF-1, D-PAF-1 and H/D-PAF-1 are 5309.4, 4364.5 and 4365.5 m$^2$g$^{-1}$, respectively. The average pore sizes of H-PAF-1, D-PAF-1 and H/D-PAF-1 are 1.2, 1.2 and 1.3 nm , respectively.

### 5.2.3 Neutron scattering experiments

#### Total scattering experiments at ISIS

Neutron total scattering experiments were performed on the NIMROD diffractometer [136] at the ISIS spallation neutron source. NIMROD is designed to perform measurements of total scattering in the forward scattering direction,

thereby minimising the effects of inelastic scattering in data corrections associated with light atoms.

The samples were loaded into thin-walled vanadium cans of diameter 4 mm, which were mounted within a closed-cycle refrigerator (CCR). Measurements were performed at temperatures of 10, 150 and 300 K, counting for 6 hours of beam time with a proton current of 44 $\mu$A.

In addition to the measurements on the samples, additional measurements were performed of the empty instrument, the empty CCR, and the empty sample can inside the CCR for data correction, and of a vanadium rod for normalisation. The data were processed and corrected using the GUDRUN tool [95]. Useful data were obtained for a range of values of scattering vector $Q$ between 0.02–35 Å$^{-1}$.

#### Small angle scattering experiments at CSNS

Further experiments to obtain measurements of the small angle scattering down to lower values of $Q$ region were performed on the Small Angle Neutron Scattering (SANS) instrument at China Spallation Neutron Source (CSNS) [137]. The sample was mounted in a standard rectangular sample container made of thin silica glass. The incident neutron beam had wavelength ranged of 1–10 Å defined by a double-disc bandwidth chopper, and was collimated to the sample by a pair of apertures. Each measurement took two hours. Data were corrected for background scattering, sources of beam attenuation, and detector efficiencies.

### 5.2.4 Building the random network

The starting point of building the model was a CRN of points with tetrahedral coordination, established using the WWW method [138] starting from a random arrangement [111]. The task of decorating this arrangement of points was tackled using software written by Prof. Martin Dove. The network was expanded to give

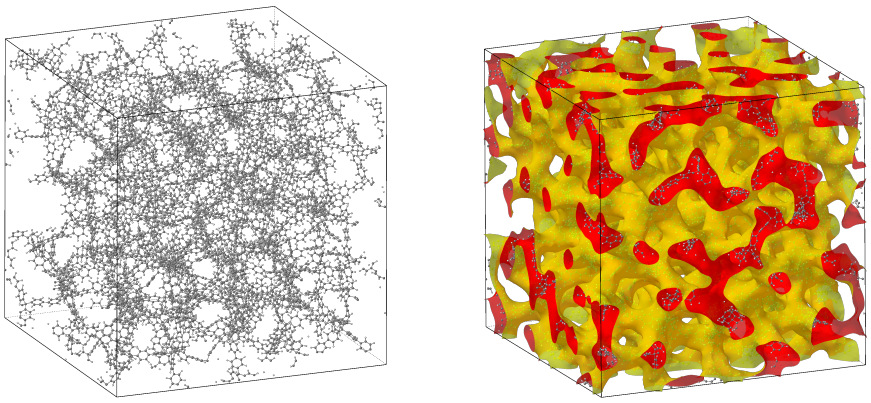

Figure 5.1: Atomic structure of amorphous PAF-1 from the model as relaxed by MD simulation at a temperature of 300 K, shown as atoms on the left and as highlighting the porosity on the right. The images constructed using the CrystalMaker visualisation tool [139].

an appropriate distance between the neighbouring points, and each connection between network points was decorated with planar 4,4′-biphenyl molecule. A Monte Carlo procedure was used to rotate molecules about their long axes in order to maximise the contact distances between the H atoms of neighbouring molecules. After this, a simple relaxation procedure was used to continue to maximise the contact distances between the H atoms, including allowing individual rings to rotate about the long axis of the molecule. The final configuration was then relaxed further using molecular dynamics simulations.

The configuration used in this work contains 10496 atoms (256 tetrahedral sites). One snapshot of the configuration after being relaxed by the simulation is shown in Fig. 5.1. This figure shows two views, one with the atoms and bonds, and the other showing the pores in the structure. From the simulation at a temperature of 300 K, the mean configuration edge length is 72.80 Å, giving a number density of 0.663 FU/nm$^3$ (FU is formula unit).

Table 5.1: Values for the parameters in the model interatomic potential, with key equations and references given in the text.

| Buckingham potential, Eq. (2.28), reference [140]. | | | |
|---|---|---|---|
| Atoms | $B$ (eV) | $\rho$ (Å) | $C$ (eV Å$^6$) |
| C–C | 270363 | 0.2667 | 1701.73 |
| C–H | 58551 | 0.2793 | 688.27 |
| H–H | 12680 | 0.2809 | 278.37 |
| Morse potential, Eq. (2.29), reference [141]. | | | |
| Atoms | $\epsilon$ (eV) | $\alpha$ (Å$^{-1}$) | $r_0$ (Å) |
| $C_{Tet}$–$C_{Phe}$ | 291.772 | 2.55 | 1.54173 |
| $C_{Phe}$–$C_{Phe}$ | 303.736 | 2.55 | 1.48218 |
| Bond angle potential, Eq. (2.30), reference [141]. | | | |
| Bonds | $\theta_0$ (deg) | $k$ (eV/rad) | |
| $C_{Phe}$–$C_{Tet}$–$C_{Phe}$ | 109.47 | 770.0 | |
| $C_{Tet}$–$C_{Phe}$–$C_{Phe}$ | 120 | 566.079 | |
| $C_{Phe}$–$C_{Phe}$–$C_{Phe}$ | 120 | 915.356 | |
| Torsion potential, Eq. (2.28), reference [142]. | | | |
| Atoms | $A$ (eV) | m | $\delta$ |
| C–C–C–C | 8.0 | 4 | 0 |

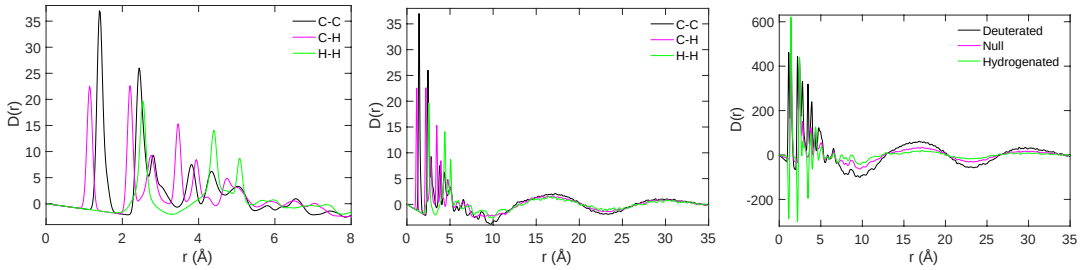


(a) Partial functions, low $r$ (b) Partial functions, wide $r$ (c) Combined functions

Figure 5.2: a,b) Comparison of the partial PDF functions $D_{\mathrm{norm}}(r)$ for each element pair, defined here as $r\,(g_{mn}(r) - 1)$, seen for the lower-$r$ range of data (a) and across the full range of distances (b); c) Comparison of the neutron PDF functions $D(r)$ for each sample. The PDFs were calculated from configurations obtained from the MD simulations performed at a temperature of 300 K.

### 5.2.5 Molecular dynamics simulations

Classical molecular dynamics (MD) simulations using force fields were performed using the software DL_POLY version 4.08 [55]. The phenyl rings were treated as rigid bodies. All atomic charges were set equal to zero; whilst this is clearly an

approximation, it is less important for a full network material than it would be for a pure molecular crystal.

Interatomic potentials for interactions between atoms other than the bonded C–C pairs (see below) were treated using the Buckingham potential introduced in Section 2.5.

The two C–C bonds outside the phenyl group, namely between the tetrahedral carbon and its neighbour within a phenyl ring, and between the two bridging atoms between two phenyl rings in the molecules, were modelled using a Morse potential (Eq. (2.29)). The values for the parameters $D$, $\alpha$ and $r_0$ for the two bonds were taken from the MM3 model [141], and are reproduced in Table 5.1.

Bond-angle potentials were modelled using Eq. (2.30). Values of the potential parameters $k$ and $\theta_0$ were again taken from the MM3 potential [141] and are reproduced in Table 5.1.

Finally a torsion interaction between the two phenyl rings in the 4,4′-biphenyl molecule was modelled using Eq. (2.28). The value of the parameter $A$ was taken from ab initio calculations [142], and is given in Table 5.1.

The actual MD simulations were performed initially in the constant-temperature [91, 92] constant-pressure or constant-stress [89, 90] ensemble, using a time step of 0.001 ps. The configurations were equilibrated for a simulated time of 20 ps and then run for s simulated time of 30 ps to obtain data for analysis, with configurations saved periodically for analysis. For a study of the atomic dynamics the simulations were perform in the constant-energy constant-volume ensemble, with the same running times.

## 5.3 Results

### 5.3.1 From atomic structure to the neutron total scattering functions

The atomic model has been shown above in Fig. 5.1. From the configurations a set of partial PDF functions $g_{m,n}$ were formed, and used to calculate normalised functions of the form $D_{\mathrm{norm}}(r) = r\,(g_{mn}(r) - 1)$. These are shown for the different atom pairs in Figs. 5.2a and 5.2b. The peaks for pairs within the rigid phenyl rings were calculated as $\delta$ functions, and for presentation and subsequent analysis were convolved with Gaussian functions to reflect thermal broadening. For distances above 10 Å, the pair PDFs show a slow oscillation with period of around 14 Å. These oscillations are more–or-less equal for each atom pair.

The partial PDFs are combined as described by Eq. (2.18) to give $D(r)$ functions for the three experimental cases of completely deuterated, partially deuterated to give close to null scattering from the H/D sites, and fully hydrogenous samples. The results are shown in Fig. 5.2. The key differences arise from the differences in scattering lengths, where $b_{\mathrm{D}} = 6.67$ fm, $b_{\mathrm{H/D}} \simeq 0$, and $b_{\mathrm{H}} = -3.74$ fm; for reference, $b_{\mathrm{C}} = 6.65$ fm [143]. Noting that the products of concentrations (from the chemical formula, the concentration for carbon $c_{\mathrm{C}} = 25/41$ and for hydrogen/deuterium $c_{\mathrm{H/D}} = 16/41$) are $c_{\mathrm{C}}^2 = 0.372$, $c_{\mathrm{H/D}}^2 = 0.152$ and $2c_{\mathrm{C}}c_{\mathrm{H/D}} = 0.476$, the oscillations in the PDF at higher $r$ are enhanced in the deuterated case, but significantly reduced in the hydrogenous case. This is clearly seen in Fig. 5.2.

The sine Fourier transforms of the combined calculated $D(r)$ functions to give the functions $Qi(Q)$ are compared with the experimental data in Fig. 5.3. The only adjustable agreement was a single scale factor applied to each data set to bring the calculated functions in line with the experimental data. The agreement is considered to be excellent, particularly – and importantly – considering that

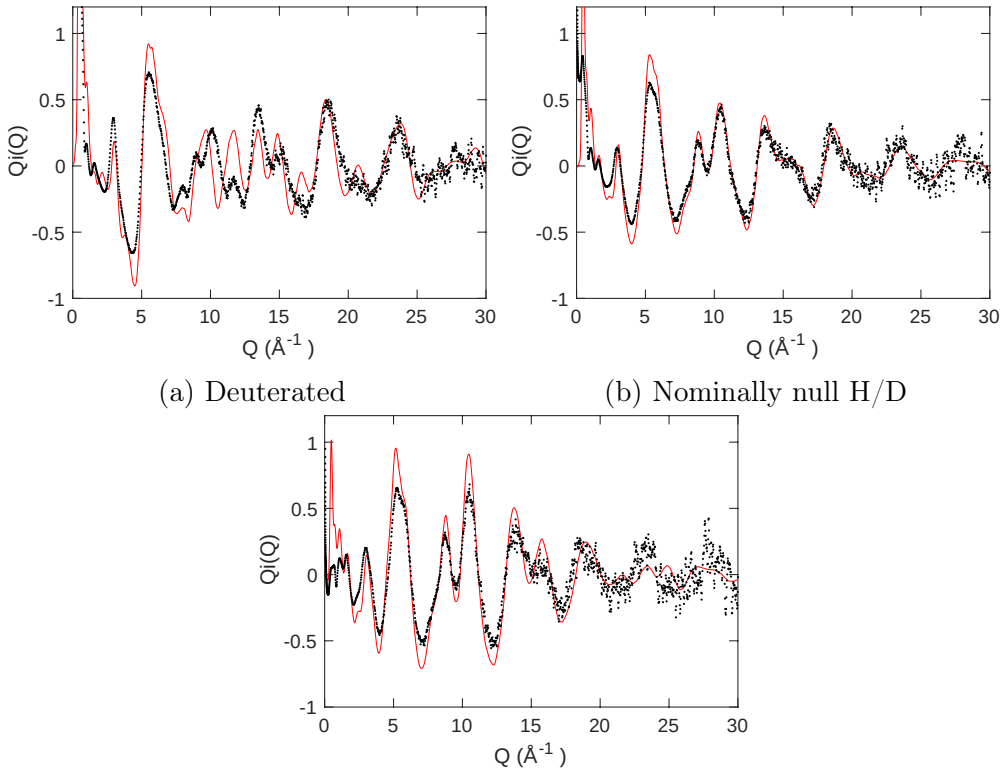


(a) Deuterated

(b) Nominally null H/D

(c) Hydrogenated

Figure 5.3: Comparison of $Qi(Q)$ functions calculated from MD at 300 K (red curves) and measured from total scattering experiments performed at 300 K (black points)

nothing about the model has been adjusted to give this agreement other than the value of the single overall scale factor.

What is also significant about the agreement between the calculated and experimental $Qi(Q)$ functions is that the calculation has reproduced the variation between the three different samples. Whilst broadly the peaks in the scattering functions of the three samples are in similar places, their relative heights and depths between them differ between the different samples. The only discrepancy between model calculation and experiment is in the case of the fully deuterated sample around $Q \sim 10$ Å$^{-1}$, but in the other two samples the agreement there is excellent.

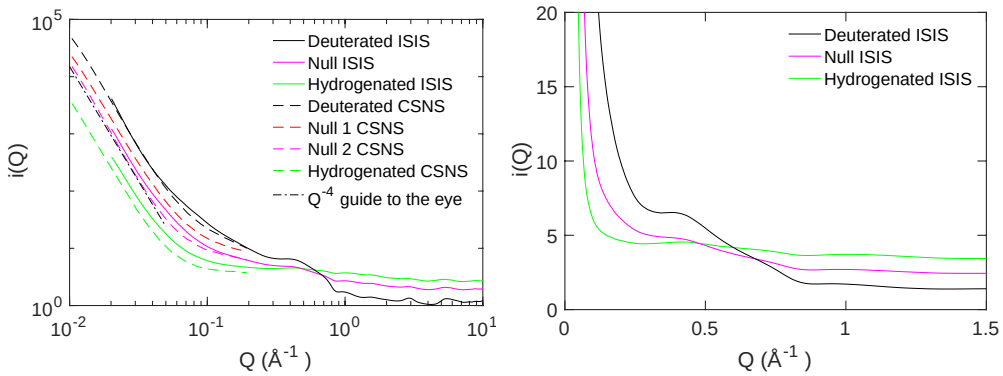


(a) Experimental, ISIS and CSNS

(b) Experimental, ISIS

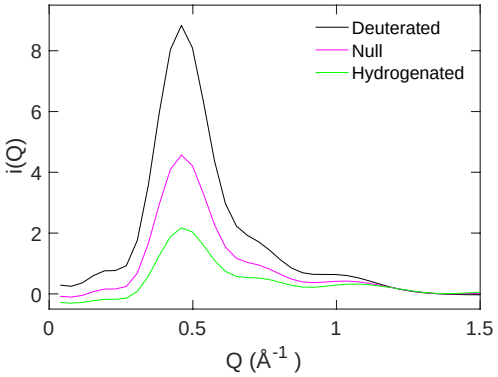


(c) Calculated

Figure 5.4: a) Comparison of the low-$Q$ regions of the measured $i(Q)$ function for each of the three compositions of amorphous PAF-1 at a temperature of 300 K, plotted logarithmically to highlight the small angle regime. Here data from ISIS (continuous curves, $0.02 < Q < 10$ Å$^{-1}$) and from CSNS (dashed curves, $0.01 < Q < 0.2$ Å$^{-1}$) are compared. The black dot-dash curve is of the form $Q^{-4}$ representing Porod scattering from particle surfaces. b) Comparison of the low-$Q$ regions of the experimental $i(Q)$ for each of the three compositions, highlighting better the peak at around $Q \sim 0.4$ Å$^{-1}$. c) Comparison of the low-$Q$ regions of the calculated $i(Q)$ from the MD simulations for each of the three samples at 300 K, showing the variation of the calculated peak at $Q \sim 0.45$ Å$^{-1}$ with composition.

### 5.3.2 Small angle scattering

Fig. 5.4 shows in more detail the scattering function $i(Q)$ at lower values of $Q$. In Fig. 5.4a the data for $0.01 < Q < 10$ Å$^{-1}$ from both ISIS and CSNS are plotted on logarithmic scales for both $Q$ and $i(Q)$. The CSNS data have been scaled to put onto the same scale as the ISIS data, but no account has been taken of the levels of background scattering in the CSNS data. Fig. 5.4a also shows a line of

the form $Q^{-4}$ to show that this closely represents the variation of $i(Q)$ for $Q$ below 0.05 Å$^{-1}$. This form of scattering is characteristic of Porod scattering arising from interference due to a discontinuous surface [144], which in this case means the particle surface. There is no sign of Guinier scattering associated with particle size in the data for $Q > 0.01$ Å$^{-1}$.

The low-$Q$ region of the $i(Q)$ data shown in Fig. 5.4 also shows a strong feature at $Q \sim 0.45$ Å$^{-1}$, as highlighted in the linear plot of the ISIS data in Fig. 5.4b. A peak at this value of $Q$ corresponds to an oscillation in the PDF with period of around 14 Å, exactly as was seen in Fig. 5.2. Indeed, this peak is reproduced, without the low-$Q$ Porod scattering, in the simulations as the Fourier transform of the computed $D(r)$ functions, as shown in Fig. 5.4c. The agreement with experiment is good in two regards. First, the position of the peak in $Q$ in the simulation matches the experimental position well, and secondly the variation of the peak intensity with changing composition from nominally-pure deuteration to nominally-pure hydrogenation in the calculation is consistent with the experimental data in Fig. 5.4b.

### 5.3.3 Analysis of the local atomic structure

The comparison between the calculated and experimental scattering factors for the three samples of PAF-1 gives confidence that the model based on a CRN of connected tetrahedral sites is a reasonable representation of the real amorphous structure. An analysis of some short-range aspects of the atomic structure – what is often called the "local structure" – is report from the MD simulations.

#### Interatomic distances

In MD simulation there are two critical C–C distances, namely the distance between two biphenyl rings, and between the tetrahedral carbon atom and linked

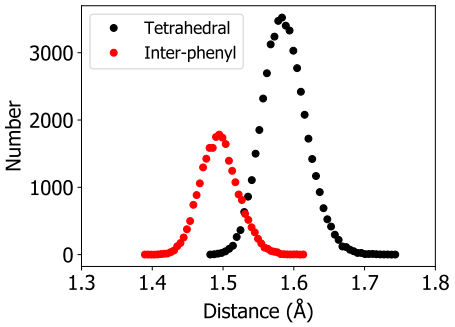


(a) C–C distances

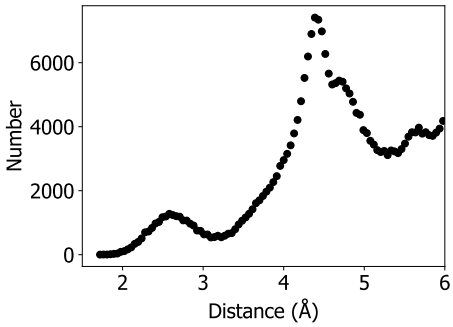


(b) End H–H distances

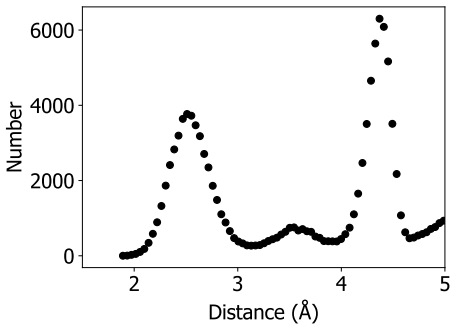


(c) Inter-phenyl H–H distances

Figure 5.5: Distribution of interatomic distances in amorphous PAF-1 at 300 K from MD simulations. a) Distribution of C–C bond distances. b) Distribution of H–H distances between the end hydrogens of different molecules around the tetrahedral carbon side c) Distribution of H–H distances between the hydrogens of different rings around the central C–C bond of the biphenyl molecules.

biphenyl ring; recall that the phenyl rings were kept rigid in MD simulations and therefore the intra-phenyl C–C distances are not considered. Fig. 5.5a shows the distributions of these two critical C–C distances. The inter-phenyl distance is the shorter of the two, but of course this reflects the choice of parameters in the interatomic potential, particularly the value of $r_0$ in the Morse potential (Eq. (2.29)) as presented in Table 5.1.

Two types of H–H distance distributions are considered here. The first, shown in Fig. 5.5b, concerns the H atoms at the ends of the biphenyl molecules closest to the tetrahedral carbon, and consider the distances between these two H atoms in each molecule and the pairs of H atoms in their four neighbours. The first peak in

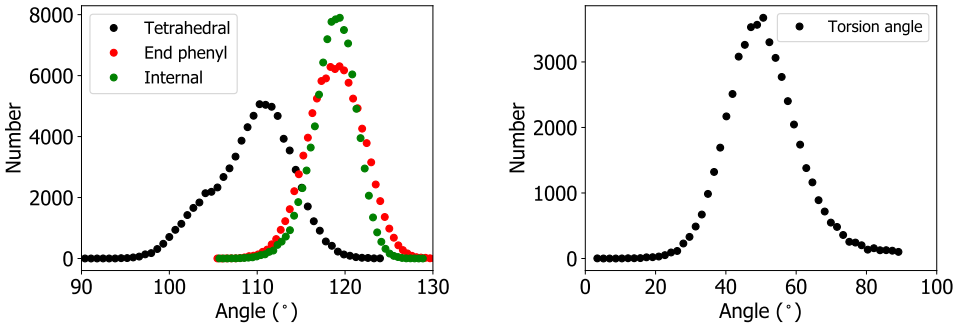


(a) C–C–C angles (b) Torsion angles

Figure 5.6: Distributions of a) C–C–C bond angles, and b) phenyl torsion angles, obtained from the MD simulations of amorphous PAF-1 at a temperature of 300 K.

the distribution function, around 2.5 Å, represents the closest approach of H atoms in neighbouring phenyl rings. The position of this peak is consistent with the distance in the ideal crystal structure, which is also around 2.5 Å. The distribution shows a satisfactory relaxation of the local structure around the tetrahedral site.

Fig. 5.5c shows the second interesting H–H distance, namely between closest H atoms in the two phenyl rings in the middle of the biphenyl molecule. The first peak in this distribution function has the same mean distance as for the distribution of H–H distances about the tetrahedral carbon. This mean distance of around 2.5 Å corresponds to a 45° torsion angle between two phenyl rings rotating about the long axis, which is longer than the distance of around 1.7 Å for a planar biphenyl molecule and shorter than the distance of around 3.6 Å for a 90° torsion angle. The distribution of angles is discussed below.

### Bond and torsion angles

There are three important C–C–C angles, namely the angle subtended on the tetrahedral site (nominally 109.47°), the angle between subtended on the carbon atom bonded to the tetrahedral site (nominally around 120°), and the angle sub-

tended on the carbon atoms on one phenyl ring that are linked to the neighbouring phenyl ring within a molecule (also nominally around 120°). The angles within the phenyl ring themselves are not considered here. For each of these the simulation model defines a specific bond angle potential, with parameter values given in Table 5.1.

Fig. 5.6a shows the distribution functions for all three angles. The distributions of the second two angles are almost identical, with same position (equivalent to the nominal position) and width. On the other hand, the distribution of tetrahedral angles is much broader, by around a factor of 2, and the distribution is not quite symmetric.

Fig. 5.6b shows the distribution of biphenyl torsion angles. This is centred around a torsional angle of 45°, with a width of around 20°. This is consistent with a DFT study [142], and fully consistent with the discussion of inter-phenyl H–H distances shown in Fig. 5.5c as discussed above.

### 5.3.4 Comparison with a hypothetical diamond-like crystal structure

#### Model

The starting point for the discussion about PAF-1 was the aspiration of original researchers to create a diamond-like crystal structure. Given the close similarities between the short-range atomic structures of amorphous silica and the diamond-like cristobalite crystal structure [145], it is likely that it is reasonable to explore a crystalline version based on an initial diamond network of tetrahedral sites. A diamond-like PAF structure for use in MD simulations was constructed using the same method as used to construct an amorphous structure, as discussed in Section 5.2.4. The sample contained 512 tetrahedral sites as a $4 \times 4 \times 4$ supercell of the basic diamond-type unit cell, with a total of 20992 atoms.

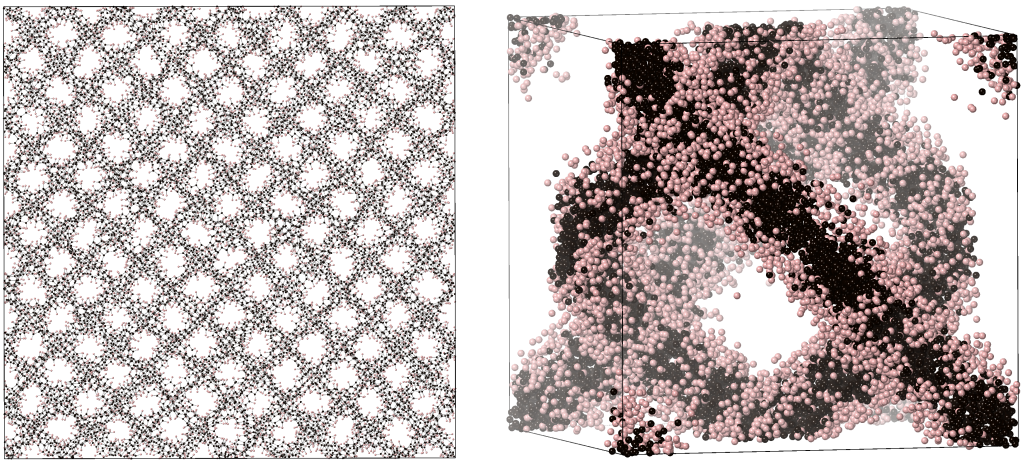

(a) (b)

Figure 5.7: Projection of the simulated crystal configuration of cubic metric at a temperature of 300 K, a) viewed down one of the cube axes, and b) showing a view of the configuration collapsed into one unit cell, with a fading based on distance from the viewer. Carbon and hydrogen atoms are shown as black and pink spheres respectively.

Two types of simulation are performed , first constraining the cubic metric while allowing the volume to change in a constant-temperature constant-pressure ensemble (NPT), and second allowing the simulation box to change shape as well as size in a constant-temperature constant-stress ensemble (NST).

### Atomic structure with the cubic metric

One of the NPT configurations is shown in Fig. 5.7, both as a simple projection and with all atoms collapsed back into one unit cell. Both highlight the diamond-type network in different ways. The Bragg powder diffraction patterns from both the whole and collapsed configurations are calculated. In both cases the calculated diffraction patterns are consistent with space group $Fd\bar{3}m$, identically with the cubic $\beta$-cristobalite phase of silica. In this case, the first Bragg peak has index 111, and it is noticeably the strongest Bragg peak. Other strong Bragg peaks include those with indices 220, 222, 331, 333, 440, 442 and 353, with weaker peaks including 311, 400 and 422. This particular space group implies some degree of

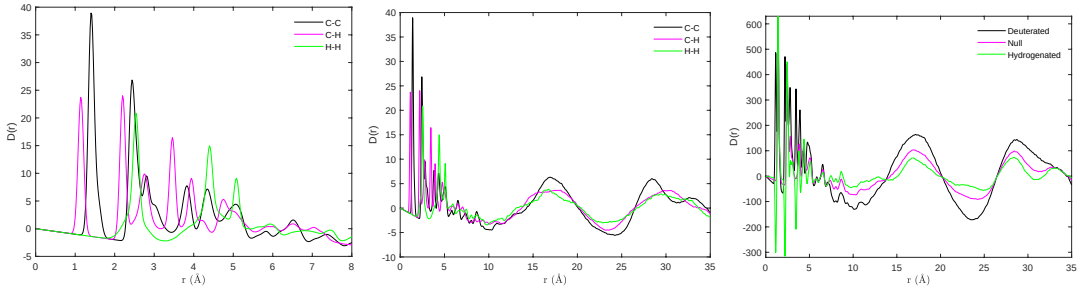


(a) Partial functions, low $r$ (b) Partial functions, wide $r$ (c) Combined functions

Figure 5.8: a,b) Comparison of the partial PDF functions $D(r)$ for each element pair in the crystalline phase of PAF-1 of cubic metric, defined here as $r\,(g_{mn}(r) - 1)$, as calculated from a MD simulation performed at a temperature of 300 K. Results are shown for the lower-$r$ range of data (a) and across the full range of distances (b). Panel c) gives a comparison of the neutron PDF functions $D(r)$ for each sample, formed from Eq. (2.18). These data should be compared with the corresponding functions shown in Fig. 5.2.

orientational disorder of the phenyl groups around the long axis of the biphenyl molecule.

The calculated PDFs for the NST ensemble are shown in Fig. 5.8, for comparison with the corresponding PDFs from the amorphous phase shown previous in Fig. 5.2. Over the range of data $r < 8$ Å – Fig. 5.8a – the partial PDF functions are almost identical to those seen in the amorphous phase, Fig. 5.2a. Whilst a large part of the PDF over this range includes intra-biphenyl distance correlations, there are also important inter-phenyl correlations within the biphenyl molecules and between neighbouring molecules around the tetrahedral sites. What can be concluded clearly from this analysis is that the short-range structure of the cubic crystalline phase is very similar to that of the amorphous phase, which is consistent with the discussion above about there being some degree of orientational disorder consistent with the apparent space group symmetry.

Figs. 5.8b and 5.8c and show the partial and combined PDFs over a wider range of distance, up to 35 Å. As highlighted in the case of the amorphous PAF, Figs. 5.2b and 5.2c, the existence of an oscillation in each of the PDFs with a

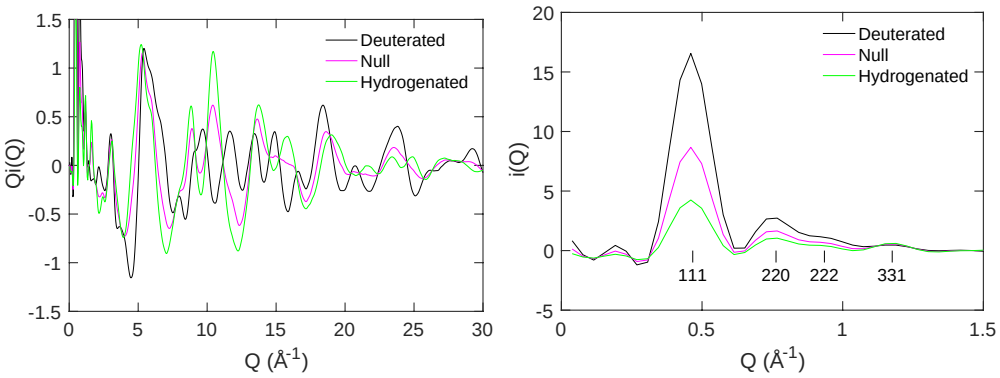


(a) (b)

Figure 5.9: a) Comparison of the scattering functions $Qi(Q)$ for the three crystalline materials, calculated from the MD simulations performed at a temperature of 300 K; b) Comparison of the corresponding functions $i(Q)$ for lower values of $Q$ highlighting the Bragg reflections (broadened by the finite range of the PDF transformed to give $Qi(Q)$).

period of around 14 Å. These oscillations are seen also in the PDFs of cubic crystalline configuration, but with higher intensity and a structure that is less symmetric. The fact that the PDFs are weaker at higher $r$ is not dissimilar to the way in which the PDF of amorphous silicon is remarkably similar to that of $\beta$-cristobalite but attenuated at larger-$r$ [145].

As discussed in Section 5.3.2, the Fourier transform of this oscillation will give a peak in the scattering function. In this case, it corresponds to the 111 Bragg peak, which is reminiscent of the fact that the first sharp diffraction peak in amorphous silica, $Q = 1.53 \pm 0.02$ Å$^{-1}$, [114] corresponds closely to the 111 Bragg peak in $\beta$-cristobalite (lattice parameter $a = 7.13$ Å, [101] corresponding to the Bragg peak at $Q = \sqrt{3} \times 2\pi/a = 1.53$ Å$^{-1}$). This leads into a general discussion of the scattering function.

### Scattering functions with the cubic metric

The scattering functions $Qi(Q)$ calculated for the crystal phase with deuterium, with a null deuterium/hydrogen mix, and with hydrogen are shown in Fig. 5.9a.

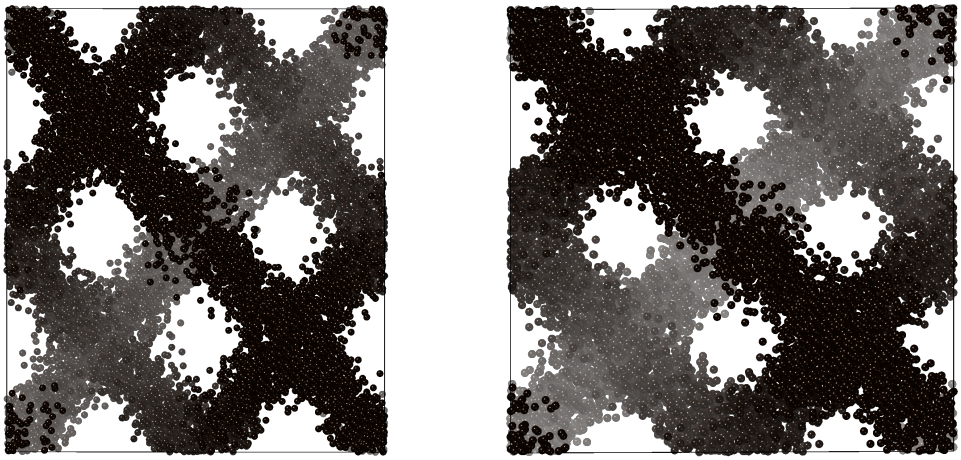

(a) Projection down [100] (b) Projection down [001]

Figure 5.10: Projection of the simulated crystal configuration relaxed without imposition of the cubic metric at a temperature of 300 K, viewed down the a) [100] and b) [001] axes, and showing only the carbon atoms with a fading based on distance from the viewer.

They can be compared by eye with the corresponding functions calculated for the amorphous phase, Fig. 5.3; it is seen that the functions for the crystalline phases are in very close agreement with those calculated for the amorphous phase. This is not surprising given the similarities of the PDFs in both cases (Figs. 5.2 and 5.8). The only differences, as noted above, are at higher $r$, and this difference feeds through to the difference between a broad peak and a Bragg peak, where the latter should be a Dirac $\delta$-function. In practice the finite range of $r$ used in the Fourier transform, means that the Bragg peaks will be broadened by an amount of order $2\pi/r_{\max}$. The low-$Q$ part of the scattering function $i(Q)$ is shown in Fig. 5.9b, which can be compared with the corresponding function for the amorphous phase in Fig. 5.4c. It can be seen that the scattering from the crystalline phase is sharper than for the amorphous phase (as noted, broadening by the finite range of $r$ in the PDF), and the Miller indices of the prominent peaks are indicated in the scattering function.

**Structure without the constraint of the cubic metric**

Unexpectedly, without the constraint of the cubic metric, allowing changes to both the shape and size of the atomic configuration during the simulation, it is found that the crystal structure transforms to one of tetragonal metric, apparently with a disordered structure as in the metrically-cubic phase. Projections of the atomic structure collapsed onto one unit cell are shown in Fig. 5.10. This structure has a density lower than that of the metrically cubic crystal by around 2.5%. There is an expansion along the [001] direction by around 11%, and a contraction in the perpendicular plane by about 6%.

### 5.3.5 First diffraction peak

There has been a long-standing question about the nature of the first peak in the diffraction patterns of amorphous materials, particularly because this peak is usually the sharpest [146–154]. Of relevance here is the first sharp diffraction peak (FSDP) in amorphous silica noted above. It is also pertinent to note there is a corresponding peak in amorphous ZIF at $Q \sim 1$ Å$^{-1}$, which as noted earlier has an atomic structure similarly based on that of a tetrahedral CRN, although there appears not to be a corresponding diamond-like crystal structure.

A metric length scale from the density can be defined to give a correspondence with the $d$-spacing of the 111 peak of the corresponding diamond-type crystal structure of the same atomic density: $\ell = (8/\rho_{\rm t})^{1/3}/\sqrt{3}$, where $\rho_{\rm t}$ is the number of tetrahedral sites per unit volume. For silica, amorphous ZIF, and PAF there are the following results for $2\pi/\ell$ and the position of the first-sharp diffraction peak, $Q_{\rm FSDP}$:

What is interesting is that the position of the FSDP scales closely with the density of tetrahedral sites, as given by $2\pi/\ell$. The scaling is not so good for ZIF as it is for silica and PAF, but in these other two cases it is almost exact. The

Table 5.2: A comparison of FSDP parameters for different example materials.

| Material | $\ell$ (Å) | $2\pi/\ell$ (Å$^{-1}$) | $Q_{\mathrm{FSDP}}$ (Å$^{-1}$) | Ref. |
|---|---|---|---|---|
| Silica | 4.117 | 1.526 | 1.53 | [114] |
| ZIF | 7.787 | 0.807 | 1.075 | [117] |
| PAF | 13.242 | 0.474 | $\sim 0.45$ | – |

FSDP, as has been pointed out before, represents not a distance in the glass (it isn't a correlation length) but a period of oscillation in the atomic density. In the case of silica and ZIF, the oscillations with wavelength $\ell$ are not very different from interatomic separation and not clear in the PDF, but in the case of PAF the oscillations extend beyond the range of the strong and identifiable interatomic peaks in the PDF over the range 0–10 Å, Fig. 5.2. As noted, these oscillations are stronger still in the crystal phase, Fig. 5.8. The oscillations occur in all three types of atom pair (C–C, C–H and H–H).

This is an intriguing result, given the important of the debate around the origin of the FSDP in amorphous silica and the fact that both are based on similar networks with similar connecting rings of atoms and associated pores within the network. The effect is magnified in the case of PAF. It is not possible to say more here, but does point to the possibility of resolving the controversy of the FSDP with further research starting from porous framework materials as the end-point of a spectrum of tetrahedral amorphous networks with different connectors and densities rather than silica as the other end point.

### 5.3.6 Effect of temperature

Simulations performed at several temperatures show clearly that the PAF-1 network undergoes negative thermal expansion. The volume per formula unit is plotted as a function of temperature in Fig. 5.11. At the higher temperatures the coefficient of thermal expansivity is equal to $-24$ MK$^{-1}$. which is comparable to that of many significant NTE materials [155].

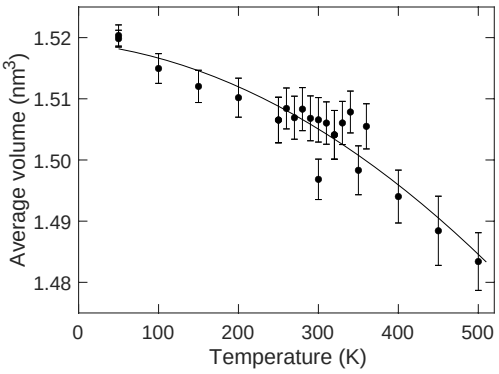


Figure 5.11: Volume of the PAF-1 network as a function of temperature obtained from the MD simulations reported in this paper. The curve is a guide to an eye, obtained as a fitted second-order polynomial.

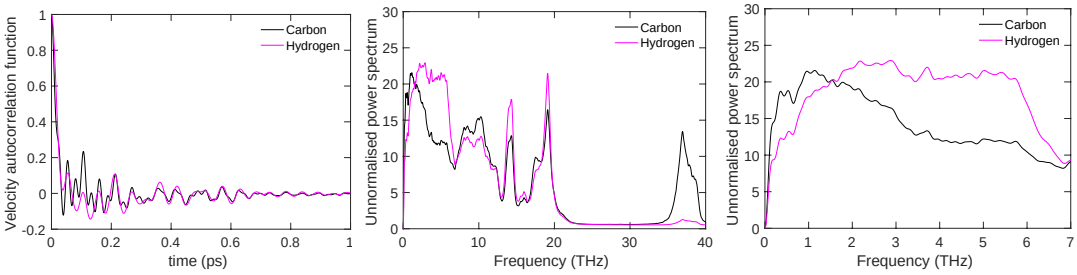


(a) (b) (c)

Figure 5.12: a) Velocity autocorrelation functions for C (black) and H (magneta) atoms in the MD simulation of 300 K. b,c) Associated power spectra of the two velocity autocorrelation functions over the full range of frequencies (b) and over the range of low frequencies highlighting better the zero-frequency limit (c).

It is not surprising that the PAF network shows NTE, because in its idealised form it has maximum volume, so fluctuations in local structure involving rotations and displacements of the biphenyl molecules will necessarily give rise to NTE through the tension mechanism. This has been discussed in several places, and particularly pertinent is the discussion of networks where the linkers are rod-like molecules, such as $Zn(CN)_2$ and $Si(NCN)_2$.

### 5.3.7 Analysis of the network dynamics

The time-dependent velocity autocorrelation functions for the C and H atoms were calculated separately, and are shown in Fig. 5.12a. One expects the correlation

functions for the two atom types to be broadly similar given that the phenyl rings are held rigid in the simulation, with the two differences coming from the terminal 4,4′ C atoms in the biphenyl molecules, and from the tetrahedral C atoms.

The Fourier transforms of the velocity autocorrelation functions give the power spectrum, corresponding to the vibrational density of states. The power spectra for carbon and hydrogen atoms are shown in Figs. 5.12b and 5.12c. It should be remembered that the power spectra do not include internal vibrations of the phenyl groups.

The highest frequency group in the power spectra is around 33 THz, and it is strong for the carbon atoms and very weak for the hydrogen atoms. By comparison with a vibrational analysis of a carbon tetra-4-biphenyl cluster performed using the, it is clear that this group is strongly associated with vibrations of the tetrahedral carbon atoms with variation of the C–C bond length. The feature around 18 THz corresponds to motions of the phenyl groups that bend the tetrahedral C–C–C angles. The lowest-frequency peak extending below 0.5 THz corresponds to rotations of the biphenyl molecules. These are the modes that will give rise to the negative thermal expansion seen above, corresponding to flexing of the network without distortions of the $CC_4$ tetrahedra or flexing of the biphenyl molecules.

## 5.4 Summary

The main achievement in this paper has been to demonstrate that an atomic model for amorphous PAF based on a continuous random network of connected tetrahedral sites provides a good description of the neutron scattering function. The atomic structure was relaxed by molecular dynamics simulations, and this allowed a detailed characterisation of the atomic structure. The neutron scattering experiments were performed using isotopic substitution of deuterium for hydrogen, which includes the case where the scattering is primarily from C–C correlations,

and in the cases of pure hydrogen and pure deuterium gives a different balance of scattering from C–C and H–H correlations, but more importantly changes the sign of the contribution from the C–H correlation. It is found that good agreement is obtained for all three H/D ratios used in this study.

The atomic structure given by the MD simulations has been characterised by considering distributions of interatomic distances, bond angles, and torsional angles. The atomic structure is able to relax well in two regards, firstly to maintain a reasonable distribution of biphenyl torsion angles, and secondly by reasonably avoidance of close H...H contacts around the tetrahedral site. The simulations do show some angular distortions around the tetrahedral site.

Comparison with a hypothetical crystal based on the diamond structure – analogous to the $\beta$-cristobalite form of silica – suggested that if there is a crystalline form it is likely to have orientational disorder of the phenyl groups about the long axis of the molecule. Atomic distribution functions for the crystalline phase are remarkably similar to those of the amorphous phase.

One very interesting result is the presence of long-period oscillations in the pair distribution functions for all three types of atomic correlations, which give rise to a first sharp diffraction peak in both the calculation and measurement of the scattering function. The calculation of the how the peak varies with isotopic substitution is consistent with the experimental results. This peak corresponds to the strong 111 Bragg reflection from the crystalline phase in a way that is exactly analogous with the correspondence between the first sharp diffraction peak in amorphous silica and the 111 Bragg peak in $\beta$-cristobalite.

The samples studied show very strong small angle scattering with a classical Porod form proportional to $Q^{-4}$, consistent with scattering from particulate surfaces. The existence of strong scattering made it hard to separate the small-angle scattering from the wide-angle scattering, which meant that accurate extraction of the pair distribution function was not possible. Hence the comparison between

simulation and experiment is with the scattering function only.

The combination of neutron total scattering on samples of different isotopic composition with molecular dynamics simulation has successfully confirmed and characterised the proposed atomic structure of the amorphous phase of PAF. This approach can be commended for application to other amorphous organic network materials.

# Chapter 6

# Orientational disorder and the giant entropy of phase transition in ammonium sulfate $(NH_4)_2SO_4$

## 6.1 Introduction

Ammonium sulfate (AS), $(NH_4)_2SO_4$, at room temperature is paraelectric. It becomes ferroelectric at 223 K[156]. Its space group changes from $Pnam$ to $Pna2_1$ (The conventional setting of space group 62 is $Pnma$. $Pnam$ is chosen for ease of comparison with the low-temperature $Pna2_1$ phase.) , accompanied by a loss of mirror plane $ab$, a loss of the inversion centre and a spontaneous polarization along the c axis[157]. It can be seen from Fig. 6.1 that the mirror plane in the HT phase is perpendicular to the c axis at 1/4 c. The hydrogen bonds are also symmetric about mirror plane. Although the space group becomes polar in the LT phase, the displacements of C and N atoms are small and the primary effect of the phase transition is slight rotations of the $ND_4^+$ and $SO_4^{2-}$ tetrahedra.

AS has been well studied in terms of its crystal structure and ferroelectric properties. Recently, it regathers momentum because of the potential applications

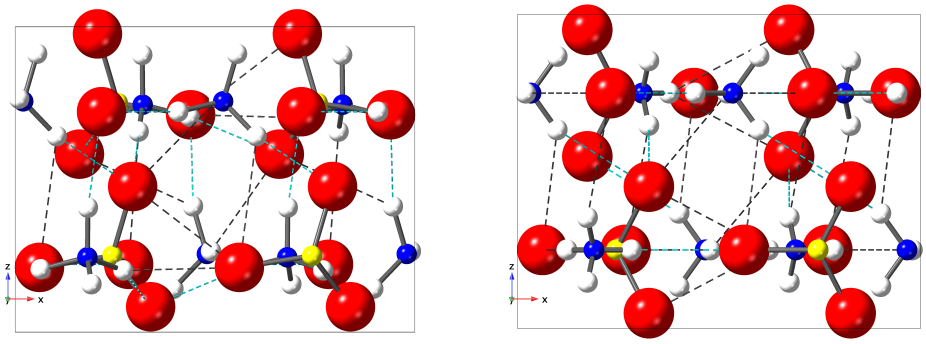

(a) fig:LT phase $Pna2_1$ (b) fig:HT phase $Pnam$

Figure 6.1: The unit cell structure of (a) LT phase $Pna2_1$ and (b) HT phase $Pnam$ viewing from the b axis. The D, N, O, S atoms are in white, blue, red and yellow respectively. The cyan dash line represents the short hydrogen bonds (0 – 2.3 Å). The grey dash line represents the long hydrogen bonds (2.3 – 2.6 Å).

associated with its caloric effect [158].

### 6.1.1 Caloric effect

The caloric effect is a phenomenon that the material experience a reversible temperature change under an external field. The external field can be a magnetic field (magnetocaloric), an electric field (electrocaloric), and pressure (barocaloric). The cooling performance for a caloric material is based on two quantities, the adiabatic temperature change $\Delta T$ and the isothermal entropy change $\Delta S$ [159].

Caloric effects are not rare. Many materials show a large caloric effect during their ferroic phase transitions[160]. This is not hard to understand since these phase transitions are usually accompanied by a relatively large isothermal entropy change. Among all the ferroelectric materials, the largest known isothermal entropy change belongs to the ferroelectric phase transition of ammonium sulfate ($\Delta S = 17.6$ Jmol $\cdot$ K$^{-1}$). with great potential. This enables ammonium sulfate a natural candidate for electrocaloric materials. However, its ionic conductivity limits its capacity to a large electric field (highest electro-caloric measurement at 400 kVcm$^{-1}$ [161]). J.F. Scott suggested ammonium sulfate is still very promising for electrocaloric applications if its conductivity can be greatly reduced by admixtures or some

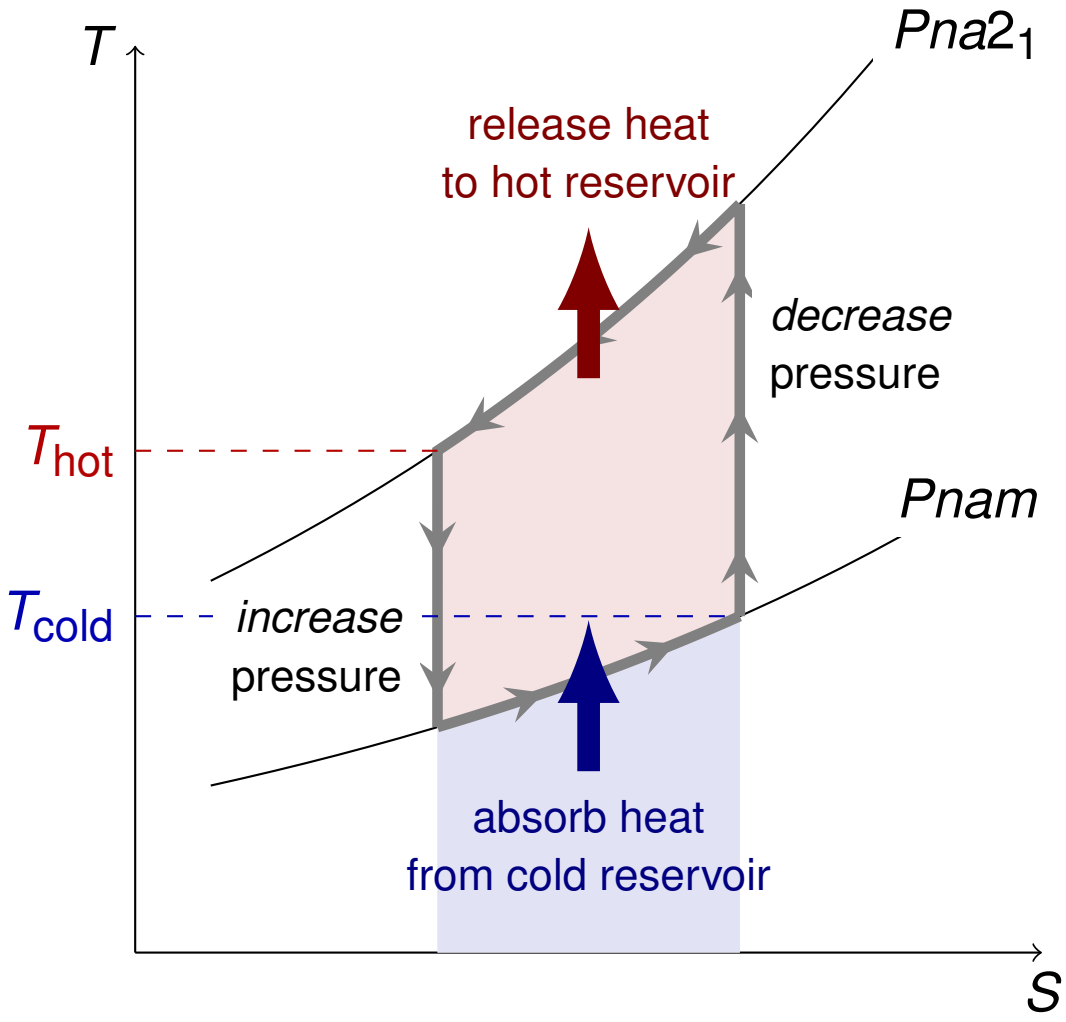


Figure 6.2: The cooling mechanism based on inverse caloric effect. An increased pressure results a phase transition of AS from the low entropy LT phase to the high entropy HT phase. When the entropy increases, it will absorb heat from the cold reservoir. A decreased pressure results a phase transition of AS from the high entropy HT phase to the low entropy LT phase. When the entropy decreases, it will release heat to the hot reservoir. The pressure can be replaced by a magnetic field, or an electric field for other caloric materials. The figure is drawn by Dr Anthony Phillips.

other methods[162]. Recently, the caloric effect of ammonium sulfate is found to be not only triggered by the electric field but also by applying pressure near its ferroelectric phase transition[158].

A possible cooling mechanism based on the inverse barocaloric effect (absorbing heat when the pressure is increased) of AS is illustrated in Figure 6.2. By applying

a proper pressure, the low entropy LT phase of AS will transform to the high entropy HT phase of AS. During this phase transition, the AS will absorb heat from the outside environment. Decreasing the pressure can make the high entropy HT phase of AS transform to the low entropy LT phase of AS, during which the AS will release heat to the outside environment.

The extraordinary barocaloric performance of AS is strongly dependent on its large entropy change during the ferroelectric phase transition. Understanding why such a large entropy change occurs at a simple structure as AS (a network of two types of tetrahedra $ND_4^+$ and $SO_4^{2-}$) could provide fundamental insight into design of materials requiring large entropy change.

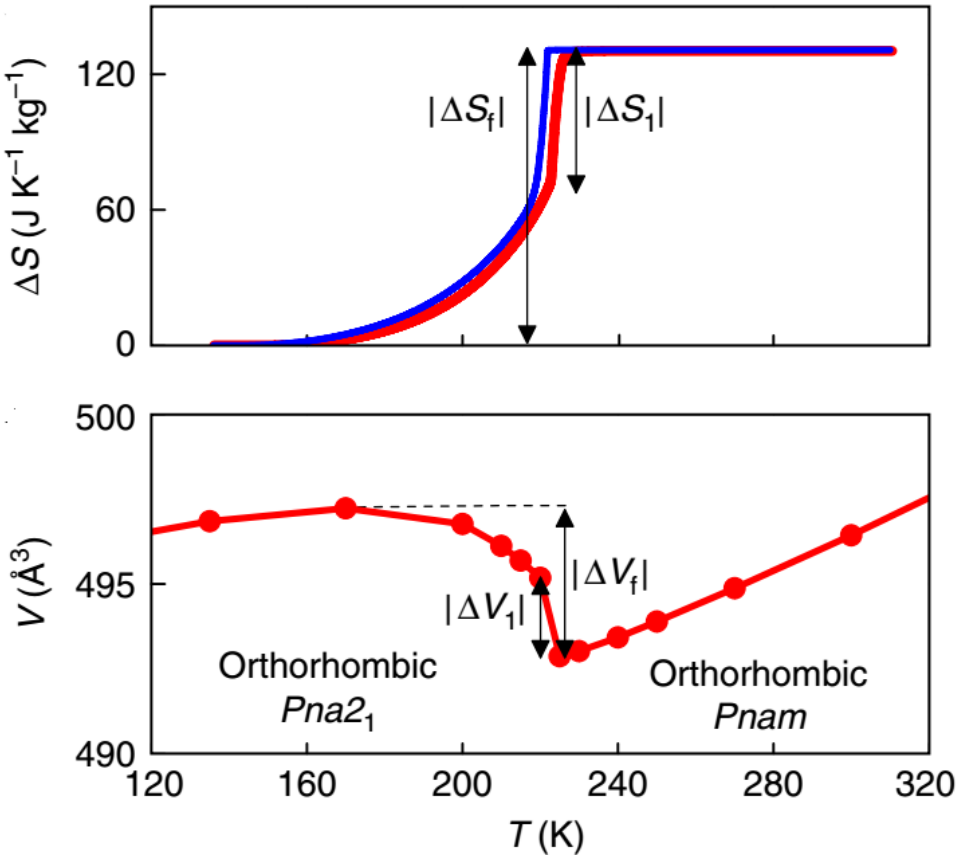


Figure 6.3: AS cell volume and entropy change during the ferroelectric phase transition[158]

Figure 6.3 shows the entropy and cell volume change of ammonium sulfate

during the ferroelectric phase transition. The decreasing unit cell volume suddenly become increasing along with the decrease of the temperature at the first order phase transition. In the meantime, the thermal expansion of the unit cell becomes negative in the LT phase from positive in the HT phase. The negative thermal expansion exists until AS is further cooled down to 160 K. Reflecting this on the entropy change, there is a sudden entropy decrease at the first order transition and a continuous entropy decrease until 160 K [158].

According to the Maxwell relation,

$$\Delta S = -\int_{P_i}^{P_f} (\partial V/\partial T)_p \mathrm{d}P \tag{6.1}$$

there is always high entropy change associated with large volume change. Yet this explanation alone is not enough to elucidate the underlying entropy change mechanism associated with the microscopic structure change of AS.

### 6.1.2 Previous structure studies of AS

As mentioned above, there were lots of studies of AS. They can be divided into two streams. One stream focuses on crystal structure studies mainly based on diffraction. The other stream focuses on searching for a vibrational mode responsible for the ferroelectric phase transitions.

There is some disagreement about the structure of the LT phase. Katsuhiko carried out a series of xray diffraction studies on ammonium sulfate. He inferred the ammonium ions in the LT phase can orient to either side of the ab mirror plane by refining the occupancies of two differently oriented ammonium ions (actually 4 in total because there are two symmetry non-equivalent ammonium ions in the LT phase) in Rietveld refinement[163] while the neutron diffraction data measured by Elmer et al. [164] and X-ray single crystal data measured by Leszek et al. [165] suggest the LT phase orientation of ammonium ions can only orient to one side of the mirror plane. A DFT study on AS claims there are

one stable configuration and 3 metastable configurations for the LT phase. Each configuration is unique in terms of the relative orientation of the ammonium and sulfate ions and calculated lattice parameters [166]. The diffraction studies also suggest there are slight distortion of $ND_4^+$ and $SO_4^{2-}$tetrahedra [164, 165].

Katsuhiko et al. measured X-ray diffuse scattering on the HT phase of AS[167], in which they claimed the diffuse scattering observed could be explained by a phonon mode associated with the librational move of sulfate ions. Jain et al. believe the phase transition can be attributed to the internal distortion and librational moves of sulfate ions. Thus, they predicted there is a key mode corresponding to such vibration [168][169]. On the contrary, Torrie et al. suggested the phase transition is related to the librational moves of $NH_4^+$ ions [170]. Later studies propose the key phonon mode is associated with the collective reorientation of $NH_4^+$(I) - $SO_4^{2-}$ - $NH_4^+$(II)[171].

## 6.2 Experimental and analysis method

### 6.2.1 Neutron scattering measurements

Previous studies have proved deuterated ammonium sulfate $(ND_4)_2SO_4$ has no significant difference with natural abundance AS in terms of phase transition temperatures and thermal properties [172]. Deuterated AS samples are used for the total scattering experiment in order to avoid the data noise caused by the H atoms. The neutron total scattering data was measured on the GEM diffractometer at ISIS. The sample was loaded in a cylinder vanadium can with 6mm diameter. The vanadium can was put in the cryostat environment (closed cycle refrigerator CCR). A series of 15-minute-short runs are measured to extract the lattice parameters and 6-hour-long runs were measured for 6 temperatures 150 K, 180 K, 210 K, 240 K, 270 K and 300 K for total scattering data measurements. The data reduction

Table 6.1: Potentials for AS RMC refinement.

| Bond potential | | |
|---|---|---|
| Atoms | Energy (eV) | equilibrium distance (Å) |
| N–D | 2.63 | 1.01 |
| S–O | 3.23 | 1.48 |
| **Bond angle potential** | | |
| Bonds | Energy (eV) | equilibrium angle (°) |
| D–N–D | 3.9 | 109.47 |
| O–S–O | 12.85 | 109.47 |

was performed with the software MANTID[173].

### 6.2.2 Analysis of the neutron scattering data

The short-run data was analysed by the Rietveld refinement using the `GSAS`/`EXPGUI` programs. The starting models for both the LT and HT phase were adopted from the single crystal models refined by Dr. A.E.Phillips. The long-run data were transformed to the appropriate scattering functions $i(Q)$ and pair distribution functions $D(r)$ using standard procedures introduced in Section 2.3. The data correction, normalization and Fourier transform were all performed using the `GUDRUN` package.

### 6.2.3 Reverse Monte Carlo simulation

The Reverse Monte Carlo simulation was performed using the `RMCprofile` code [51]. Configurations of both the LT and the HT phase used a $6 \times 5 \times 8$ supercell based on the refined crystal structure, set up using the `data2config`/`RMCcreate` code [77]. Each configuration contains 14400 atoms. The RMC simulations were carried out for at least $2 \times 10^6$ steps in total until convergence, giving 10.67 accepted moves per atom and an average move acceptance rate of 7.68%. Bond and angle potentials are used in the RMC refinement. The potential details are tabulated in Table 6.1.

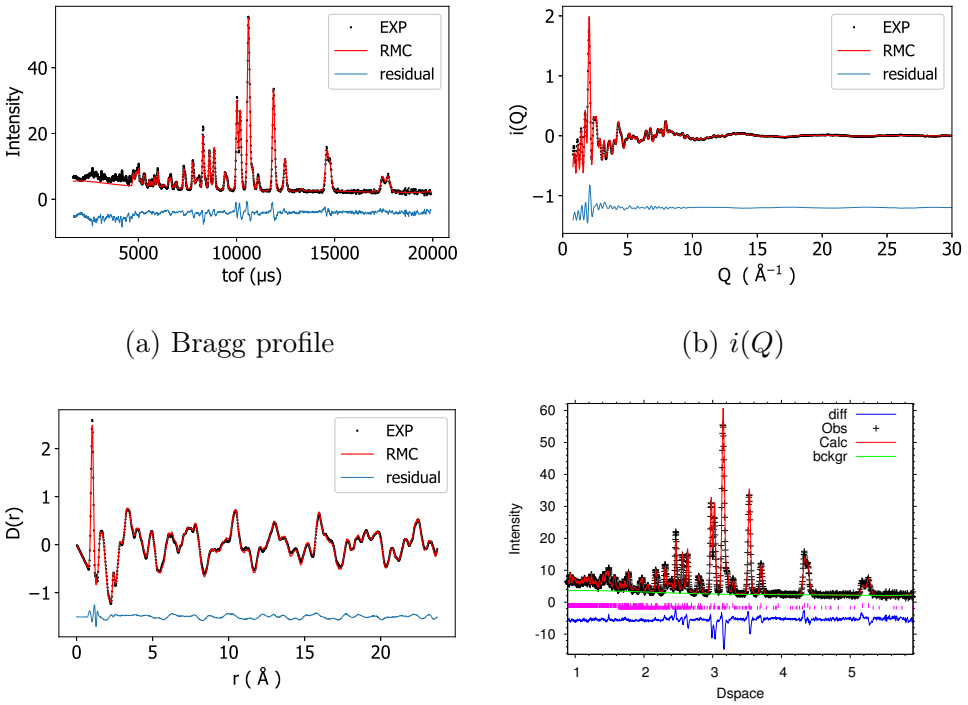


(a) Bragg profile

(b) $i(Q)$

(c) D(r)

(d) Rietveld refinement

Figure 6.4: Representative fits from RMC simulation at 150 K of (a) Bragg pattern, (b) total scattering function, (c) pair distribution function and d) Rietveld refinement for AS.

## 6.3 Structure insight from RMC configurations

As shown in Fig. 6.1, the differences between the LT and HT phases of AS are only slight tilts of ammonium and sulfate ions. This subtle change in symmetry is difficult to see from the Bragg profiles. There is no change in terms of the lattice type and systematic absence as well as no new or splitting Bragg peaks. The rigid body constraint was applied for the $ND_4^+$ and $SO_4^{2-}$ tetrahedra in the Rietveld refinement but it can not achieve a good fit without a very large negative $L_{33}$ parameter for $ND_4^+$. If the rigid body constraint is not applied, the final refined model will have very distorted $ND_4^+$ and $SO_4^{2-}$ tetrahedra (0.2 Å bonds difference for both N–D bonds in $ND_4^+$ and S–O bonds in $SO_4^{2-}$). Therefore, the refined model with the rigid body constraint was adopted for RMC refinement and only lattice parameters are extracted from the Rietveld refinement as the

reliable structure parameters.

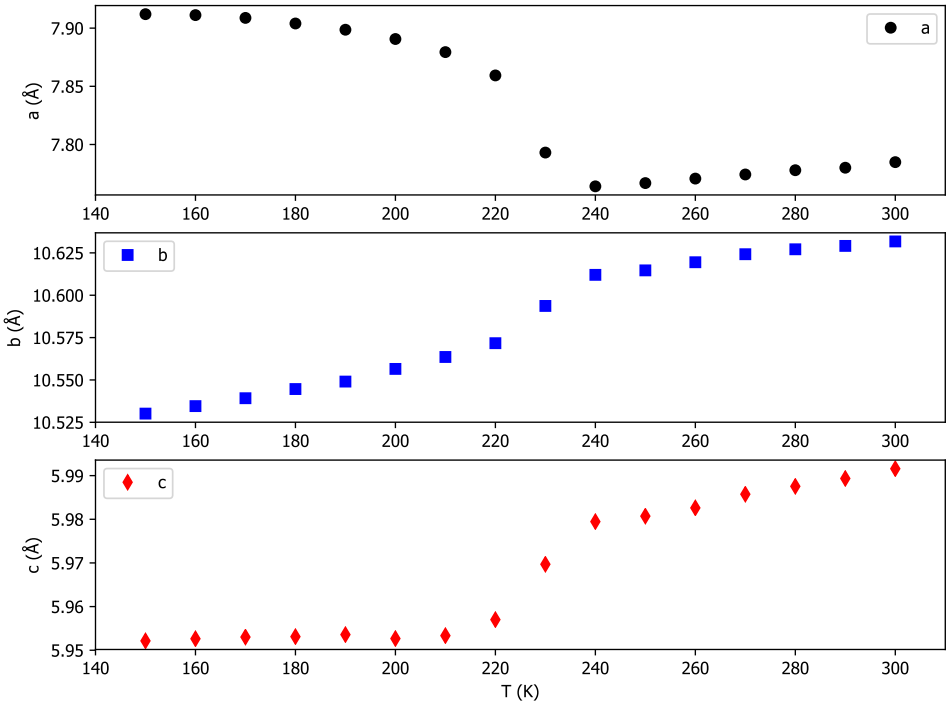


Figure 6.5: Lattice parameters extracted from the Rietveld refinement.

Fig. 6.5 shows the lattice parameters from 150 K to 300 K calculated from the Rietveld refinement. The temperatures can be divided into 3 regions according to the change of lattice parameters of AS. The first region is above 240 K where all lattice parameters show linearly decrease with decreasing temperatures. The second region is between 220 K to 240 K, where the phase transition occurs. All lattice parameters experience abrupt change. Exceptionally, unlike lattice parameter b and c which decrease with decreasing temperatures, the lattice parameter a increases with decreasing temperatures, showing an unusual negative thermal expansion (NTE). The third region is from 150 K to 220 K where the lattice parameter b and c come back to the smooth positive thermal expansion while the NTE behaviour of lattice parameter a persists. The NTE of lattice

parameter a results in the curved increase of unit cell volumes in Fig. 6.3 with decreasing temperatures.

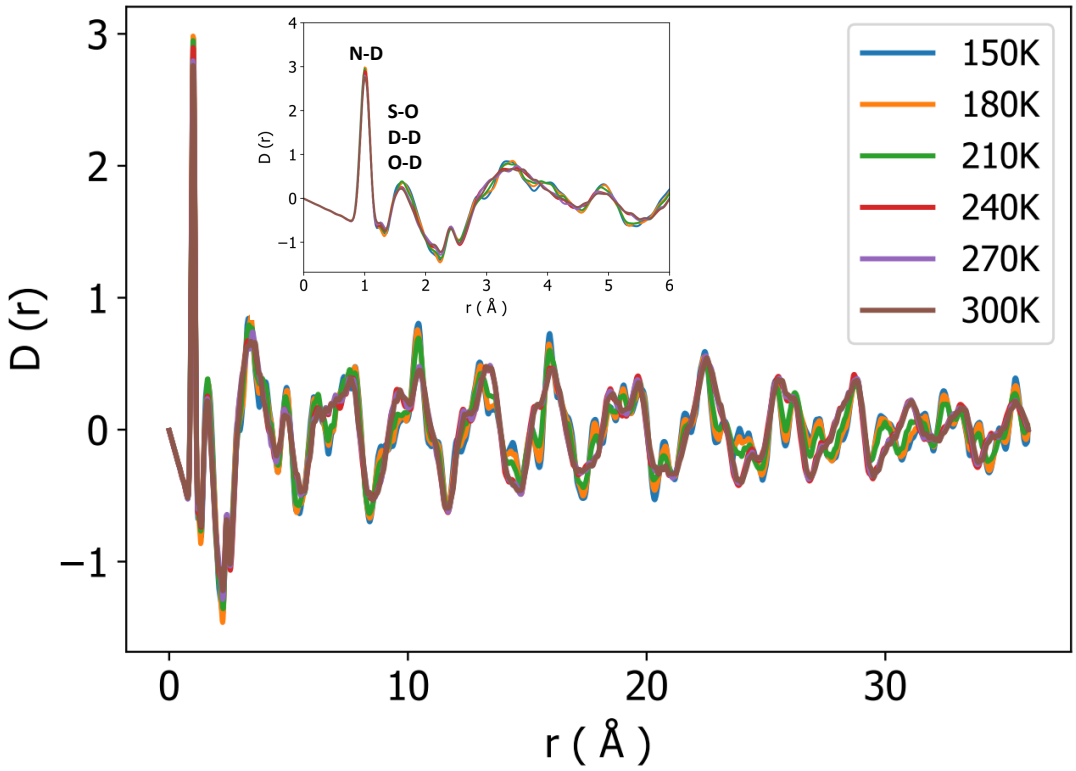


Figure 6.6: Pair distribution functions (PDF) for AS from 150 K to 300 K.

While the LT and the HT phase of AS are hard to identify from Bragg profiles, they can be easily distinguished from the Fourier transform of the total scattering data i.e. the pair distribution functions shown in Fig. 6.6. In the PDFs of AS, the first three peaks are almost identical for both phases, indicating they have similar local structures (the structure within the tetrahedra). However, from the 4th peak, the PDFs of the LT phases show systematic difference with the PDFs of the HT phases, suggesting the tetrahedra (both $ND_4^+$ and $SO_4^{2-}$ ions) are well defined at the short range but behave differently in the LT and the HT phase and result in different medium and long range order.

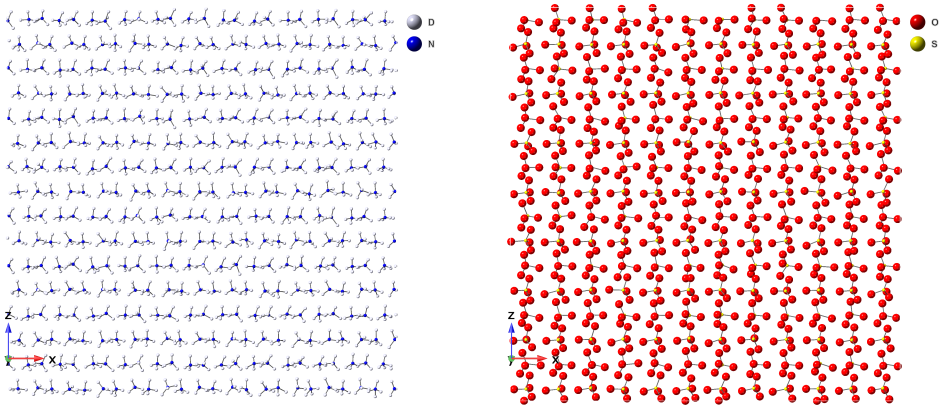


(a) $ND_4^+$ (b) $SO_4^{2-}$

Figure 6.7: Representative atomic layer of a) $ND_4^+$ and b) $SO_4^{2-}$ ions from the 210K RMC configuration viewing from the b axis.

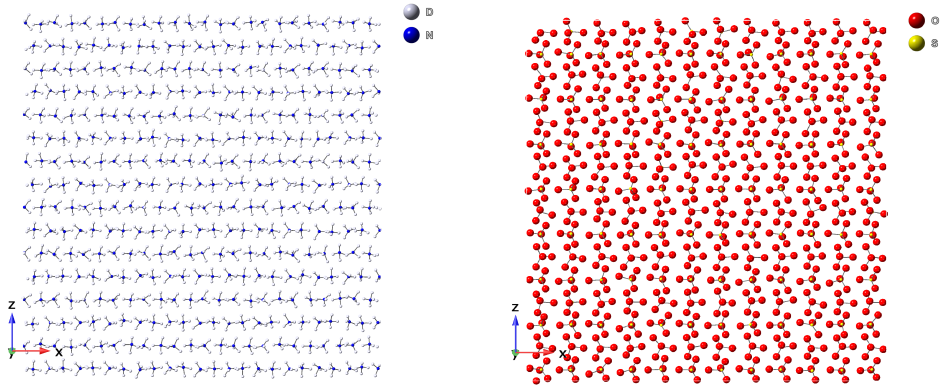


(a) $ND_4^+$ (b) $SO_4^{2-}$

Figure 6.8: Representative atomic layer of a) $ND_4^+$ and b) $SO_4^{2-}$ ions from the 240K RMC configuration viewing from the b axis.

### 6.3.1 RMC configuration analysis

The refined RMC configurations of 210 K (just below the phase transition) and 240 K (just above the phase transition) are shown in Figs. 6.7 and 6.8. It can be seen there is some difference of $ND_4^+$ or $SO_4^{2-}$ ions between the LT and HT phase. However, it is hard to observe how disorder the orientations of $ND_4^+$ or $SO_4^{2-}$ are from direct observation of the RMC configurations.

The orientation distributions of N–D bonds and S–O bonds projected down x axis (corresponding to the right side view of Figs. 6.1, 6.7 and 6.8)are shown in

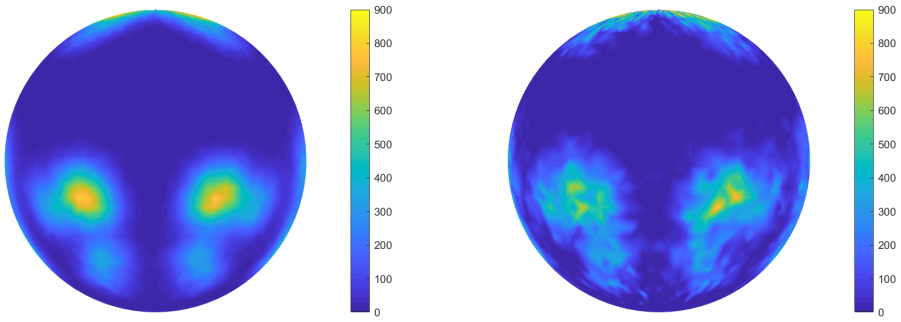


(a) 150 K




(b) 180 K

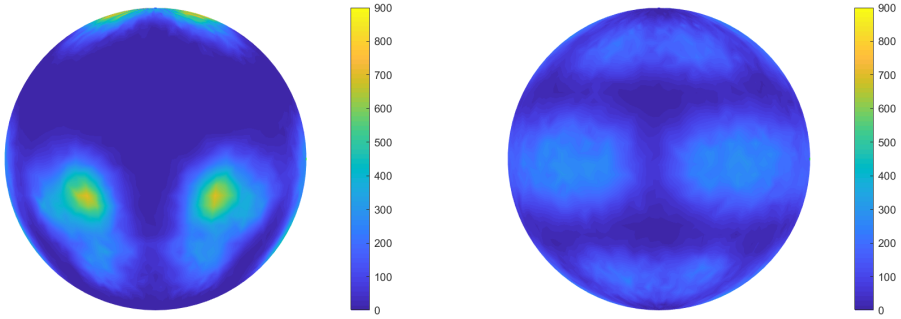


(c) 210 K




(d) 240 K

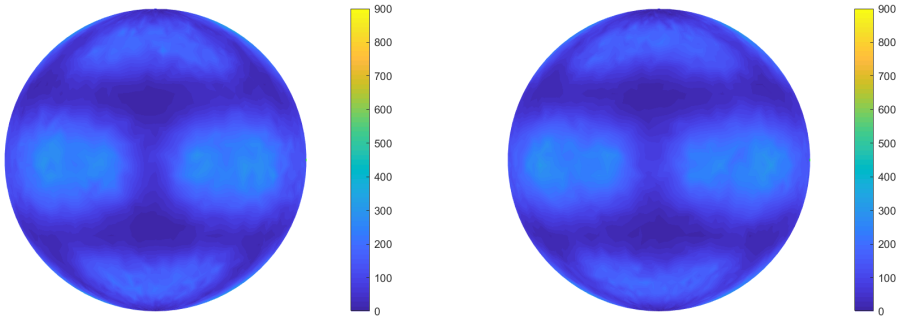


(e) 270 K




(f) 300 K

Figure 6.9: The orientation distribution of N–D bonds projected down the x axis.

Fig. 6.9 and Fig. 6.10 respectively. The orientation distribution projected down the y and z axis are shown in the appendix. In the orientation distributions plot, the brighter the colour, the more bonds orient in the solid angle direction. The bright colour directions in the LT phase become less bright and more widely spread in the HT phase. Hence, what's unclear in the RMC configuration plots (Figs. 6.7 and 6.8) but now clearly shown in the orientation distributions (Fig. 6.9

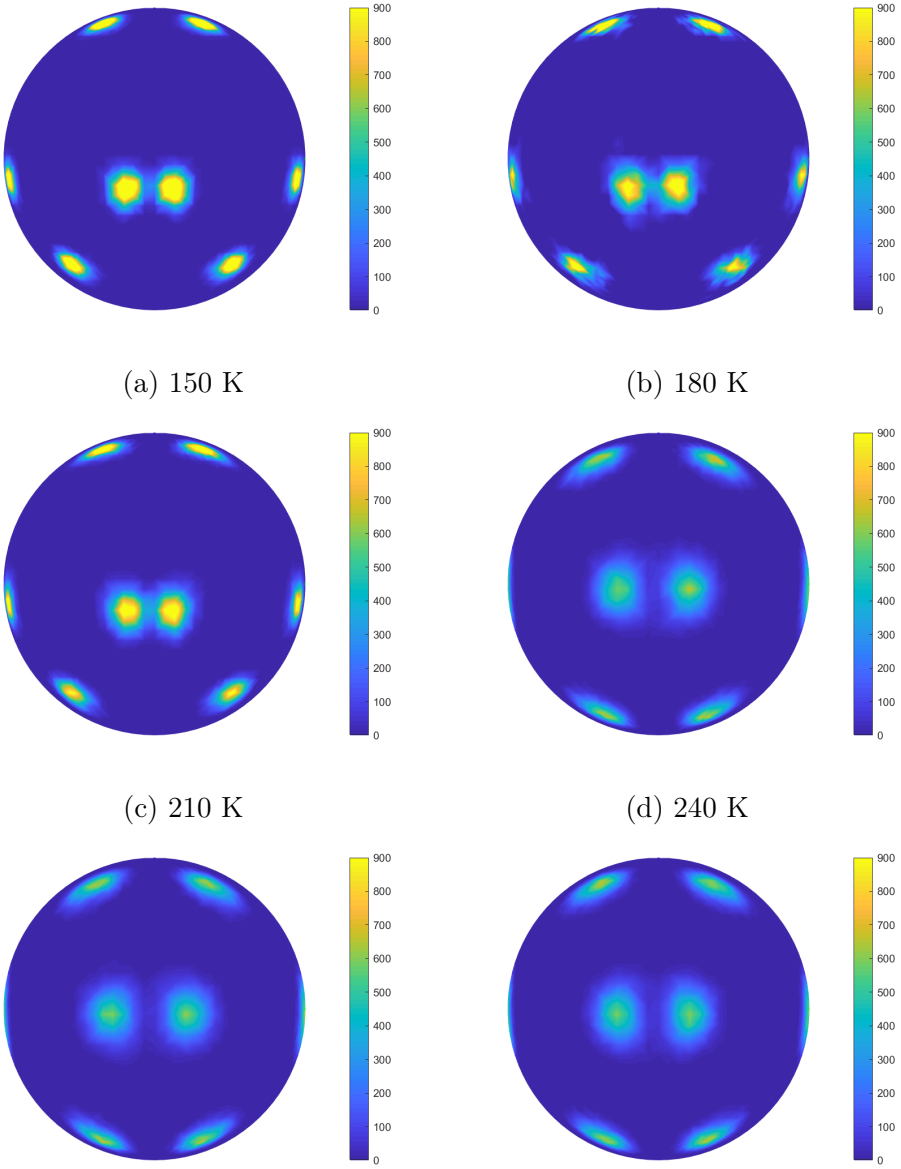


(a) 150 K (b) 180 K

(c) 210 K (d) 240 K

(e) 270 K (f) 300 K

Figure 6.10: The orientation distribution of S–O bonds projected down x axis.

and Fig. 6.10) is that the orientation of both the N–D bonds and S–O bonds become substantially disordered from the LT phase to the HT phase. Moreover, the bonds orientations are symmetrical about the equator section of the sphere (the ab mirror plane in the unit structure) in the HT phase while the bonds orientations become asymmetrical about the equator section of the sphere and slightly tilt down. This is a characterization of the subtle symmetry change shown

in Fig. 6.1. The N–D bonds have a higher tilt amplitude compared with the S–O bonds.

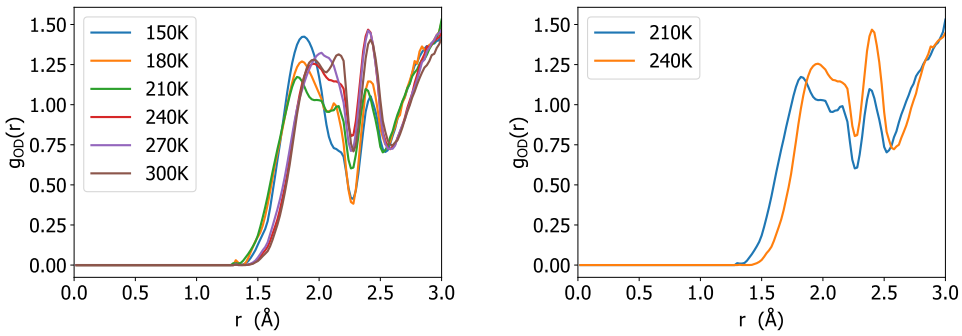


(a) (b)

Figure 6.11: The distribution of O–D partial PDF of a) all temperatures and b) 210 K (just below the phase transition) and 240 K (just above the phase transition).

The O–D partial PDF for all temperatures are shown in Fig. 6.11a, from which it can be seen that the LT and HT phases have fundamentally different hydrogen bonds distributions. In order to show the difference more clearly, Fig. 6.11b only plot the two temperatures just below and above the phase transition i.e. 210 K and 240 K respectively.

Fig. 6.11b shows there are 2 peak regions below 3 Å for both the LT and HT phases. The first peak region represents the hydrogen bonds below 2.3 Å corresponding to the cyan bonds in Fig. 6.1. The second peak region represents the hydrogen bonds between 2.3 Å and 2.7 Åcorresponding to the grey bonds in Fig. 6.1. Because cyan hydrogen bonds are shorter, they are stronger than the grey hydrogen bonds. From the the LT phase to the HT phase, the area under the first peak region decreases from 0.69787 to 0.65325. In the meantime, the second peak region increases from 0.34067 to 0.39200. The peak area change and Fig. 6.11b suggest on one hand the HT phase has much more weaker grey hydrogen bonds than the LT phase. On the other hand, the LT phase has even shorter cyan hydrogen bonds than the HT phase. This suggests the LT phase has

a stronger hydrogen bonds system with more shorter hydrogen bonds whereas the HT phase has a weaker hydrogen bonds system with more longer hydrogen bonds.

### 6.3.2 Polyhedra geometric analysis

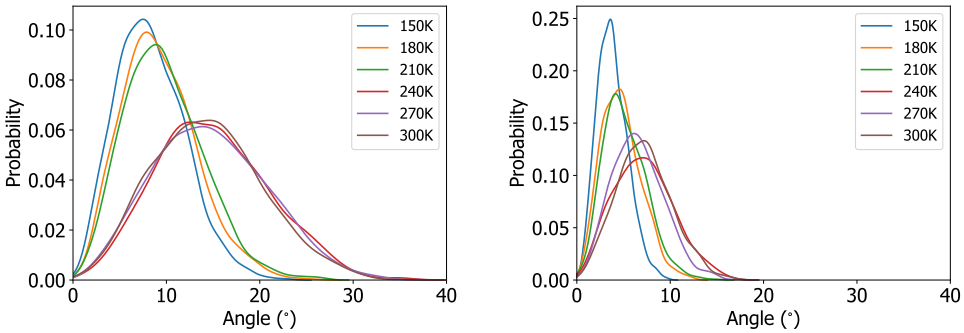


(a) $ND_4^+$ (b) $SO_4^{2-}$

Figure 6.12: The probability distribution of whole body rotation for a) $ND_4^+$ tetrahedra ions and b) $SO_4^{2-}$ tetrahedra ions. The limits of x and y axis are set the same in order to clearly show the comparison of $ND_4^+$ and $SO_4^{2-}$ tetrahedra ions

GASP analysis were performed for both $ND_4^+$ and $SO_4^{2-}$ tetrahedra ions at all 6 temperatures. As explained in Section 2.6.2, each tetrahedron in the RMC configurations is compared to its corresponding crystallographic averaged counterpart. The tetrahedra whole body rotation distributions of $ND_4^+$ and $SO_4^{2-}$ are shown in Fig. 6.12. The $ND_4^+$ tetrahedra change dramatically between the two phases. In the LT phase, the rotation angles are restrained to rotate within 20°. In the HT phase, the rotation angles become much widely distributed and the tail of the rotation angle distribution doubles compared with the LT phase. The average rotation angle of $ND_4^+$ tetrahedra is around 8° in the HT phase whereas the average rotation angle of $ND_4^+$ tetrahedra is around 15°

The rotational behaviour of $SO_4^{2-}$ tetrahedra seems to have 3 stages. At 150 K, the $SO_4^{2-}$ tetrahedra rotation angles are narrowly distributed. Most $SO_4^{2-}$ tetrahedra rotate about 5° and the maximum rotation angle is only 10°. At

180 K and 210 K, the rotation angles of $SO_4^{2-}$ tetrahedra become more widely distributed and the maximum rotation angle is around 15°. When it comes to the HT phase temperatures (240, 270, and 300 K), the rotation angles of $SO_4^{2-}$ tetrahedra become even more widely distributed and the maximum rotation angle achieves 15°. Moreover, the average rotation angle of $ND_4^+$ tetrahedra increases to around 9°. Comparing Fig. 6.12a and Fig. 6.12a, it can be concluded that $ND_4^+$ tetrahedra are more flexible than $SO_4^{2-}$ tetrahedra in terms of rotation.

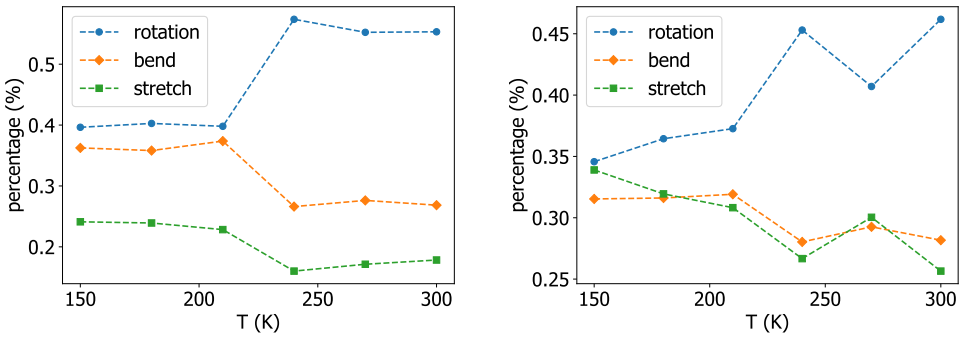


(a) $ND_4^+$ (b) $SO_4^{2-}$

Figure 6.13: The contribution percentage of rotation, bend and stretch in the overall mismatch with the original a) $ND_4^+$ and b) $SO_4^{2-}$ tetrahedra ions.

Fig. 6.13 shows the contribution of whole tetrahedra rotation, bond bending and bond stretching to how each $ND_4^+$ or $SO_4^{2-}$ tetrahedron differs from the ideal crystallography averaged tetrahedra. It's clearly shown that the rotation preserves the highest contribution of tetrahedra mismatch for both phases at all temperatures. Moreover, the rotation contribution has a sharp increase from the LT phase to the HT phase, suggesting in the HT phase, rotation becomes the dominant effect.

For $ND_4^+$ tetrahedra, bond bending has a similar contribution with rotation in the LT phase but its contribution decreased about 10% in the HT phase. Nevertheless, the contribution of bond bend is always 10% higher than that of bond stretch. For $SO_4^{2-}$ tetrahedra, bond bend and bond stretch have similar

Table 6.2: Averaged pseudo-dipole vectors for $ND_4^+$ tetrahedra ions

| Temperature / K | x / Å | y / Å | z / Å |
|---|---|---|---|
| 150 | 0.001(1) | -0.001(1) | 0.038(1) |
| 180 | 0.013(1) | 0.003(1) | 0.045(1) |
| 210 | 0.002(1) | 0.000(1) | 0.042(1) |
| 240 | 0.001(1) | 0.001(1) | 0.002(1) |
| 270 | 0.002(1) | 0.001(1) | 0.001(1) |
| 300 | 0.002(1) | 0.002(1) | 0.000(1) |

Table 6.3: Averaged pseudo-dipole vectors for $SO_4^{2-}$ tetrahedra ions

| Temperature / K | x / Å | y / Å | z / Å |
|---|---|---|---|
| 150 | 0.002(1) | 0.00(1) 1 | -0.123(1) |
| 180 | 0.003(1) | -0.004(1) | -0.132(1) |
| 210 | -0.001(1) | -0.002(1) | -0.128(1) |
| 240 | 0.004(1) | -0.000(2) | -0.000(2) |
| 270 | -0.001(1) | 0.002(2) | 0.001(2) |
| 300 | -0.001(1) | 0.003(2) | 0.003(2) |

tetrahedra mismatch contributions across all temperatures.

### 6.3.3 Pseudo-dipole analysis

The pseudo dipoles for both $ND_4^+$ tetrahedra ions and $SO_4^{2-}$ tetrahedra ions are calculated according to Section 2.6.3. Table 6.2 and Table 6.3 tabulate the averaged pseudo-dipole moment vectors of $ND_4^+$ and $SO_4^{2-}$ tetrahedra respectively. In the LT phase, the averaged z values are at least an order of magnitude larger than both x and y direction (except the x value at 180 K), indicating the pseudo-dipole is strongly biased to the z direction i.e. c axis in the unit cell. In the HT phase, the value magnitudes are more or less the same in all direction. Considering both $ND_4^+$ and $SO_4^{2-}$ tetrahedra ions have charges, this is consistent with the experimental observations that LT AS has spontaneous polarization along c axis whereas HT AS is paraelectric with no spontaneous polarization. In the LT phase, the averaged z values for $SO_4^{2-}$ tetrahedra are about three times bigger than that of $ND_4^+$

Table 6.4: Averaged modulus of the pseudo-dipoles

| Temperature / K | $ND_4^+$ / Å | $SO_4^{2-}$ / Å |
|---|---|---|
| 150 | 0.50(4) | 0.43(3) |
| 180 | 0.51(4) | 0.46(4) |
| 210 | 0.50(4) | 0.46(4) |
| 240 | 0.66(7) | 0.54(5) |
| 270 | 0.66(7) | 0.56(6) |
| 300 | 0.70(8) | 0.56(6) |

tetrahedra. The collective averaged picture is that the $SO_4^{2-}$ tetrahedra are more distorted than $ND_4^+$ tetrahedra with strong bias in the z direction.

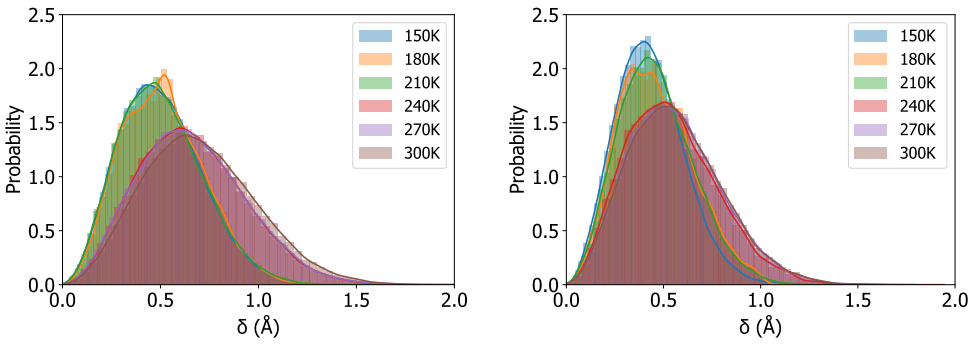


(a) (b)

Figure 6.14: The distributions of the modulus of the pseudo-dipoles for a) $ND_4^+$ and b) $SO_4^{2-}$ tetrahedra ions.

The distributions of the pseudo-dipole modulus for the tetrahedra ions are shown in Fig. 6.14. The modulus of the pseudo-dipole can be treated as a factor to reflect how distorted the tetrahedra are. Like other types of distributions showing above, there is a noteworthy change at the phase transition and again the distributions in the HT phase are much wider than the distributions in the LT phase. The averaged modulus of the pseudo-dipoles is shown in Table 6.4. The averaged pseudo-dipole modulus for $ND_4^+$s increases from 0.5 Å in the LT phase to 0.66 Å in the HT phase. The averaged pseudo-dipole modulus for $SO_4^{2-}$s also increased around 0.1 Å from the LT phase to the HT phase. The averaged pseudo-dipole modulus for $ND_4^+$s is larger than that of $SO_4^{2-}$s, suggesting $ND_4^+$

tetrahedra are more distorted than $SO_4^{2-}$ tetrahedra in both phases.

At the first glimpse, this seems to be contradictory with the conclusion drawn from the averaged pseudo-dipole vectors. Moreover, the modulus of the averaged pseudo-dipole vectors is far more smaller than the averaged pseudo-dipole modulus in the LT phase, especially for $ND_4^+$ tetrahedra. A plausible explanation for this is there is tremendous orientational disorder for the pseudo-dipoles or the directions of tetrahedra distortion of both tetrahedra ions and the $ND_4^+$ tetrahedra are more orientationally disordered than $SO_4^{2-}$ tetrahedra. Therefore, although a $ND_4^+$ tetrahedron is usually more distorted than a $SO_4^{2-}$ tetrahedron, the collective orientation of both tetrahedra result the less orientationally disordered $SO_4^{2-}$ tetrahedra are more distorted than $ND_4^+$ tetrahedra in an overall picture. Both types of tetrahedra in the overall picture are much less distorted than in the individual picture.

## 6.4 Explanation of the phase transition entropy of AS

The RMC study of AS has provided several insights. The plots of orientation distributions of N–D bonds and S–O bonds directly show there is more orientational disorder in the HT phase than in the LT phase. From the O–D partial PDF, it can be concluded that in the LT phase, the shortest hydrogen bonds are even shorter than that in the HT phase. However, there are more longer hydrogen bonds in the HT phase. The gasp analysis indicates the $ND_4^+$ and $SO_4^{2-}$ tetrahedra have much larger rotation amplitudes in the HT phase than in the LT phase. Tetrahedra rotation is the main effect of how tetrahedra ions deviate from their crystallographic ideal form, especially in the HT phase. The pseudo-dipole analysis suggests the $ND_4^+$ and $SO_4^{2-}$ tetrahedra are more distorted in the HT phase than

in the LT phase. $ND_4^+$ tetrahedra are more distorted than $SO_4^{2-}$ tetrahedra in both phases. The modulus of the averaged pseudo-dipole vectors is much more smaller than the averaged pseudo-dipole modulus. It proves both tetrahedra ions experience plenty of orientational disorder from a different aspect.

Taking these insights back to the basic unit cell structure in Fig. 6.1 can give the following story. In the LT phase, the two types tetrahedra network is stabilized by the directionless ionic bonds and directional hydrogen bonds. The orientations of the tetrahedra are arranged in favour of local hydrogen bonds instead of more densely packing of atoms. Nevertheless, the tetrahedra are able to rotate under the constraint of hydrogen bonding. The directional hydrogen bonds will also cause tetrahedra distortion and because the orientation of tetrahedra are ordered, the directional hydrogen bonds may be stronger in certain directions. The electric dipoles induced by the distortion are inclined to orient to the c axis. Thus the spontaneous polarization are created.

As the temperature increases to the HT phase, the tetrahedra can rotate to a point at which some of the connecting hydrogen bonds become symmetrical about the *ab* plane. This creates an equilibrium where the hydrogen bonds at each side of the *ab* mirror plane compete with each other to change the orientation of tetrahedra ions. Thus, the rotation of the tetrahedra increases substantially. The shortest hydrogen bonds (cyan bonds in Fig. 6.1) in the HT phases are those parallel to the *ab* mirror plane. Considering the large reorientation of tetrahedral ions, such hydrogen bonds may only be an imagination from the crystallographic averaged picture and never exist in real situations.

Moreover, the more flexible and less rigid $ND_4^+$ tetrahedra and the less flexible and more rigid $SO_4^{2-}$ tetrahedra form a reorientation competition network. The reorientation of $SO_4^{2-}$ tetrahedra will not only influence the rotation but also distort the neighbouring $ND_4^+$ tetrahedra and vice versa. There will no longer be any preferred orientation along the c axis hence the electric dipoles become

orientationally disordered. The distorted tetrahedra will influence the arrangement of hydrogen bonds and influence back to the orientation of tetrahedra. In short, it's the synergetic effect of tetrahedra rotation, reorganization of hydrogen bonds and tetrahedra distortion hence electric dipole reorientation that make the tetrahedra network become much more disordered and create the giant entropy change.

# Chapter 7

# Conclusions

This thesis is an exploration of using neutron total scattering to study orientational disorder in materials. It includes three previously well studied crystals (potassium cyanide (KCN), barium carbonate ($BaCO_3$) and ammonium sulfate ($(NH_4)_2SO_4$)) and one new amorphous porous aromatic framework material PAF-1. These studies have demonstrated it is a good practice to combine the experimental neutron scattering data with simulation techniques including the reverse Monte Carlo method (RMC) and the molecular dynamics method (MD) to study the orientational disorder in materials.

The orientational disorder of the plastic crystal KCN and the carbonate minerals such as $BaCO_3$ and $CaCO_3$, has been a long-standing problem. Many models have been proposed but these investigations were limited by computational power at the time. With the aid of modern instrumentation and computational power, nowadays it is more feasible to study the orientational disorder quantitatively.

This has been proved from the plastic crystal KCN and common mineral $BaCO_3$ orientational disorder study. The better quantitative understanding of orientational disorder further helps to understand the role of orientational disorder in the phase transition of materials.

In the RMC study of $BaCO_3$, the new multiphase method was used. It demon-

strates the feasibility and potential to study the multiphase materials with RMC.

Ammonium sulfate is an excellent example of how orientational disorder affects the properties of materials. In this case, the orientational disorder of $NH_4$ tetrahedra ions and $SO_4$ tetrahedra ions plays an vital role in the ferroelectric phase transition of AS as well as the associated large phase transition entropy. Understanding this relationship may help to develop new caloric materials with careful choices of basic structure units and use of symmetry.

PAF-1 is an unexpected amorphous framework because it was synthesised aiming at the crystalline diamond framework. Nevertheless, it possesses the high porosity and stability predicted by the crystalline model. The structure of such materials is not easy to study experimentally. The neutron total scattering study confirms the structure of PAF-1 is a continuous random network and possess a characteristic first sharp diffraction peak (FSDP) for tetrahedral networks. This study opens the door for the experimental study of the structure of amorphous tetrahedral networks.

The works included in this thesis provide a method (total scattering + RMC + MD) suitable to study the complex orientational disorder of materials. It is feasible to apply this method to more complicated materials, such as MOFs [7, 174]. In the future, this method can be further developed to accommodate more phases and achieve bigger simulation boxes to cover a longer structure length scale. This will enable studies with more practical considerations. For example, it may allow to experimentally study how the organic molecules behave in water to imitate the cell environment. Perhaps another example which can be practised very soon is to learn how the pollution air molecules interact with framework materials used to absorb them. Once the scientific community accumulated enough reliable studies of the relationship between the orientational disorder and properties of materials, the mechanism hardly to find from a single example may be exploited, perhaps with the aid of deep learning, and that can lead to a more advanced rational

design of materials.

There is no doubt that along with the progress of analysis tools, the potential of combining experimental total scattering data and computer simulations will be more and more exploited for the study of structure-properties relationship of materials.

## Appendix

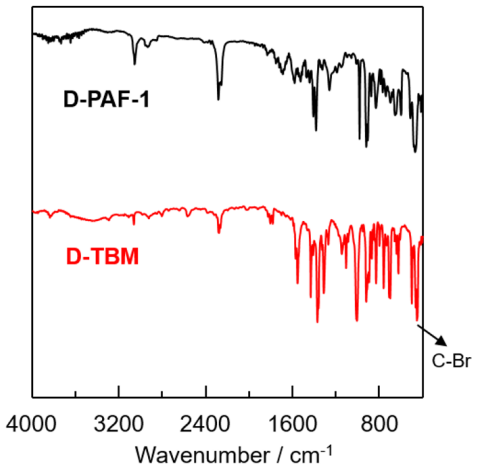


Figure .1: FT-IR spectra of D-PAF-1 (black), and D-TBM (red) from 4000 to 400 $cm^{-1}$. Disappearance of C-Br at 532 $cm^{-1}$ in D-PAF-1 confirm the complete polymerization of D-TBM.

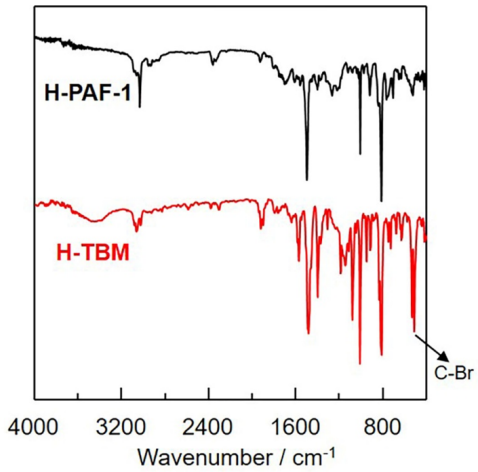


Figure .2: FT-IR spectra of H-PAF-1 (black), and H-TBM (red) from 4000 to 400 $cm^{-1}$. Disappearance of C-Br at 532 $cm^{-1}$ in H-PAF-1 confirm the complete polymerization of H-TBM.

Fig. .9a shows the distribution of N – D bonds remains almost unchanged across all temperatures. The distribution of S – O bonds become wider as the temperature increases but effect is limited. The angle distributions for both D-N-D angle and O-S-O angle become wider along with the increase of temperatures.

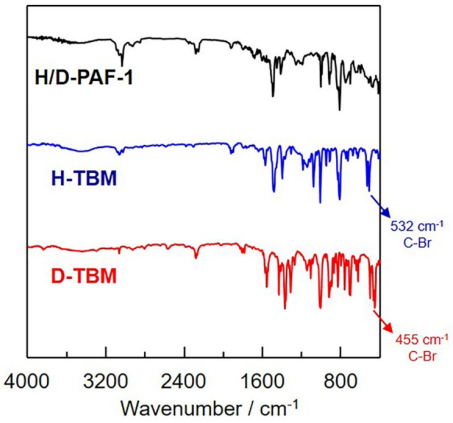


Figure .3: FT-IR spectra of H/D-PAF-1 (black), H-TBM (blue) and D-TBM (red) from 4000 to 400 $cm^{-1}$.

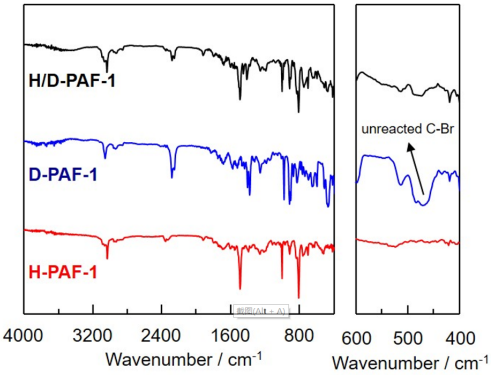


Figure .4: FT-IR spectra of H/D-PAF-1 (black), D-PAF-1 (blue) and H-PAF-1 (red) from 4000 to 400 cm-1 (left) and enlargement spectra from 600 to 400 $cm^{-1}$ (right).

Particularly, all the angle distributions in the HT phase are much wider than angle distributions in the LT phase.

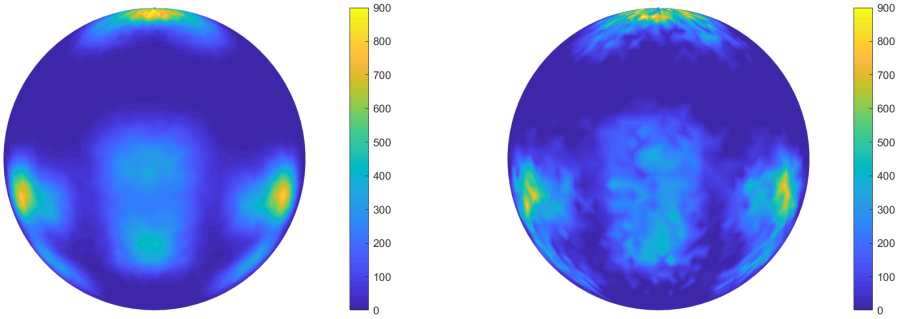


(a) 150 K




(b) 180 K

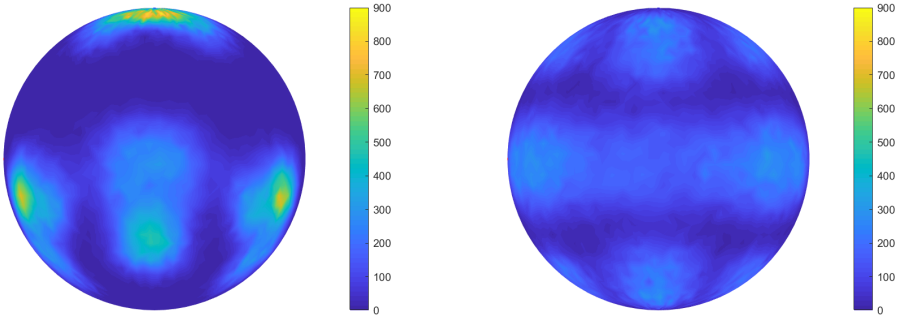


(c) 210 K




(d)

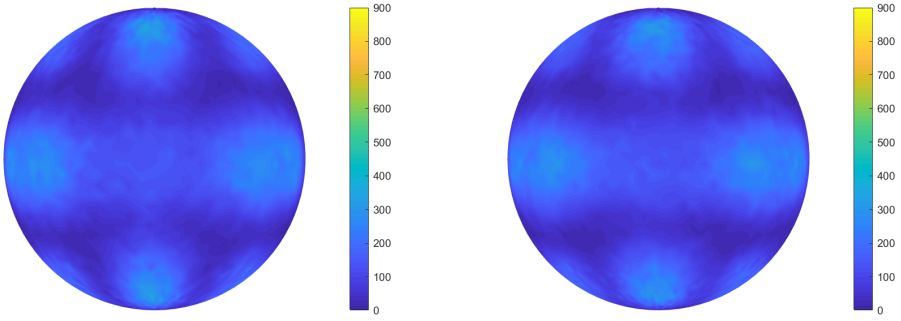


(e) 270 K




(f) 300 K

Figure .5: The orientation distribution of N–D bonds projected down the y axis.

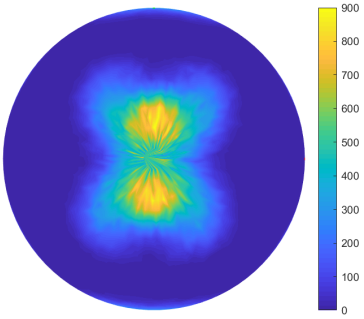


(a) 150 K

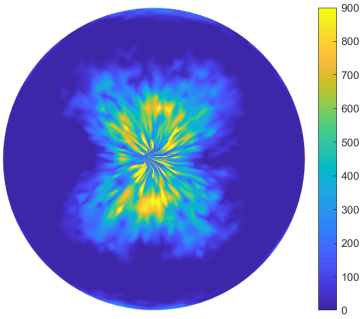


(b) 180 K

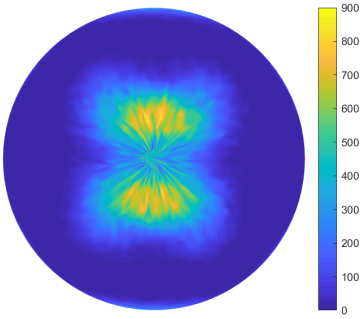


(c) 210 K

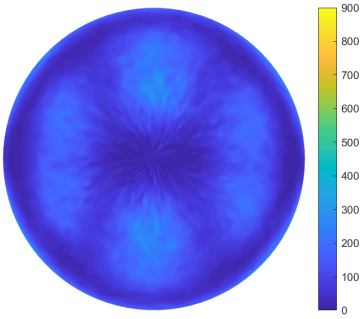


(d)

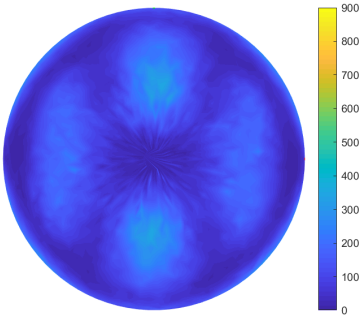


(e) 270 K

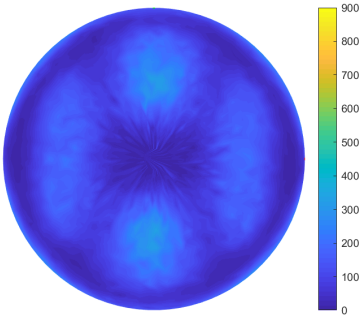


(f) 300 K

Figure .6: The orientation distribution of N–D bonds projected down the z axis.

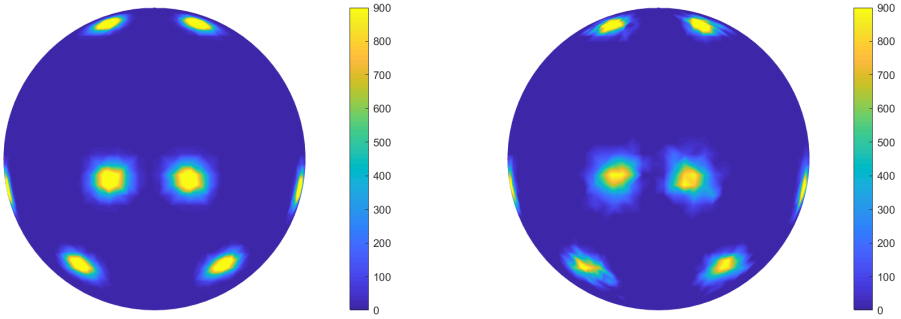


(a) 150 K




(b) 180 K

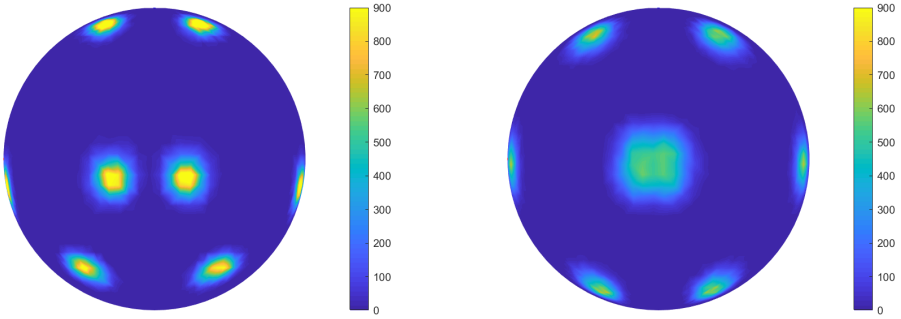


(c) 210 K




(d) 240 K

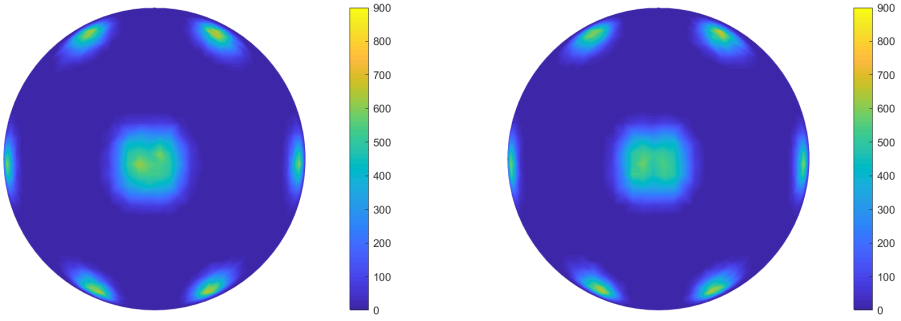


(e) 270 K




(f) 300 K

Figure .7: The orientation distribution of S–O bonds projected down y axis.

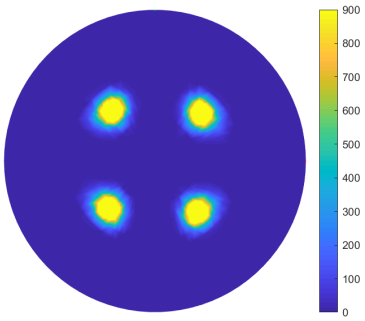


(a) 150 K

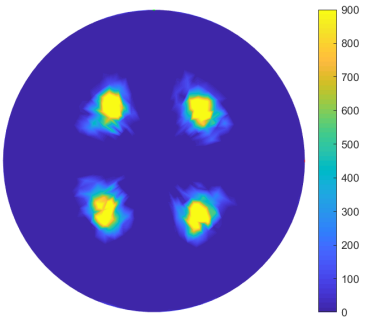


(b) 180 K

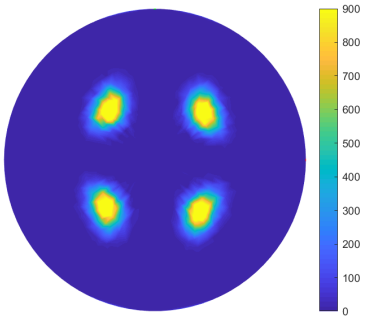


(c) 210 K

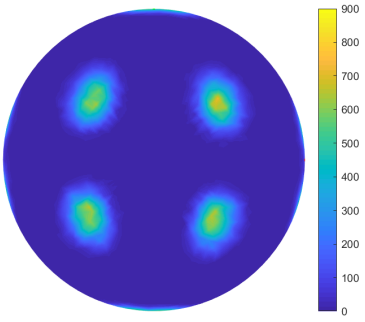


(d) 240 K

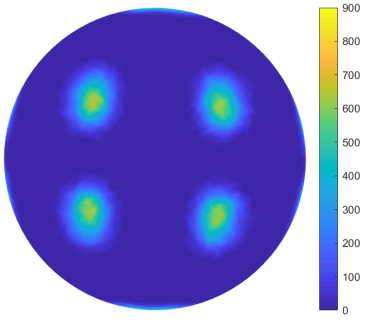


(e) 270 K

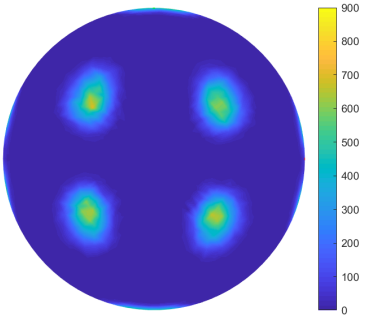


(f) 300 K

Figure .8: The orientation distribution of S–O bonds projected down z axis.

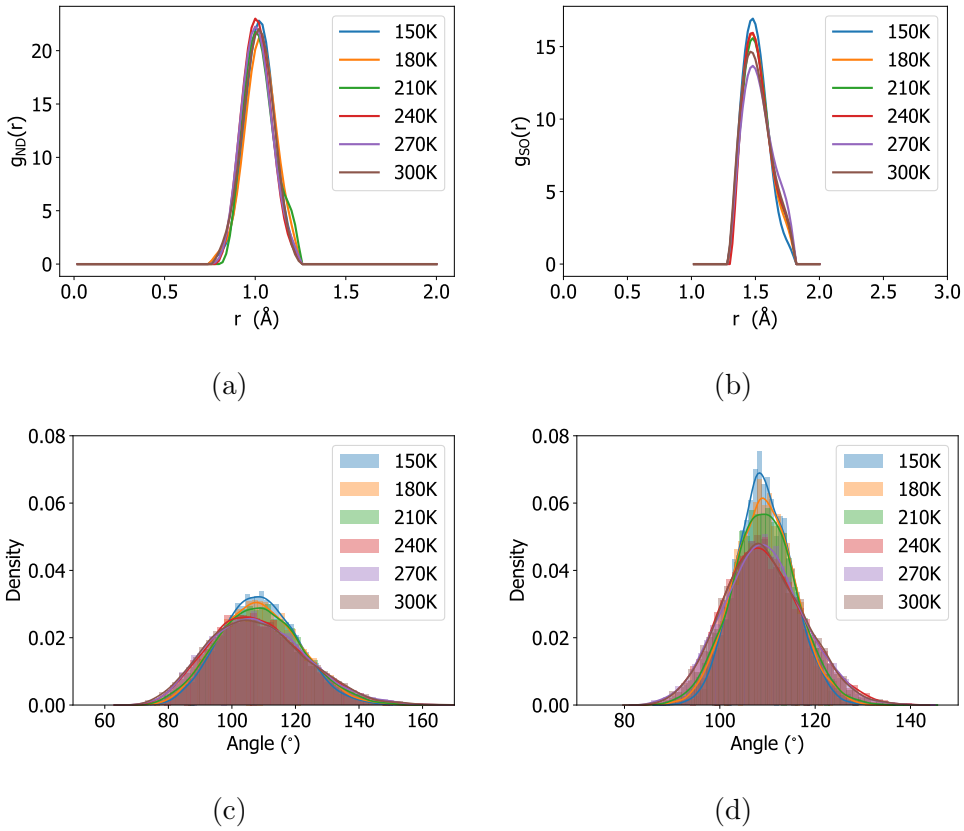


Figure .9: The bond length distribution of a) N–D and b) S–O and the angle distribution of c) D-N-D angle and d) O-S-O angle

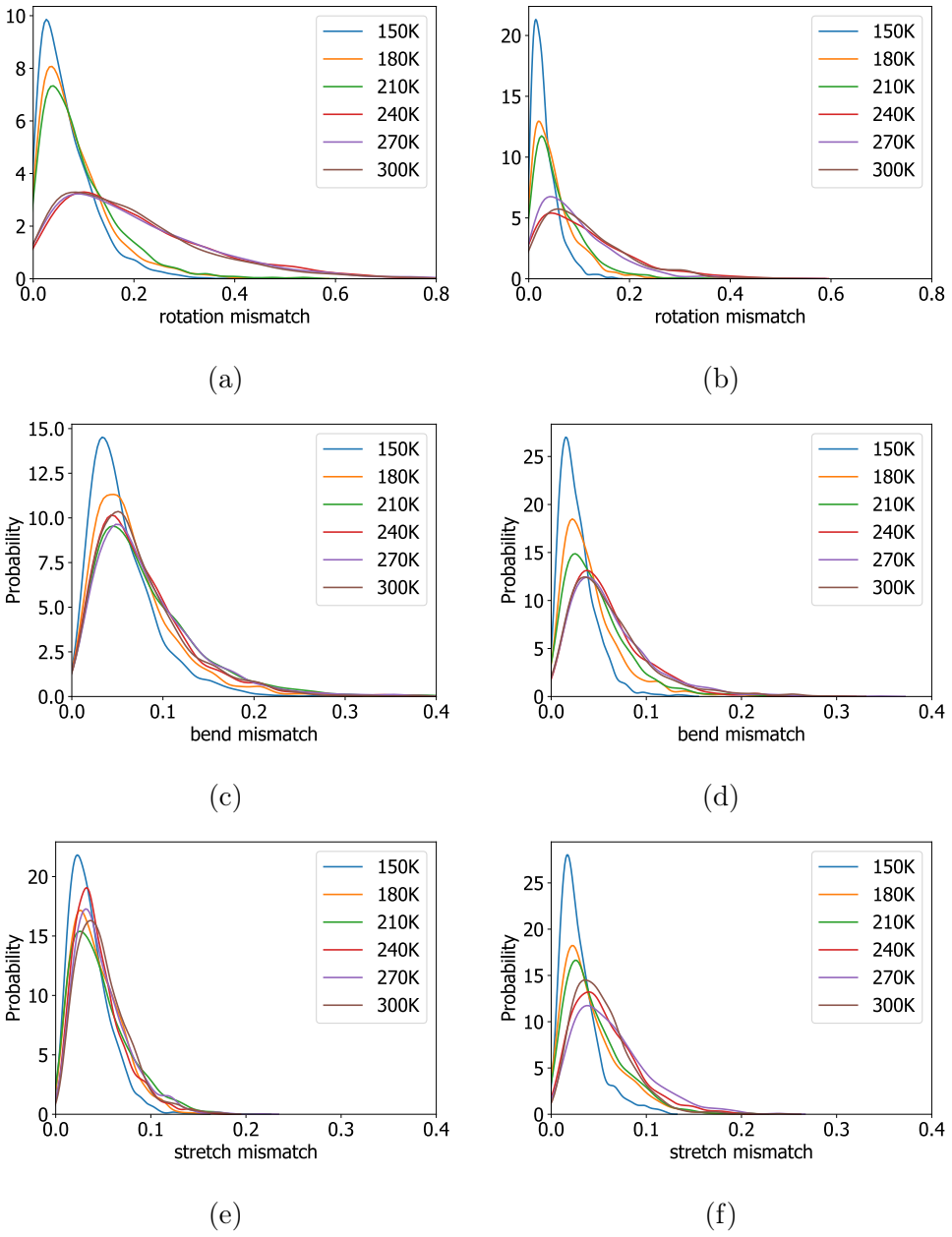


Figure .10: The mismatch distribution of rotation for a) $ND_4^+$ b) $SO_4^{2-}$ , bend for c) $ND_4^+$ d) $SO_4^{2-}$ and stretch for e) $ND_4^+$ f) $SO_4^{2-}$ tetrahedra ions.

# Bibliography

[1]W. K. D. Eisenberg, *The structure and properties of water*, Oxford Classic Texts in the Physical Sciences (Oxford University Press, USA, 2005).

[2]R. W. W. Victor F. Petrenko, *Physics of ice* (Oxford University Press, 2002).

[3]A. Goto, T. Hondoh, and S. Mae, "The electron density distribution in ice i h determined by single-crystal x-ray diffractometry", The Journal of chemical physics **93**, 1412–1417 (1990).

[4]J. M. Ziman, *Models of disorder: the theoretical physics of homogeneously disordered systems* (Cambridge University Press, 1979).

[5]S. Califano, V. Schettino, and N. Neto, *Lattice dynamics of molecular crystals*, Vol. 26 (Springer Science & Business Media, 2012).

[6]G. B. Vaughan, P. A. Heiey, D. E. Luzzi, D. A. Ricketts-Foot, A. R. McGhie, J. E. Fisher, Y.-W. Hui, A. L. Smith, D. E. Cox, W. J. Romanow, et al., "Orientational disorder in solvent-free solid $c_70$", Science **254**, 1350–1353 (1991).

[7]H. D. Duncan, E. O. Beake, H. Y. Playford, M. T. Dove, and A. E. Phillips, "Local structure of a switchable dielectric prussian blue analogue", CrystEngComm **19**, 7316–7321 (2017).

[8]Y. Kanai, A. Harada, T. Shibata, R. Nishimura, K. Namiki, M. Watanabe, S. Nakamura, F. Yumoto, T. Senda, A. Suzuki, et al., "Characterization of heme orientational disorder in a myoglobin reconstituted with a trifluoromethyl-group-substituted heme cofactor", Biochemistry **56**, 4500–4508 (2017).

[9]J. Liu, "Local structure of lead halide perovskites for photovoltaic applications", PhD thesis (School of Physics and Astronomy, Queen Mary university of London, Sept. 2019).

[10]T. Chen, B. J. Foley, B. Ipek, M. Tyagi, J. R. Copley, C. M. Brown, J. J. Choi, and S.-H. Lee, "Rotational dynamics of organic cations in the $ch_3nh_3pbi_3$ perovskite", Physical Chemistry Chemical Physics **17**, 31278–31286 (2015).

[11]J. Even, M. Carignano, and C. Katan, "Molecular disorder and translation/rotation coupling in the plastic crystal phase of hybrid perovskites", Nanoscale **8**, 6222–6236 (2016).

[12]W.-L. Ong, E. S. O'Brien, P. S. Dougherty, D. W. Paley, C. F. Higgs III, A. J. McGaughey, J. A. Malen, and X. Roy, "Orientational order controls crystalline and amorphous thermal transport in superatomic crystals", Nature materials **16**, 83 (2017).

[13]J. Rowe, J. Rush, and E Prince, "Neutron diffraction study of the structure and phase transitions of alkali cyanide crystals", The Journal of Chemical Physics **66**, 5147–5149 (1977).

[14]R. M. Lynden-Bell and K. H. Michel, "Translation-rotation coupling, phase transitions, and elastic phenomena in orientationally disordered crystals", Rev. Mod. Phys. **66**, 721–762 (1994).

[15]W Press and A Hüller, "Analysis of orientationally disordered structures. I. Method", Acta Cryst (1973). A29, 252-256 [doi:10.1107/S0567739473000653], 1–5 (1973).

[16]G Dolling, B. M. Powell, and V. F. Sears, "Neutron diffraction study of the plastic phases of polycrystalline $SF_6$ and $CBr_4$.", English, Molecular Physics **37**, 1859–1883 (1979).

[17]J. Rowe, D. Hinks, D. Price, S Susman, and J. Rush, "Single crystal neutron diffraction study of sodium cyanide", The Journal of Chemical Physics **58**, 2039–2042 (1973).

[18]A Hüller and W Press, "Analysis of orientationally disordered structures. III. Positive definiteness of orientational distribution functions", Acta Crystallographica Section A **35**, 876–880 (1979).

[19]P Gerlach, W Prandl, and K Vogt, "The determination of the effective rotational potential in the plastic phase of $C_2Cl_6$ from neutron Bragg scattering data", English, Molecular Physics **52**, 383–397 (2006).

[20]Y. Xu, B. Gabidullin, and D. L. Bryce, "Single-crystal nmr characterization of halogen bonds", The Journal of Physical Chemistry A **123**, 6194–6209 (2019).

[21]L. W. Jelinski, "Solid state deuterium nmr studies of polymer chain dynamics", Annual Review of Materials Science **15**, 359–377 (1985).

[22]J. R. Yates, S. E. Dobbins, C. J. Pickard, F. Mauri, P. Y. Ghi, and R. K. Harris, "A combined first principles computational and solid-state nmr study of a molecular crystal: flurbiprofen", Physical Chemistry Chemical Physics **7**, 1402–1407 (2005).

[23]C. A. Young and A. L. Goodwin, "Applications of pair distribution function methods to contemporary problems in materials chemistry", Journal of Materials Chemistry **21**, 6464–6476 (2011).

[24]T. Egami and S. J. Billinge, *Underneath the bragg peaks: structural analysis of complex materials*, Vol. 16 (Newnes, 2012).

[25]J. J. Rehr and R. C. Albers, "Theoretical approaches to x-ray absorption fine structure", Rev. Mod. Phys. **72**, 621–654 (2000).

[26]S. A. Maugeri, "Total scattering applied to the study of nanomaterials", PhD thesis (School of Physics and Astronomy, Queen Mary university of London, Aug. 2017).

[27]M. T. Dove, "An introduction to the use of neutron scattering methods in mineral sciences", European Journal of Mineralogy **14**, 203–224 (2002).

[28]M. T. Dove, M. G. Tucker, and D. A. Keen, "Neutron total scattering method: simultaneous determination of long-range and short-range order in disordered materials", European Journal of Mineralogy **14**, 331–348 (2002).

[29]M. T. Dove and M. T. Dove, *Introduction to lattice dynamics*, Vol. 4 (Cambridge university press, 1993).

[30]M. T. Dove and M. T. Dove, *Structure and dynamics: an atomic view of materials*, Vol. 1 (Oxford University Press, 2003).

[31]D. S. Sivia, *Elementary scattering theory: for x-ray and neutron users* (Oxford University Press, 2011).

[32]G. L. Squires, *Introduction to the theory of thermal neutron scattering* (Courier Corporation, 1996).

[33]M. Bée, "Quasielastic neutron scattering", (1988).

[34]G. J. Russell, "Spallation Physics - An Overview", 291–299 (1990).

[35]K. Andersen, *Reactor & Spallation Neutron Sources*, 2013.

[36]P Day, J Enderby, W Williams, L Chapon, A Hannon, P Radaelli, and A Soper, "Scientific reviews: gem: the general materials diffractometer at isis-multibank capabilities for studying crystalline and disordered materials", Neutron News **15**, 19–23 (2004).

[37]D. Bowron, A. Soper, K Jones, S Ansell, S Birch, J Norris, L Perrott, D Riedel, N. Rhodes, S. Wakefield, et al., "Nimrod: the near and intermediate range order diffractometer of the isis second target station", Review of Scientific Instruments **81**, 033905 (2010).

[38]R. Smith, S Hull, M. Tucker, H. Playford, D. McPhail, S. Waller, and S. Norberg, "The upgraded polaris powder diffractometer at the isis neutron source", Review of Scientific Instruments **90**, 115101 (2019).

[39]H. Rietveld, "A profile refinement method for nuclear and magnetic structures", Journal of applied Crystallography **2**, 65–71 (1969).

[40]L. McCusker, R. Von Dreele, D. Cox, D Louër, and P Scardi, "Rietveld refinement guidelines", Journal of Applied Crystallography **32**, 36–50 (1999).

[41]R. Smith, *Refinement of time-of-flight profile parameters in gsas*, `https://www.isis.stfc.ac.uk/Pages/refinement-of-profile-parameters-with-polaris-data.pdf`.

[42]A. Le Bail, "Whole powder pattern decomposition methods and applications: a retrospection", Powder Diffraction **20**, 316–326 (2005).

[43]R. A. Young, *The rietveld method*, Vol. 6 (Oxford university press Oxford, 1993).

[44]A. K. Soper, *GudrunN and GudrunX: programs for correcting raw neutron and X-ray diffraction data to differential scattering cross section*, tech. rep. RAL-TR-2011-013 (Rutherford Appleton Laboratory, Didcot, U.K., 2011).

[45]D. A. Keen, "A comparison of various commonly used correlation functions for describing total scattering.", Journal of Applied Crystallography **34**, 172–177 (2001).

[46]C. Farrow, P Juhas, J. Liu, D Bryndin, E. Božin, J Bloch, T. Proffen, and S. Billinge, "Pdffit2 and pdfgui: computer programs for studying nanostructure in crystals", Journal of Physics: Condensed Matter **19**, 335219 (2007).

[47]H. Lin, E. Božin, S. Billinge, E. Quarez, and M. G. Kanatzidis, "Nanoscale clusters in the high performance thermoelectric agpb$_m$sbte$_{m+2}$", Physical Review B **72**, 174113 (2005).

[48]M. G. Tucker, M. T. Dove, and D. A. Keen, "Application of the reverse monte carlo method to crystalline materials", Journal of applied crystallography **34**, 630–638 (2001).

[49]D. A. Keen, M. G. Tucker, and M. T. Dove, "Reverse Monte Carlo modelling of crystalline disorder", Journal of Physics: Condensed Matter **17**, S15–S22 (2005).

[50]M. T. Dove, M. G. Tucker, and D. A. Keen, "Neutron total scattering method: simultaneous determination of long-range and short-range order in disordered materials.", English, European Journal of Mineralogy **14**, 331–348 (2002).

[51]M. G. Tucker, D. A. Keen, M. T. Dove, A. L. Goodwin, and Q. Hui, "RMCProfile: reverse Monte Carlo for polycrystalline materials.", Journal of Physics: Condensed Matter **19**, 335218–16 (2007).

[52]J. Liu, A. E. Phillips, D. A. Keen, and M. T. Dove, "Thermal disorder and bond anharmonicity in cesium lead iodide studied by neutron total scattering and the reverse monte carlo method", The Journal of Physical Chemistry C (2019).

[53]E. O. Beake, M. G. Tucker, M. T. Dove, and A. E. Phillips, "Orientational disorder in adamantane and adamantanecarboxylic acid", ChemPhysChem **18**, 459–464 (2017).

[54]I. Todorov, W Smith, and U. Cheshire, *The dl poly 4 user manual*, tech. rep. (STFC, STFC Daresbury Laboratory, Daresbury, Warrington, Cheshire, WA4 4AD, United Kingdom, version, 2011).

[55]I. T. Todorov, W. Smith, K. Trachenko, and M. T. Dove, "DL_POLY_3: new dimensions in molecular dynamics simulations via massive parallelism", English, Journal of Materials Chemistry **16**, 1911–8 (2006).

[56]M. Gao, "Carbon dioxide absorption in metal organic frameworks", PhD thesis (School of Physics and Astronomy, Queen Mary university of London, Dec. 2015).

[57]H.-J. Bunge, *Texture analysis in materials science: mathematical methods* (Elsevier, 2013).

[58]G. Cai, A. E. Phillips, D. A. Keen, M. G. Tucker, and M. T. Dove, "Neutron scattering study of the orientational disorder in potassium cyanide", Journal of Physics Communications **4**, 023001 (2020).

[59]G. Cai, A. E. Phillips, M. G. Tucker, and M. T. Dove, "Neutron scattering study of the orientational disorder and phase transitions in barium carbonate", Journal of Physics: Condensed Matter **32** (2020).

[60]C. Bradley and A. Cracknell, *The mathematical theory of symmetry in solids: representation theory for point groups and space groups* (Oxford University Press, 2009).

[61]W. R. Fehlner and S. H. Vosko, "A product representation for cubic harmonics and special directions for the determination of the Fermi surface and related properties", English, Canadian Journal of Physics **54**, 2159–2169 (1976).

[62]S. A. Wells, M. T. Dove, M. G. Tucker, and K. Trachenko, "Real-space rigid-unit-mode analysis of dynamic disorder in quartz, cristobalite and amorphous silica", Journal of Physics: Condensed Matter **14**, 4645 (2002).

[63]R. Lynden-Bell, I. McDonald, and M. Klein, "Analysis of translation-rotation coupling in an orientationally disordered ionic crystal", Molecular Physics **48**, 1093–1117 (1983).

[64]I. E. Collings, A. B. Cairns, A. L. Thompson, J. E. Parker, C. C. Tang, M. G. Tucker, J. Catafesta, C. Levelut, J. Haines, V. Dmitriev, et al., "Homologous critical behavior in the molecular frameworks $zn(cn)_2$ and $cd(imidazolate)_2$", Journal of the American Chemical Society **135**, 7610–7620 (2013).

[65]C. S. Coates, M. Baise, A. Simonov, J. W. Makepeace, A. G. Seel, R. I. Smith, H. Y. Playford, D. A. Keen, R. Siegel, A. Schmutzler, et al., "Room temperature spin-ice physics in cadmium cyanide", arXiv preprint arXiv:1904.05749 (2019).

[66]P. J. W. Debye, *Polar molecules* (Chemical Catalog Company, Incorporated, 1929).

[67]J Frenkel, "The liquid state and the theory of fusion. ii. the theory of fusion and crystallization", Acta phys.-chim. URSS **3**, 913–938 (1935).

[68]H. T. Stokes, D. L. Decker, H. M. Nelson, and J. Jorgensen, "Structure of potassium cyanide at low temperature and high pressure determined by neutron diffraction", Physical Review B **47**, 11082 (1993).

[69]D. Price, J. Rowe, J. Rush, E Prince, D. Hinks, and S Susman, "Single crystal neutron diffraction study of potassium cyanide", The Journal of Chemical Physics **56**, 3697–3702 (1972).

[70]R. W. Impey, M. Sprik, and M. L. Klein, "Simulation of the cubic to orthorhombic phase transition in potassium cyanide", The Journal of chemical physics **83**, 3638–3644 (1985).

[71]K. H. Michel and H De Raedt, "Unified rotational dynamics of molecular crystals with orientational phase transition", English, The Journal of Chemical Physics **65**, 977–984 (1976).

[72]K. H. Michel and J Naudts, "Anomalous thermoelastic behavior and molecular reorientations in crystals", English, The Journal of Chemical Physics **67**, 547–558 (1977).

[73]K. H. Michel and J Naudts, "Dynamics of translations and rotations in molecular crystals", English, The Journal of Chemical Physics **68**, 216–14 (1978).

[74]J. M. Rowe, J. J. Rush, N. J. Chesser, K. H. Michel, and J Naudts, "Nature of the Phase Transition in KCN at 168 K", English, Physical Review Letters **40**, 455–458 (1978).

[75]R. M. Sharma and T. P. Sharma, "Lattice dynamics of KCN", English, Journal of Physics C: Solid State Physics **20**, 3411–3416 (1987).

[76]D. Durand, L. C. S. do Carmo, A. Anderson, and F. Lüty, "Raman and infrared studies of rotational-translational modes in stress-aligned ferroelastic kcn and nacn", Physical Review B **22**, 4005 (1980).

[77]M. T. Dove and G. Rigg, "RMCgui: a new interface for the workflow associated with running Reverse Monte Carlo simulations", English, Journal of Physics: Condensed Matter **25**, 454222–9 (2013).

[78]R Srinivasan, "The thermal expansion of calcite from room temperature up to 400°C", English, Proceedings of the Indian Academy of Sciences - Section A **42**, 81–85 (1955).

[79]S. A. Markgraf and R. J. Reeder, "High-temperature structure refinements of calcite and magnesite", American Mineralogist **70**, 590–600 (1985).

[80]M. T. Dove and B. M. Powell, "Neutron diffraction study of the tricritical orientational order/disorder phase transition in calcite at 1260 K", English, Physics and Chemistry of Minerals **16**, 1–5 (1989).

[81]M. T. Dove, I. P. Swainson, B. M. Powell, and D. C. Tennant, "Neutron powder diffraction study of the orientational order–disorder phase transition in calcite, $CaCO_3$", English, Physics and Chemistry of Minerals **32**, 493–503 (2005).

[82]J. P. R. de Villiers, "Crystal structures of aragonite, strontianite, and witherite", American Mineralogist **56**, 758–767 (1971).

[83]S. M. Antao and I. Hassan, "$BaCO_3$: high-temperature crystal structures and the $Pmcn \rightarrow R3m$ phase transition at 811 °C", English, Physics and Chemistry of Minerals **34**, 573–580 (2007).

[84]S. M. Antao and I Hassan, "The orthorhombic structure of $CaCO_3$, $SrCO_3$, $PbCO_3$ and $BaCO_3$: linear structural trends", English, The Canadian Mineralogist **47**, 1245–1255 (2009).

[85]Y Ye, J. R. Smyth, and P Boni, "Crystal structure and thermal expansion of aragonite-group carbonates by single-crystal x-ray diffraction", American Mineralogist **97**, 707–712 (2012).

[86]K. O. Strömme, "On the crystal structures of the high-temperature forms of strontium and barium carbonate and structurally related compounds", English, Acta Chemica Scandinavica **29a**, 105–110 (1975).

[87]T. D. Archer, S. E. A. Birse, M. T. Dove, S. A. T. Redfern, J. D. Gale, and R. T. Cygan, "An interatomic potential model for carbonates allowing for polarization effects", English, Physics and Chemistry of Minerals **30**, 416–424 (2003).

[88]P. Raiteri, J. D. Gale, D. Quigley, and P. M. Rodger, "Derivation of an Accurate Force-Field for Simulating the Growth of Calcium Carbonate from Aqueous Solution: A New Model for the Calcite–Water Interface", The Journal of Physical Chemistry C **114**, 5997–6010 (2010).

[89]M Parrinello and A Rahman, "Crystal Structure and Pair Potentials: A Molecular-Dynamics Study", English, Physical Review Letters **45**, 1196–1199 (1980).

[90]S. Melchionna, G. Ciccotti, and B. Lee Holian, "Hoover NPTdynamics for systems varying in shape and size", English, Molecular Physics **78**, 533–544 (2006).

[91]S. Nosé, "A unified formulation of the constant temperature molecular dynamics methods", English, The Journal of Chemical Physics **81**, 511–10 (1984).

[92]W. G. Hoover, "Canonical dynamics: Equilibrium phase-space distributions", English, Physical Review A **31**, 1695–1697 (1985).

[93]A. C. Hannon, "Results on disordered materials from the GEneral Materials diffractometer, GEM, at ISIS", English, Nuclear Instruments and Methods in Physics Research Section A: Accelerators, Spectrometers, Detectors and Associated Equipment **551**, 88–107 (2005).

[94]O Arnold, J. C. Bilheux, J. M. Borreguero, A Buts, S. I. Campbell, L Chapon, M Doucet, N Draper, R. F. Leal, M. A. Gigg, V. E. Lynch, A Markvardsen, D. J. Mikkelson, R. L. Mikkelson, R Miller, K Palmen, P Parker, G Passos, T. G. Perring, P. F. Peterson, S Ren, M. A. Reuter, A. T. Savici, J. W. Taylor, R. J. Taylor, R Tolchenov, W Zhou, and J Zikovsky, "Mantid—Data analysis and visualization package for neutron scattering and $\mu$ SR experiments", Nuclear Inst. and Methods in Physics Research, A **764**, 156–166 (2014).

[95]A. K. Soper, *GudrunN and GudrunX : programs for correcting raw neutron and X-ray diffraction data to differential scattering cross section*, tech. rep. RAL-TR-2011-013 (Rutherford Appleton Laboratory, 2011).

[96]A. C. Larson and R. B. Von Dreele, *General Structure Analysis System (GSAS)*, tech. rep. LAUR 86-748 (Los Alamos National Laboratory, 2004).

[97]B. H. Toby, "EXPGUI, a graphical user interface for GSAS", Journal of Applied Crystallography **34**, 210–213 (2001).

[98]B. H. Toby and R. B. Von Dreele, "GSAS-II: the genesis of a modern open-source all purpose crystallography software package", English, Journal of Applied Crystallography **46**, 544–549 (2013).

[99]W. A. Sławiński, "Calculation of pair distribution functions for multiphase systems", English, Journal of Applied Crystallography **51**, 919–923 (2018).

[100]O. M. Yaghi, M. O'Keeffe, N. W. Ockwig, H. K. Chae, M. Eddaoudi, and J. Kim, "Reticular synthesis and the design of new materials", Nature **423**, 705–714 (2003).

[101]W. W. Schmahl, I. P. Swainson, M. T. Dove, and A Graeme-Barber, "Landau free energy and order parameter behaviour of the $\alpha/\beta$ phase transition in cristobalite.", Zeitschrift für Kristallographie **201**, 125–145 (1992).

[102]M. G. Tucker, M. P. Squires, M. T. Dove, and D. A. Keen, "Dynamic structural disorder in cristobalite: neutron total scattering measurement and reverse Monte Carlo modelling.", Journal of Physics: Condensed Matter **13**, 403–423 (2000).

[103]A. L. Goodwin and C. Kepert, "Negative thermal expansion and low-frequency modes in cyanide-bridged framework materials.", Physical Review B **71**, 140301 (2005).

[104]W Schafer and A Kirfel, "Neutron powder diffraction study of the thermal expansion of cuprite.", Applied Physics A: Materials Science & Processing **74**, S1010–S1012 (2002).

[105]G. Artioli, M. Dapiaggi, P. Fornasini, A. Sanson, F. Rocca, and M. Merli, "Negative thermal expansion in cuprite-type compounds: A combined synchrotron XRPD, EXAFS, and computational study of $Cu_2O$ and $Ag_2O$.", Journal of Physics and Chemistry of Solids **67**, 1918–1922 (2006).

[106]L. Li, K. Refson, and M. T. Dove, "Negative thermal expansion of cubic silicon dicarbodiimide, $Si(NCN)_2$, studied by ab initiolattice dynamics", Journal of Physics: Condensed Matter **32**, 465402–11 (2020).

[107]K. S. Park, Z Ni, A. P. Cote, J. Y. Choi, R Huang, F. J. Uribe-Romo, H. K. Chae, M O'Keeffe, and O. M. Yaghi, "Exceptional chemical and thermal stability of zeolitic imidazolate frameworks.", Proceedings of the National Academy of Sciences **103**, 10186–10191 (2006).

[108]W. H. Zachariasen, "The atomic arrangement in glass", Journal of the American Chemical Society **54**, 3841–3851 (1932).

[109]P Steinhardt, R Alben, and D Weaire, "Relaxed continuous random network models", Journal of Non-Crystalline Solids **15**, 199–214 (1974).

[110]Y. Tu, J Tersoff, G Grinstein, and D. Vanderbilt, "Properties of a Continuous-Random-Network Model for Amorphous Systems", Physical Review Letters **81**, 4899–4902 (1998).

[111]G. T. Barkema and N. Mousseau, "High-quality continuous random networks", Physical Review B **62**, 4985–4990 (2000).

[112]K. Laaziri, S Kycia, S Roorda, M Chicoine, J. L. Robertson, J Wang, and S. C. Moss, "High-energy x-ray diffraction study of pure amorphous silicon", Physical Review B **60**, 13520–13533 (1999).

[113]M. J. Cliffe, A. P. Bartók, R. N. Kerber, C. P. Grey, G. Csányi, and A. L. Goodwin, "Structural simplicity as a restraint on the structure of amorphous silicon", Physical Review B **95**, 224108–6 (2017).

[114]A. C. Wright, "Neutron scattering from vitreous silica. V. The structure of vitreous silica: What have we learned from 60 years of diffraction studies?", Journal of Non-Crystalline Solids **179**, 84–115 (1994).

[115]M. G. Tucker, D. A. Keen, M. T. Dove, and K Trachenko, "Refinement of the Si–O–Si bond angle distribution in vitreous silica", Journal of Physics: Condensed Matter **17**, S67–S75 (2005).

[116]A. C. Wright, "Silicate glass structure: towards a working hypothesis for the 21st century", Physics and Chemistry of Glasses **61**, 57–76 (2020).

[117]T. D. Bennett, A. L. Goodwin, M. T. Dove, D. A. Keen, M. G. Tucker, E. R. Barney, A. K. Soper, E. G. Bithell, J.-C. Tan, and A. K. Cheetham, "Structure and properties of an amorphous metal-organic framework", Physical review letters **104**, 115503 (2010).

[118]M. T. McDowell, S. W. Lee, J. T. Harris, B. A. Korgel, C. Wang, W. D. Nix, and Y. Cui, "In situ tem of two-phase lithiation of amorphous silicon nanospheres", Nano letters **13**, 758–764 (2013).

[119]T. Ben, H. Ren, S. Ma, D. Cao, J. Lan, X. Jing, W. Wang, J. Xu, F. Deng, J. M. Simmons, S. Qiu, and G. Zhu, "Targeted Synthesis of a Porous Aromatic Framework with High Stability and Exceptionally High Surface Area", Angewandte Chemie International Edition **48**, 9457–9460 (2009).

[120]C. Pei, T. Ben, and S. Qiu, "Great Prospects for PAF-1 and its derivatives", Mater. Horiz. **2**, 11–21 (2015).

[121]O. M. Yaghi, G. Li, and H. Li, "Selective binding and removal of guests in a microporous metal-organic framework", Nature **378**, 703–706 (1995).

[122]H.-C. J. Zhou and S. Kitagawa, "Metal–Organic Frameworks (MOFs)", Chem. Soc. Rev. **43**, 5415–5418 (2014).

[123]A. P. Cote, "Porous, Crystalline, Covalent Organic Frameworks", Science **310**, 1166–1170 (2005).

[124]S.-Y. Ding and W. Wang, "Covalent organic frameworks (cofs): from design to applications", Chemical Society Reviews **42**, 548–568 (2013).

[125]P. M. Budd, B. S. Ghanem, S. Makhseed, N. B. McKeown, K. J. Msayib, and C. E. Tattershall, "Polymers of intrinsic microporosity (PIMs): robust, solution-processable, organic nanoporous materials", Chemical Communications, 230–2 (2004).

[126]J.-X. Jiang, F. Su, A. Trewin, C. D. Wood, N. L. Campbell, H. Niu, C. Dickinson, A. Y. Ganin, M. J. Rosseinsky, Y. Z. Khimyak, and A. I. Cooper, "Conjugated Microporous Poly(aryleneethynylene) Networks", Angewandte Chemie International Edition **46**, 8574–8578 (2007).

[127]S. S. Han, H. Furukawa, O. M. Yaghi, and W. A. Goddard Iii, "Covalent organic frameworks as exceptional hydrogen storage materials", Journal of the American Chemical Society **130**, 11580–11581 (2008).

[128]J. S. Jian-Rong Li and H.-C. Zhou, "Metal–Organic Frameworks for Separations", Chemical Reviews, 1–64 (2012).

[129]S. M. J. Rogge, A Bavykina, J Hajek, H Garcia, A. I. Olivos-Suarez, A Sepúlveda-Escribano, A Vimont, G Clet, P Bazin, F Kapteijn, M Daturi, E. V. Ramos-Fernandez, F. X. Llabrés i Xamena, V Van Speybroeck, and J Gascon, "Metal–organic and covalent organic frameworks as single-site catalysts", Chem. Soc. Rev. **46**, 3134–3184 (2017).

[130]S. Das, P. Heasman, T. Ben, and S. Qiu, "Porous organic materials: strategic design and structure–function correlation", Chemical reviews **117**, 1515–1563 (2017).

[131]T. Ben and S. Qiu, "Porous aromatic frameworks: synthesis, structure and functions", CrystEngComm **15**, 17–26 (2013).

[132]A. B. Cairns and A. L. Goodwin, "Structural disorder in molecular framework materials", Chemical Society Reviews **42**, 4881–4893 (2013).

[133]A. Trewin and A. I. Cooper, "Porous organic polymers: distinction from disorder?", Angewandte Chemie International Edition **49**, 1533–1535 (2010).

[134]J. M. H. Thomas and A. Trewin, "Amorphous PAF-1: Guiding the Rational Design of Ultraporous Materials", The Journal of Physical Chemistry C **118**, 19712–19722 (2014).

[135]P. Fayon and A. Trewin, "Formation mechanism of ultra porous framework materials", Physical Chemistry Chemical Physics **18**, 16840–16847 (2016).

[136]D. T. Bowron, A. K. Soper, K Jones, S Ansell, S Birch, J Norris, L Perrott, D Riedel, N. J. Rhodes, S. R. Wakefield, A Botti, M. A. Ricci, F Grazzi, and M Zoppi, "NIMROD: The Near and InterMediate Range Order Diffractometer of the ISIS second target station", Review of Scientific Instruments **81**, 033905–11 (2010).

[137]Y. Ke, C. He, H. Zheng, Y. Geng, J. Fu, S. Zhang, H. Hu, S. Wang, B. Zhou, F. Wang, and J. Tao, "The time-of-flight Small-Angle Neutron Spectrometer at China Spallation Neutron Source", Neutron News **29**, 14–17 (2018).

[138]F Wooten, K Winer, and D Weaire, "Computer Generation of Structural Models of Amorphous Si and Ge", Physical Review Letters **54**, 1392–1395 (1985).

[139]D. C. Palmer, "Visualization and analysis of crystal structures using CrystalMaker software", Zeitschrift für Kristallographie - Crystalline Materials **230**, 559–572 (2015).

[140]D. E. Williams, "Improved intermolecular force field for molecules containing H, C, N, and O atoms, with application to nucleoside and peptide crystals", Journal of Computational Chemistry **22**, 1154–1166 (2001).

[141]N. L. Allinger, Y. H. Yuh, and J. H. Lii, "Molecular mechanics. The MM3 force field for hydrocarbons. 1.", Journal of the American Chemical Society **111**, 8551–8566 (1989).

[142]M. P. Johansson and J. Olsen, "Torsional Barriers and Equilibrium Angle of Biphenyl: Reconciling Theory with Experiment", Journal of Chemical Theory and Computation **4**, 1460–1471 (2008).

[143]V. F. Sears, "Neutron scattering lengths and cross sections", Neutron News **3**, 26–37 (1992).

[144]S Ciccariello, J Goodisman, and H Brumberger, "On the Porod law", Journal of Applied Crystallography **21**, 117–128 (1988).

[145]D. A. Keen and M. T. Dove, "Local structures of amorphous and crystalline phases of silica, $SiO_2$, by neutron total scattering", Journal of Physics: Condensed Matter **11**, 9263–9273 (1999).

[146]P. S. Salmon, "Real Space Manifestation of the First Sharp Diffraction Peak in the Structure Factor of Liquid and Glassy Materials", Proceedings of the Royal Society A: Mathematical, Physical and Engineering Sciences **445**, 351–365 (1994).

[147]S. R. Elliott, "The origin of the first sharp diffraction peak in the structure factor of covalent glasses and liquids", Journal of Physics: Condensed Matter **4**, 7661–7678 (1999).

[148]C. Massobrio and A. Pasquarello, "Origin of the first sharp diffraction peak in the structure factor of disordered network-forming systems: Layers or voids?", The Journal of Chemical Physics **114**, 7976–7979 (2001).

[149]J. Du and L. R. Corrales, "First sharp diffraction peak in silicate glasses: Structure and scattering length dependence", Physical Review B **72**, 239–4 (2005).

[150]G. Lucovsky and J. C. Phillips, "Nano-regime Length Scales Extracted from the First Sharp Diffraction Peak in Non-crystalline SiO2 and Related Materials: Device Applications", Nanoscale Research Letters **5**, 550–558 (2010).

[151]M. Micoulaut and M. Bauchy, "Anomalies of the first sharp diffraction peak in network glasses: Evidence for correlations with dynamic and rigidity properties", Physica Status Solidi b **250**, 976–982 (2013).

[152]M. T. M. Shatnawi, "The First Sharp Diffraction Peak in the Total Structure Function of Amorphous Chalcogenide Glasses: Anomalous Characteristics and Controversial Views", New Journal of Glass and Ceramics **06**, 37–46 (2016).

[153]Y. Shi, J. Neuefeind, D. Ma, K. Page, L. A. Lamberson, N. J. Smith, A. Tandia, and A. P. Song, "Ring size distribution in silicate glasses revealed by neutron scattering first sharp diffraction peak analysis", Journal of Non-Crystalline Solids **516**, 71–81 (2019).

[154]R. Shi and H. Tanaka, "Distinct signature of local tetrahedral ordering in the scattering function of covalent liquids and glasses", Science Advances **5**, eaav3194–7 (2019).

[155]M. T. Dove and H. Fang, "Negative thermal expansion and associated anomalous physical properties: review of the lattice dynamics theoretical foundation", Reports on Progress in Physics **79**, 066503 (2016).

[156]B. Matthias and J. Remeika, "Ferroelectricity in ammonium sulfate", Physical Review **103**, 262 (1956).

[157]A. Sawada, Y. Takagi, and Y. Ishibashi, "The origin of the ferroelectric phase transition in ammonium sulfate", Journal of the Physical Society of Japan **34**, 748–754 (1973).

[158]P Lloveras, E. Stern-Taulats, M Barrio, J.-L. Tamarit, S. Crossley, W. Li, V. Pomjakushin, A Planes, L. Mañosa, N. Mathur, et al., "Giant barocaloric effects at low pressure in ferrielectric ammonium sulphate", Nature communications **6**, 1–6 (2015).

[159]A. Smith, C. R. Bahl, R. Bjørk, K. Engelbrecht, K. K. Nielsen, and N. Pryds, "Materials challenges for high performance magnetocaloric refrigeration devices", Advanced Energy Materials **2**, 1288–1318 (2012).

[160]X Moya, S. Kar-Narayan, and N. D. Mathur, "Caloric materials near ferroic phase transitions", Nature materials **13**, 439–450 (2014).

[161]S Crossley, W Li, X Moya, and N. Mathur, "Large electrocaloric effects in single-crystal ammonium sulfate", Philosophical Transactions of the Royal Society A: Mathematical, Physical and Engineering Sciences **374**, 20150313 (2016).

[162]J. Scott, "Electrocaloric materials", Annual Review of Materials Research **41**, 229–240 (2011).

[163]K. Hasebe, "Studies of the crystal structure of ammonium sulfate in connection with its ferroelectric phase transition", Journal of the Physical Society of Japan **50**, 1266–1274 (1981).

[164]E. O. Schlemper and W. C. Hamilton, "Neutron-diffraction study of the structures of ferroelectric and paraelectric ammonium sulfate", The Journal of Chemical Physics **44**, 4498–4509 (1966).

[165]L. M. Malec, M. Gryl, and K. M. Stadnicka, "Unmasking the mechanism of structural para- to ferroelectric phase transition in $(NH_4)_2SO_4$", Inorganic Chemistry **57**, PMID: 29616803, 4340–4351 (2018).

[166]B. Andriyevsky, K. Doll, and M. Jansen, "First principles study of structural stability, electronic and related properties of $(NH_4)_2SO_4$", J. Phys. Chem. Solids **71**, 357–363 (2010).

[167]K. Hasebe and S. Tanisaki, "X-ray diffuse scattering of paraelectric ammonium sulfate", Journal of the Physical Society of Japan **42**, 568–573 (1977).

[168]Y. Jain, P. Bajpai, R Bhattacharjee, and D Chowdhury, "Phase transition and temperature dependence of the molecular distortion of ions in ammonium sulphate", Journal of Physics C: Solid State Physics **19**, 3789 (1986).

[169]Y. Jain, H. Bist, and G. Upreti, "The ferroelectric phase transition in ammonium sulphate", Chemical Physics Letters **22**, 572–575 (1973).

[170]B. Torrie, C. Lin, O. Binbrek, and A Anderson, "Raman and infrared studies of the ferroelectric transition in ammonium sulphate", Journal of Physics and Chemistry of Solids **33**, 697–709 (1972).

[171]D. D. S. Meneses, G Hauret, P Simon, F Brehat, and B Wyncke, "Phase-transition mechanism in $(NH_4)_2SO_4$", Physical Review B **51**, 2669 (1995).

[172]S Hoshino, K Vedam, Y Okaya, and R Pepinsky, "Dielectric and thermal study of $(NH_4)_2SO_4$ and $(NH_4)_2BeF_4$ transitions", Physical Review **112**, 405 (1958).

[173]O. Arnold, J.-C. Bilheux, J. Borreguero, A. Buts, S. I. Campbell, L Chapon, M. Doucet, N Draper, R. F. Leal, M. Gigg, et al., "Mantid—data analysis and visualization package for neutron scattering and $\mu$ sr experiments", Nuclear Instruments and Methods in Physics Research Section A: Accelerators, Spectrometers, Detectors and Associated Equipment **764**, 156–166 (2014).

[174]H. D. Duncan, M. T. Dove, D. A. Keen, and A. E. Phillips, "Local structure of the metal–organic perovskite dimethylammonium manganese (ii) formate", Dalton Transactions **45**, 4380–4391 (2016).